Statistical mechanics of fluctuating polymer rings

Karen Winkler

München 2006

Statistical mechanics of fluctuating polymer rings

Karen Winkler

Diplomarbeit
an der Fakultät für Physik
der Ludwig–Maximilians–Universität
München

vorgelegt von
Karen Winkler
aus Hannover

München, den 26. Mai 2006

Erstgutachter: Prof. E. Frey
Zweitgutachter: Prof. H. Gaub

Zusammenfassung

Diese Arbeit untersucht die statistische Mechanik von Polymerringen und Bündeln von Polymerringen im Gleichgewicht. Die Konformationen der Ringe werden bestimmt durch das Zusammenspiel von thermischen Stößen einerseits und der inneren elastischen Spannung der Polymere andererseits. Da Polymerbündel einen asymmetrischen Querschnitt aufweisen, werden sie als Band modelliert. Neben Steifigkeit gegenüber Verdrillung besitzen Bänder gegenüber Deformierungen entlang der beiden Hauptachsen des Querschnittes unterschiedliche Biegesteifigkeiten.
Für die theoretische Beschreibung fluktuierender Ringe wird zunächst ein analytisches Modell entwickelt, welches anschließend mittels Metropolis-Monte-Carlo-Simulationen überprüft und erweitert wird.

Das in dieser Arbeit vorgestellte analytische Modell für schwach fluktuierende Ringe berücksichtigt im Gegensatz zu früheren Arbeiten einen asymmetrischen Querschnitt und nimmt als Grundzustand des freien Polymer den gestreckten Stab an, wie es für die Filamente des Zytoskeletts zutrifft. In dem Modell wird die Trajektorie des Bandes mit Eulerwinkeln beschrieben. Basierend auf der Annahme, dass nur kleine Abweichungen vom Grundzustand eines starren Ringes möglich sind, wird die elastische freie Energie der Ringe um die Konformation des Grundzustandsringes entwickelt. Dieser ist so gewählt, dass er die elastische freie Energie minimiert.
Um die allgemeinen Eigenschaften von Polymerringen zu beschreiben, wird der mittlere quadratische Durchmesser als der charakteristische Parameter eingeführt. Dieser wird in Abhängigkeit von den Biegesteifigkeiten und der Verdrillungssteifigkeit detailliert analysiert.

Die Metropolis-Monte-Carlo-Simulationen werden eingesetzt, um Polymerringe, die nur aus einem einzelnen halbsteifen Filament bestehen, zu charakterisieren. Diese haben einen kreisförmigen Querschnitt und keine Verdrillungssteifigkeit, sind aber als Grenzfall in dem allgemeinen Modell enthalten. Der Vergleich der Simulationsdaten mit den analytischen Vorhersagen für den mittleren quadratischen Durchmesser ergibt eine hervorragende Übereinstimmung bis zu hohen Flexibilitäten hin. Daher wird der mittlere quadratische Durchmesser als neue Messgröße zur Bestimmung der Steifigkeit von halbsteifen Polymerringen vorgeschlagen.
Desweiteren wurden die Monte-Carlo-Simulationen dazu genutzt, den Übergang zwischen halbsteifen und flexiblen Polymerringen zu untersuchen. Bei der Betrachtung der Verteilung der Radii zeigt sich, dass der Übergang von einem *finite-size-Effekt* dominiert ist, der aus einer oberen Schranke für den Radius resultiert.
Schließlich wird die Gestalt der Polymerringe untersucht. Frühere Untersuchungen erstreckten sich auf die Gestalt flexibler Polymere mit und ohne Selbstvermeidung. Diese Arbeit bietet jedoch eine Analyse der Form von Polymerringen über die gesamte Flexibilitätsspanne. Im Grenzfall schwacher Fluktuationen erklärt ein Skalenargument die Änderung der Gestalt.

Dieses beruht auf der Annahme, dass die mittlere Konfiguration eines steifen Polymerringes elliptisch ist. Für flexiblere Ringe mit größeren Fluktuationen wird ein Potenzgesetz gefunden.

Contents

1 Introduction

Polymers are very long molecules consisting of many similar repeating units that are covalently bond to each other. Their designation is derived from the Greek words *polys* (many) and *meros* (parts). *Biopolymers* are composed of organic molecule subunits and synthesized by living organisms. Famous examples are DNA and RNA, which encode our genetic information, and the filaments and tubules of the cytoskeleton. As the human body volume is filled by $\sim$11% of bony skeleton, similarly the cell volume consists of $\sim$11% of cytoskeleton [17]. The cytoskeleton facilitates establishing and maintaining the shape of cells, takes an active part in cell motion and plays an important role in intra-cellular transport and cell-division.

To understand the elastic properties of the cell's cytoskeleton, it is important to study its structural components, which are relatively stiff polymers on the one hand, and proteins that interconnect the polymers to form bundles and networks on the other hand. The polymers participating can be distinguished into three classes according to their diameter and the proteins they consist of: actin filaments, intermediate filaments and microtubules, see Fig. 1.1. Actin filaments, around 7nm in diameter, consist of two intertwined chains of actin proteins, Fig. 1.2(a). Intermediate filaments have diameters of 8 to 11nm, lying between the other two basic structures and are composed of a variety of proteins that are expressed in different types of cells, see Fig. 1.2(b). Microtubules are hollow cylinders, about 25nm in diameter, that are assembled by typically thirteen parallel protofilaments, which are polymers of tubulin proteins, as depicted in Fig. 1.2(c). Inherent to all cytoskeletal filaments is an almost *inextensible* backbone and a high bending stiffness, characteristics of *semiflexible* polymers.

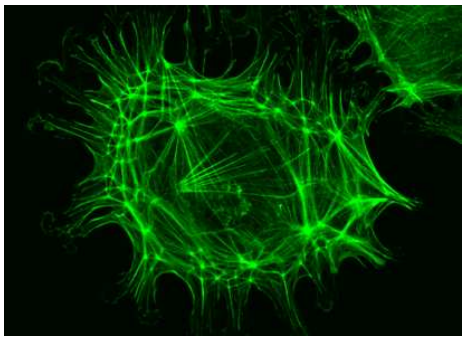

Figure 1.1: F-actin cytoskeleton in a 2D cultured bovine articular chondrocyte stained green for fluorescence microscopy. Courtesy of M. Kerrigan, A. Hall and L. Sharp.

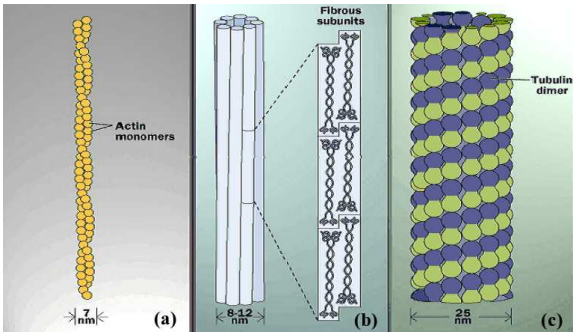

Figure 1.2: Schematic drawing of (a) an actin filament consisting of two intertwined polymer chains of actin proteins, (b) an intermediate filament and (c) a microtubulus constructed of thirteen tubulin polymers [11].

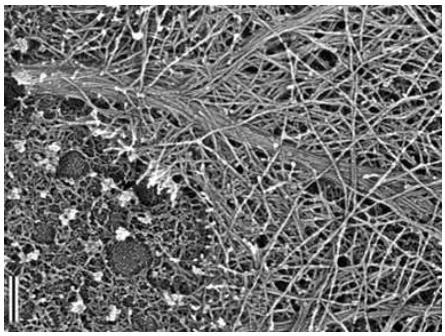

Figure 1.3: Electron microscopy picture of a tight bundle of actin filaments forming a filopodium, a slender projection of the cytoskeleton extending at the leading front of migrating cells. As reference to the dimensions, the bar has a size of 0.2μm. Courtesy of T. M. Svitkina.

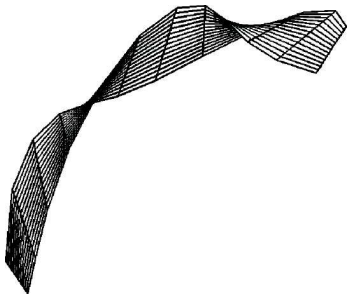

Figure 1.4: Schematic drawing of a ribbon [42]. The cross-sectional plane is noncircular, which leads to two different bending stiffnesses for deformations about the two principal axes of the cross section, respectively. In addition, a ribbon has twist stiffness due to its cross-sectional extend.

Pursuing a comprehension of the elastic properties of cytoskeletal filaments, the polymers are described neglecting their microstructure, architecture and chemical composition. On the mesoscopic length scale of hundreds of nanometers they can then be illustrated as a continuous space curve. Hence, the filaments are only distinguished by their elastic properties, i.e. their bending stiffness. The latter is characterized by the length along the backbone over which orientational correlations decay, denoted by *persistence length* l_p. This quantity is infinite for a rigid rod, while vanishing for a flexible polymer, whose bending does not require any energy. The persistence length of semiflexible polymers lies in between those two extrema. For the cytoskeletal filaments, the persistence length is larger than any microscopic length scale, l_p =17μm [20, 22], l_p =2μm [6] and l_p =6mm [39, 41] for actin filaments, intermediate filaments and microtubules, respectively. Hence, semiflexible polymers can be defined by

$$d \ll l_p, L \quad \text{for semiflexible polymers,} \tag{1.1}$$

where d denotes a microscopic length scale of the filament, for example its diameter, and L indicates the total length of the polymer. DNA, which has a diameter of 2.2nm and a persistence length of l_p =50nm, is also a semiflexible polymer according to the definition above.

Proteins interconnect cytoskeletal filaments to form bundles as parallel arrays of closely packed filaments or tubules. Actin bundles, for example, are the building blocks for villi in the intestinal tract, filopodia of migrating cells and cilia in the ear, see Fig. 1.3. With a growing number of polymers in a bundle, the cross-section of the latter increases, such that the mesoscopic picture of a continuous space curve with a symmetric bending stiffness has to be refined. Bundles may be better described as a ribbon, which is asymmetric in the cross-sectional plane. Then, two persistence lengths corresponding to bending stiffness about the two principal directions of the cross-section are required. The ribbon model is completed by introducing a twist stiffness, see Fig. 1.4.

Previously, ribbon models have been used to give a more detailed picture of the DNA, which consists of two hydrogen-bond-connected complementary strands [3]. The DNA helix is then

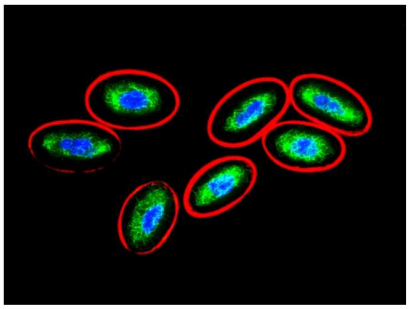

Figure 1.5: Postnatal chicken erythrocytes with the circular microtubules bundle stained in red. Vimentin intermediate filaments are marked green and the DNA is labelled blue. Courtesy of P. Dráber.

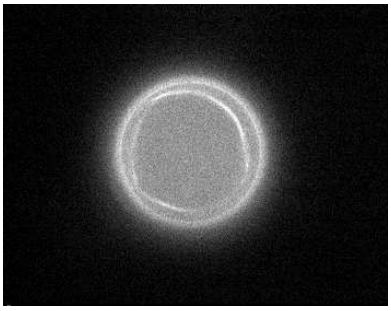

Figure 1.6: Actin bundle ring within a giant vesicle. The bundle is not attached to the membrane and may therefore fluctuate freely. Courtesy of M. Claessens [9].

understood as an intrinsically twisted band, whose bending stiffness is different about an axis parallel to the hydrogen bonds compared to a perpendicular axis [42]. Special interest has been drawn to circular DNA and to its effect of supercoiling. The key role in supercoiling is played by nicked DNA rings, where the two ends of the intrinsically twisted DNA ribbon are connected in a link such that the planes of the hydrogen bonds enclose a non-zero angle. Now the geometric constraint of the ring induces an interplay between the magnitude of the angle enclosed by the two ends of the ring with the total twist, which leads to the effect of supercoiling [3]. Hence, the geometry of a ring induces interesting effects to semiflexible polymers.

This thesis is motivated by the ubiquitous presence of *polymer rings* in both cellular and biomimetic systems. The first biopolymer that was discovered to be circular is the DNA. Closed loops of double-stranded DNA are found in viruses and certain prokaryotes. However, cytoskeletal filaments have only recently been perceived to occur in circular structures. A prominent in vivo example for loops of cytoskeletal polymers is the formation of a microtubules bundle ring in the red blood cells, the erythrocytes, of birds and reptiles [15, 55, 34]. During the maturation of the erythrocytes, microtubules assemble to form a bundle. With increasing length and thickness the bundle becomes stiffer; trying to minimize its bending energy, it aligns circularly to the "equatorial" of the erythrocyte, forming the so-called marginal band. In Fig. 1.5 the microtubules bundle of adult chicken erythrocytes is pictured under microscope. In vitro closed actin and actin bundle rings are generated by letting actin filaments assemble in a giant vesicle [33, 9]. The actin filaments aggregate to form a ring due to the confinement but do not interact with the vesicle membrane otherwise, see Fig. 1.6. Hence, the statistical mechanics of actin and actin bundle rings can be studied in this setup. Furthermore, actin ring formation can be induced in unconstraining geometries by counter-ions [51].

Modelling the statistical mechanics of polymer rings is the topic of this thesis. To take the twist stiffness and anisotropic bending stiffness of bundles into account, the polymer bundles are described as ribbons, see Fig. 1.4. The case of a single semiflexible polymer whose ends are interconnected to form a ring is also comprised in the ribbonlike ring model as a limiting case. To model the behavior of cytoskeletal filaments and filament bundles, the ground state configuration of the polymers is taken to be a straight line in contrast to previous work on

DNA rings, where a helix with intrinsic twist is considered as the ground state.
Investigating the fascinating geometric constraint of a ring, a new analytic model for tight ribbonlike rings is introduced. The model is based on a parameterization of the trajectories of ribbons in terms of Euler angles. To obtain an analytically tractable model for stiff rings the free energy of a ribbonlike ring is approximated harmonically about the ground state ring conformation, which minimizes the elastic free energy.
In the course of the analysis of the model, the mean square diameter is identified as the best characterization of the average state of a fluctuating ring, depending on the three stiffness parameters, one for twist and two for bending. The mean square diameter and its dependence on the respective stiffnesses are discussed in detail.
To assess the quality of the approximations and to investigate a broader range of flexibility, Monte Carlo simulations are employed, which have unveiled impressive features of semiflexible polymer rings; the limiting case where no twist stiffness is imposed and the bending stiffness is isotropic. For the latter the mean square diameter is found to obey the analytic predictions excellently even up to a tremendous degree of flexibility.
For the mean radius of the ring, a linear decay with the ratio of perimeter to persistence length is discovered, again over a wide range of parameters. Thus, the mean square diameter and the mean radius provide a good measurement to access the persistence length of semiflexible rings in the experimental analysis of fluctuating rings.
Finally, the striking change of shape of a semiflexible ring is examined. By investigating the shape, its dominating modes can be defined depending on its flexibility. The shape of tight rings is proven to be governed by an elliptical mode applying a scaling argument. Furthermore, the onset of higher modes and the overall change of shape is investigated.

The outline of this thesis is as follows.

- In chapter 2 a short review on polymer models is provided, followed by an introduction to the formalism of describing ribbons. In addition, a scaling argument for the mean radius of the ring are presented.
- Having established the setting, analytic calculations of the statistical mechanics of stiff ribbonlike rings are presented in chapter 3. The main focus is set on an analysis of the modes of the fluctuating ring and its average square diameter. The latter also provides a tool to explore the different limiting cases of twist and bending stiffnesses.
- Chapter 4 introduces the simulation technique, namely Metropolis Monte Carlo, used to approach a broader range of parameters than feasible with analytic calculations. The procedure to simulate a semiflexible ring is demonstrated in detail.
- Results of the simulations of a semiflexible ring are presented in chapter 5. The mean square diameter is found to obey the analytic predictions up to a high degree of flexibility. Furthermore, analyzing the radius distribution yields an interesting cross-over from semiflexible to flexible behavior, also observed in the mean shape of the configurations.
- Finally, a summary and an outlook are given in chapter 6.

2 From polymers to ribbonlike rings

Modelling polymers commenced with the study of flexible chains. To account for rigidity when deforming a polymer, models were developed including bending stiffness [29], yielding up to now good predictions for semiflexible polymers. With the discovery of circular DNA, polymer rings with intrinsic twist and twist stiffness were investigated [3], to study the implications of the helical structure of the DNA. Only recently, statistical mechanics of polymers have been studied more detailed by modelling the polymer as a ribbon taking two bending degrees of freedom together with a twist degree of freedom into account [42, 43].
The first part of this chapter gives an overview about the "classical" polymer models while the second part introduces the description of a polymer as a ribbon and illustrates the fluctuations of a ring.

2.1 Polymer models

To model polymers one has to find the appropriate level of abstraction. The elastic properties of a polymer are best described above their microstructure, architecture and chemical composition. For this purpose a polymer is represented as a chain of segments of equal length, where the model is further idealized by assuming that the polymer segments do not interact with themselves or the solvent around them.
The models differ in how adjacent segments are correlated. In the freely jointed chain model all correlations are ignored, therefore, the model serves to describe flexible polymers. On the other hand, in the freely rotating chain model the segments are restricted to have a fixed angle between successive bonds. In the wormlike chain model the stiffness is induced by assigning large energies to highly bend configurations. The results are analogous to the continuous description of the freely rotating chain model, yielding an exponential decay of the tangent-tangent correlation.

2.1.1 Freely jointed chain model

The freely jointed chain model is the most basic description of flexible polymers. The polymer is represented as a sequence of N stiff segments $\mathbf{t}_i$ of equal length b connected by free hinges such that the direction of each segment is independent of all other segments, as depicted in Fig. 2.1.

The total length of the polymer is $L = Nb$, but in equilibrium the chain is coiled only due to entropy. All configurations have the same energy, i.e. zero, and there is only one conformation where the polymer resembles a straight line but an exponentially with the

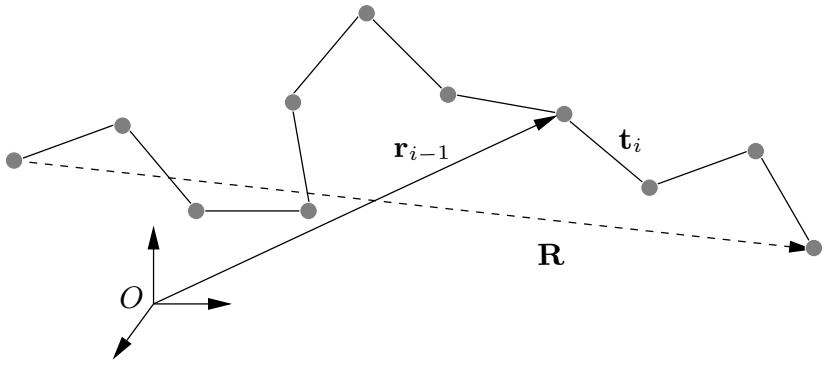

Figure 2.1: The freely jointed chain model as the simplest model for a flexible polymer. The bond vectors are denoted $\mathbf{t}_i$, while $\mathbf{r}_i$ indicate the position of the bond vectors. $\mathbf{R}$ is the end-to-end distance.

number of segments growing amount of configurations where it is coiled up. The size of the polymer is characterized by the end-to-end vector $\mathbf{R}$:

$$\mathbf{R} = \sum_{i=1}^{N} \mathbf{t}_i \,. \tag{2.1}$$

Clearly, the ensemble average $\langle \mathbf{R} \rangle$ of $\mathbf{R}$ is zero due to the spatial isotropy. It is therefore instructive to calculate the average of the squared end-to-end distance $\langle \mathbf{R}^2 \rangle$:

$$\langle \mathbf{R} \rangle = 0 \,, \tag{2.2}$$

$$\langle \mathbf{R}^2 \rangle = \sum_{i=1}^{N} \sum_{j=1}^{N} \langle \mathbf{t}_i \mathbf{t}_j \rangle = \sum_{i=1}^{N} \langle \mathbf{t}_i^2 \rangle = Nb^2. \tag{2.3}$$

Hence, the size R_0 of the polymer grows with the square root of the total number of segments

$$R_0 = b\sqrt{N}. \tag{2.4}$$

This characteristic applies to all ideal polymers with correlations decaying exponentially on large scales and N large [14]. The microscopic differences of the polymers are contained in the prefactor b, denoted Kuhn length. This is a consequence of the central limit theorem, as long as $\mathbf{R}$ can be represented as the sum of independent variables the radius distribution will be Gaussian with mean zero and variance $\langle R^2 \rangle = b^2 N$:

$$P(\mathbf{R}, N) = \left(\frac{3}{2\pi N b^2} \right)^{3N/2} \exp\left(-\frac{3\mathbf{R}^2}{2Nb^2} \right). \tag{2.5}$$

Result (2.3) is well known from the theory of random walks, since the conformation of a freely jointed chain polymer is precisely the trajectory of a random walk.
Another parameter to characterize polymers is the radius of gyration R_g. It is defined as the average distance between the segments and the center of mass and derives its importance from the fact that the radius of gyration is directly measurable in experiments and is also defined for branched polymers. Defining the center of mass as the sum over all position vectors $\{\mathbf{r}_i\}$ divided by N,

$$\mathbf{r}_{com} = \frac{1}{N} \sum_{i=1}^{N} \mathbf{r}_i \,, \tag{2.6}$$

the squared radius of gyration in the freely jointed chain model yields:

$$R_g^2 = \frac{1}{N}\sum_{i=1}^{N}\langle(\mathbf{r}_i - \mathbf{r}_{com})^2\rangle = \frac{1}{6}Nb^2. \tag{2.7}$$

The mean radius of gyration R_g vanishes because of the spatial isotropy.

For polymer models with no long-range interactions the statistical properties do not depend on the details of the model as long as the number of segments N is large. Based on this universal behavior of ideal polymers, the Gaussian chain model is introduced. The idea is to divide a chain consisting of a large number of segments into n groups which serve as the new segments. The length of the new segments $|\mathbf{t}|$ then follows a Gaussian distribution.

$$p(\mathbf{t}) = \left(\frac{3}{2\pi b^2}\right)^{3/2} \exp\left(-\frac{3\mathbf{t}^2}{2b^2}\right). \tag{2.8}$$

Writing each bond vector in terms of the position vectors of the adjacent bonds $\mathbf{t}_i = \mathbf{r}_i - \mathbf{r}_{i-1}$, the probability distribution of the set of position vectors is

$$P(\{\mathbf{r}_i\}) = \left(\frac{3}{2\pi b^2}\right)^{3n/2} \exp\left(-\frac{3}{2b^2}\sum_{i=1}^{n}(\mathbf{r}_i - \mathbf{r}_{i-1})^2\right). \tag{2.9}$$

Hence, the Gaussian chain can be interpreted as a sequence of segments consisting of harmonic springs, where the "energy" of the system is given by

$$E = \frac{k}{2}\sum_{i=1}^{n}(\mathbf{r}_i - \mathbf{r}_{i-1})^2. \tag{2.10}$$

Here $k = 3k_BT/b^2$ denotes the "entropic" spring constant. The "energy" has a purely entropic origin, stretched conformations are suppressed due to their small number, compared to coiled ones, and not due to energetic reasons.

2.1.2 Freely rotating chain model

To account for stiffness along the polymer chain correlations between bonds are induced. In the freely rotating chain model, introduced by Kratky and Porod [29], the correlations are produced by a geometric hindrance, the angle between every two segments is constrained to a fixed angle θ, see Fig. 2.2. No restrictions apply for the rotation about single bonds. If the angle θ is chosen very small this model accounts well for stiff polymers.

The model is characterized by the correlation of two bond vectors. If two bond vectors are separated by n segments, the correlations decay with the cosine of the fixed angle θ to the power of n. The freely rotating chain model becomes of special interest when performing the continuum limit and setting $\theta \ll 1$. For this purpose, the bond length $b \to 0$ is send to zero, while the total number of bonds $N \to \infty$ goes to infinity, keeping $Nb = L$ fixed. This limit yields an exponential decay of the correlations such as found in the wormlike chain model.

$$\langle \mathbf{t}_i \mathbf{t}_{i+n}\rangle = (-\cos\theta)^n \overset{b\to 0, N\to\infty}{\longrightarrow} \exp(-nb/l_p)\,. \tag{2.11}$$

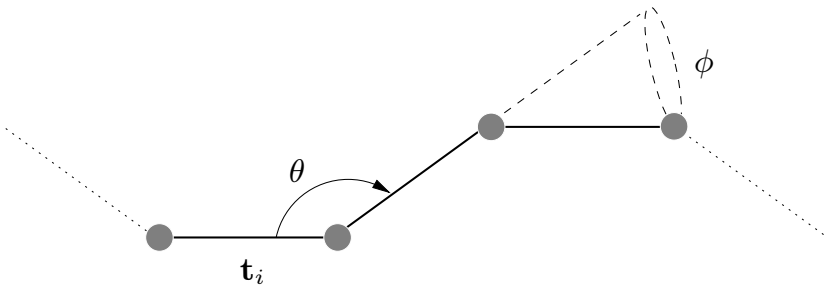

Figure 2.2: In the freely rotating chain model the angle between adjacent bonds is restricted to a fixed angle θ, while rotations about single bonds by an angle ϕ are free.

If the characteristic length scale over which correlations decay, the persistence length l_p, is smaller than the total length $L \gg l_p$, the correlation are zero as in the case of the freely jointed chain model. In the opposite limit $L \ll l_p$ the correlations become infinite recovering the behavior of a stiff rod.
In the continuum limit the freely rotating chain model yields identical results to the wormlike chain model, whose properties will be explained in detail in the next section.

2.1.3 Wormlike chain model

The wormlike chain model introduces stiffness along the polymer through an interaction energy ϵ between adjacent bonds:

$$H = -\epsilon \sum_{i=1}^{N-1} \mathbf{t}_i \mathbf{t}_{i+1} \,, \tag{2.12}$$

where the bond vectors are now normalized $|\mathbf{t}_i| = 1$. The energy is minimized for parallel bond vectors and maximized for perpendicular ones. Hence, for very large interaction energy ϵ the bond vectors will align to form a rod.
The wormlike chain elastic free energy "Hamiltonian" is identical to the classical one-dimensional Heisenberg spin model on identifying the bond vectors with spins and the interaction energy ϵ with the nearest neighbor exchange energy J [16]. Hence, some results may be inferred from the Heisenberg spin model, such as the correlation of spins, which corresponds to the correlation of bond vectors in the wormlike chain model.
The correlation of two bond vectors separated by n segments can be calculated from the partition sum, yielding:

$$\langle \mathbf{t}_i \mathbf{t}_{i+n} \rangle = \exp\left(-\frac{nb}{l_p}\right), \tag{2.13}$$

where the characteristic length over which the correlations decay, the persistence length l_p, is defined by the interaction energy ϵ and the thermal energy $\beta = 1/k_B T$ as

$$l_p \equiv -\frac{b}{\ln(\coth(\beta\epsilon) - 1/\beta\epsilon)} \,. \tag{2.14}$$

This discretized representation of the wormlike chain model is very useful for the implementation in simulations, for analytical calculations the continuous version has proven to be more efficient.

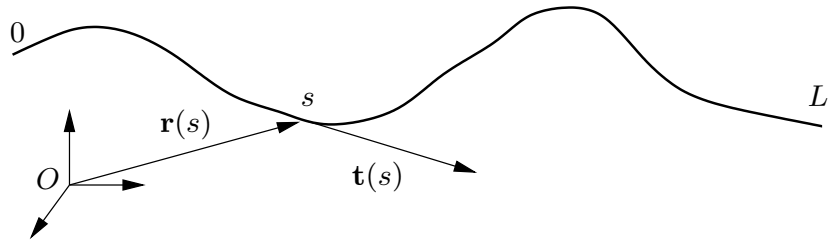

Figure 2.3: The wormlike chain is a space curve parameterized by $s \in [0, L]$ whose bending requires energy.

Performing the continuum limit we set $b \to 0$, $N \to \infty$ keeping $L = Nb$ and $\tilde{\epsilon} = \epsilon/N$ fixed. Since the bond length shrinks to zero the former bond vectors become tangent vectors of a continuous curve parameterized by the arc length s. In the continuum limit the persistence length becomes directly related to the overall length of the polymer and the interaction energy, while the sum over all bond vectors in the elastic free energy is replaced by an integral. The product of adjacent bond vectors is substituted by the squared derivative of the tangent vector:

$$\begin{aligned} l_p &\to b\beta\epsilon = \frac{L\tilde{\epsilon}}{k_B T} , \\ b\sum_{i=1}^{N-1} &\to \int_0^L ds , \\ \mathbf{t}_i\mathbf{t}_{i+1} = \frac{1}{2}\left[(\mathbf{t}_{i+1} - \mathbf{t}_i)^2 - 2\right] &\to \frac{b^2}{2}\left(\frac{\partial \mathbf{t}(s)}{\partial s}\right)^2 - 1 . \end{aligned} \tag{2.15}$$

Neglecting irrelevant constants and substituting $\epsilon b = \tilde{\epsilon} L = l_p k_B T$ the elastic free energy yields,

$$H = k_B T \frac{l_p}{2}\int_0^L \left(\frac{\partial \mathbf{t}(s)}{\partial s}\right)^2 = \frac{\kappa}{2}\int_0^L \left(\frac{\partial \mathbf{t}(s)}{\partial s}\right)^2 , \tag{2.16}$$

where the bending modulus κ is defined as $\kappa \equiv l_p k_B T$ [47].

The continuous version of the elastic free energy can easily be motivated from the viewpoint of differential geometry. Consider a space curve $\mathbf{r}(s)$ of total length L parameterized by its arc length s, the curvature at each point along the curve is given by the derivative of the tangent, $\partial \mathbf{t}(s)/\partial s$. To represent a semiflexible polymer one requires bending to be energeticly costly, hence, the "Hamiltonian" should be proportional to the overall curvature. Since the energy should penalize positive and negative curvature in the same way, the square of the curvature enters in the free elastic energy. From the theory of elasticity the weight of the curvature is given by the bending modulus κ [31]. Hence, the "Hamiltonian" has the form of Eq. (2.16). The description of the wormlike chain in terms of differential geometry already incorporates the local inextensibility of the space curve, which is imposed by setting the magnitude of the tangent equal one.

$$|\mathbf{t}(s)| = 1 . \tag{2.17}$$

This inextensibility constraint is essential for the description of semiflexible polymer, but also induces most of the mathematical difficulties in the calculation of its statistical properties. Some of the few results to be obtained analytically are the mean squareend-to-end distance

$\langle R^2 \rangle$ and the mean square radius of gyration $\langle R_g^2 \rangle$. In the continuous description the tangent-tangent correlation becomes:

$$\langle \mathbf{t}(s)\mathbf{t}(s') \rangle = \exp\left(-\frac{|s-s'|}{l_p} \right). \tag{2.18}$$

Using this expression the mean square end-to-end distance yields [32]:

$$\begin{aligned} \langle R^2 \rangle &= \langle (\mathbf{r}(L) - \mathbf{r}(0))^2 \rangle \\ &= \left\langle \left(\int_0^L ds\, \mathbf{t}(s) \right)^2 \right\rangle \\ &= \int_0^L ds \int_0^L ds'\, \langle \mathbf{t}(s)\mathbf{t}(s') \rangle \\ &= L^2 f_D(L/l_p)\,, \end{aligned} \tag{2.19}$$

where the Debye function f_D is defined as, $f_D(x) \equiv \frac{2}{x^2}\left(e^{-x} - 1 + x\right)$. It is interesting to investigate the limits of $\langle R^2 \rangle$:

$$\langle R^2 \rangle = \begin{cases} 2Ll_p & \text{for } L \gg l_p \\ L^2 & \text{for } L \ll l_p \end{cases}. \tag{2.20}$$

Hence, in the flexible limit where $L \gg l_p$ the mean square end-to-end distance yields just the result of the freely jointed chain where the Kuhn length is identified as $b = 2l_p$, in the stiff limit $L \ll l_p$ the stiff rod with the end-to-end distance equal to the total length L is recovered.
For reasons of completeness, the radius of gyration as a measure for the spatial extend is presented, again yielding the expected limits:

$$\begin{aligned} \langle R_g^2 \rangle &= \frac{1}{L} \int_0^L ds\, \langle (\mathbf{r}(s) - \mathbf{r}_{com})^2 \rangle \\ &= \frac{1}{2L^2} \int_0^L ds \int_0^L ds'\, \langle \big(\mathbf{t}(s)\mathbf{t}(s')\big)^2 \rangle \\ &= L^2 \left(f_D(L/l_p) - 1 + \frac{L}{3l_p} \right) \\ &= \begin{cases} \frac{2l_pL}{6} & \text{for } L \gg l_p \\ \frac{L^2}{12} & \text{for } L \ll l_p \end{cases}. \end{aligned} \tag{2.21}$$

Further analytic results were derived, such as the orientational probability distribution of a semiflexible polymer yielding the calculation of even higher moments of the end-to-end distance, i.e. $\langle R^4 \rangle$ [47], the pair correlation function $\langle \mathbf{r}(s)\mathbf{r}(s') \rangle$ [1] and the radial distribution function [12, 54].

Weakly bending rod approximation

To analyze a stiff polymer it is convenient to work in the so-called weakly bending rod approximation also known as Monge representation. If the polymer is almost completely stretched

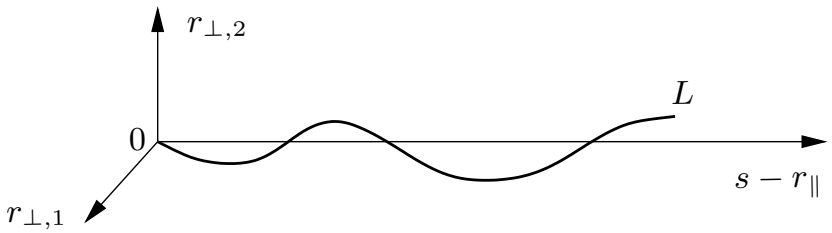

Figure 2.4: In the weakly bending rod approximation the position of the space curve is characterized by the transverse undulations $r_{\perp,i}$, $i = 1, 2$, and the stored length $s - r_{\parallel}$.

exhibiting no overhangs the position vector $\mathbf{r}(s)$ can be divided into the projection along the average axis of the contour $s - r_{\parallel}(s)$ and the undulations perpendicular to it $\mathbf{r}_{\perp}(s)$,

$$\mathbf{r}(s) = (\mathbf{r}_{\perp}(s), s - r_{\parallel}(s)) \,, \tag{2.22}$$

where $r_{\parallel}(s)$ denotes the stored length, as illustrated in Fig. 2.4. Due to the inextensibility constraint in Eq. (2.17) the undulations and the stored length are related by:

$$(\dot{\mathbf{r}}_{\perp}(s))^2 = 2\dot{r}_{\parallel}(s) - \left(\dot{r}_{\parallel}(s)\right)^2 , \tag{2.23}$$

where dots indicate derivatives with respect to s. Thus, the fluctuations parallel to the average axis of the contour are only second order in the amplitudes of the transverse fluctuations and can therefore be neglected. Hence, the Hamiltonian in the weakly bending rod approximation results in:

$$H_{wb} = \frac{\kappa}{2} \int_0^L ds\, \ddot{\mathbf{r}}_{\perp}(s)^2. \tag{2.24}$$

This free energy approximation is used in the following section to derive a scaling relation for the fluctuations of a tight wormlike ring.

2.2 Ribbonlike rings

To capture the fluctuations of polymers and polymer bundles more detailed the polymers are modelled as ribbons. In contrast to the wormlike chain model which exhibits one bending modulus, a ribbon accounts for two bending moduli, one about each of the two mutually orthogonal axes in the cross section of the ribbon [31]. Furthermore, a twist modulus is incorporated as stiffness against torsion and twist.
The interplay of all three moduli becomes intriguing when the ribbon is constrained to form a ring. The ring induces an additional stiffness to the ribbon and also serves to couple the bending and twisting modes.
A scaling argument for the fluctuations of a ring is derived based on the wormlike chain model as presented in the former section. Afterwards, the mathematical description of an elastic rod is introduced, which is employed to calculate the statistical mechanics of a ribbon in the following chapter. In the last part the elastic free energy of a ribbon is explained.

2.2.1 The fuzzy diameter

Consider a tight wormlike ring of contour radius R_c to be undulating due to thermal fluctuations. The area enclosed by the ring is smaller than the area of a rigid ring, where the radius at every position along the ring is varying by an amount $\tilde{D}$, denoted by the fuzzy diameter, see Fig. 2.5. A simple scaling argument for this fuzzy diameter can be given by employing the weakly bending rod approximation [7], introduced in 2.1.3.

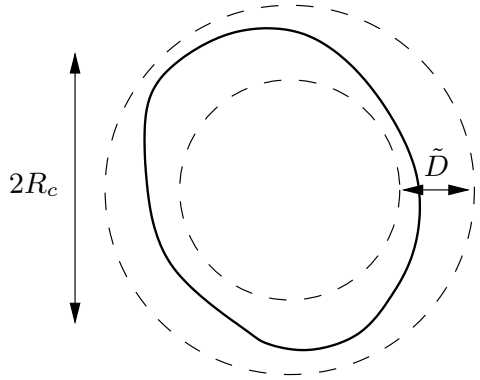

Figure 2.5: An undulated wormlike ring with contour radius R_c. The radius differs between its minimal value and its maximal value by an amount denoted by the fuzzy diameter $\tilde{D}$.

As a simple model for a fluctuating ring a stretched out polymer with periodic boundary conditions is considered. This approach only mimics a ring since the overall imposed curvature of a ring is neglected. Assuming the polymer to be stiff enough that no overhangs occur with respect to the trajectory of a rigid rod, the transverse undulations $\mathbf{r}_\perp$ can be described with the Hamiltonian of the weakly bending rod approximation, as in Eq. (2.24). Assuming periodic boundary conditions, i.e. $\mathbf{r}_\perp(s+L) = \mathbf{r}_\perp(s)$, the undulations are expanded in Fourier modes with $n \in N$,

$$r_{\perp,i}(s) = \sum_n a_{n,i} \exp\left(\mathrm{i}\frac{n2\pi s}{L}\right), \tag{2.25}$$

where $i = 1, 2$ denotes the two independent transverse modes. Using the definition of the delta functional, $\int_0^L \exp(\mathrm{i}\,2(n-m)\pi/L) = L\delta_{n,m}$, the elastic free energy results in

$$H = \frac{8\kappa\pi^4}{L^3} \sum_{n,i} n^4 a_{n,i}^2 \,. \tag{2.26}$$

The equipartition theorem states that every transverse mode has an energy of $k_B T$. Hence, the transverse modes are given by

$$\langle a_{n,i}^2 \rangle = \frac{L^2}{8n^4\pi^4} \frac{L}{l_p} \,, \tag{2.27}$$

yielding amplitudes in real space of

$$\langle r_{\perp,i}^2 \rangle = \frac{L^2}{8\pi^4} \frac{L}{l_p} \sum_n \frac{1}{n^4} = \frac{1}{720} L^2 \frac{L}{l_p} \,. \tag{2.28}$$

Given the squared undulation, the fuzzy diameter is just twice the square root of the transverse fluctuations, yielding:

$$\tilde{D} \propto 2\sqrt{\langle r_{\perp,1}^2 \rangle} \approx 1.17 \frac{R_c^{3/2}}{l_p^{1/2}} \,. \tag{2.29}$$

This scaling relation has been derived in various ways [7, 40, 48] and has also been confirmed in simulations [10, 9], where the prefactor was discovered to be 0.16, roughly an order of magnitude smaller than in the estimate given above. This is reasonable since the stiffness induced through the geometry of the ring is not fully captured by the periodic boundary conditions.
Furthermore, the scaling relation for the fuzzy diameter can be used to obtain a scaling relation for the mean radius $\langle R \rangle$ of the wormlike ring. The mean radius is supposed to shrink if fluctuations are enabled [40]. As the length fluctuations $r_\parallel$ are subdominant to the transverse fluctuations, the mean radius yields:

$$\langle R \rangle = R_c \left(1 - \frac{\langle r_{\perp,i}^2 \rangle}{R_c^2} \right) \approx R_c \left(1 - 0.344 \frac{R_c}{l_p} \right) , \tag{2.30}$$

where again the estimate of the prefactor is larger than the true value as is presented in chapter 5.
Yamakawa et al. also derived the mean square diameter of a flexible ring and the mean square radius of gyration for both the stiff and the flexible regime of a polymer ring [48, 19]. To complete the picture of a tight ring, the mean square radius of gyration is cited:

$$\langle R_g^2 \rangle = R_c^2 \left(1 - 0.057 \frac{2\pi R_c}{l_p} \right) \approx \langle R^2 \rangle \,. \tag{2.31}$$

For a tight ring the center of mass is, to a good approximation, equal to the center of the ring, hence, the radius of gyration and the mean radius are identical in first order.

Although it is possible to describe some of the main features of a fluctuating ring by very simple means, a more distinct description of a ring subject to thermal undulations including anisotropic bending and twist stiffness, is desirable.

2.2.2 Kinematics of an elastic rod

To obtain an explicit representation of the trajectories $\mathbf{r}(s)$ of a ribbon with anisotropic bending stiffness and twist stiffness, we refer to the description of an elastic rod introduced in classical elasticity theory [31].
The rod of length L is regarded as inextensible with two bending stiffnesses a_1 and a_2, corresponding to bending about the two principal axes of inertia in the cross-sectional plane, and twist stiffness a_t. The unstressed state of the rod is taken to be straight. To specify a deformed state of the rod a local body coordinate system $\{\mathbf{t}_1(s), \mathbf{t}_2(s), \mathbf{t}_t(s)\}$ is assigned to every point $s \in [0, L]$ along the center line of the rod, such that the $\mathbf{t}_t(s)$ axis points tangent to the center line of the rod in the direction of increasing s, while $\mathbf{t}_1(s)$ and $\mathbf{t}_2(s)$ are aligned to the principal axes of the cross section. The inextensibility constraint is established by requiring:

$$\frac{d\mathbf{r}}{ds} = \mathbf{t}_t \,, \tag{2.32}$$

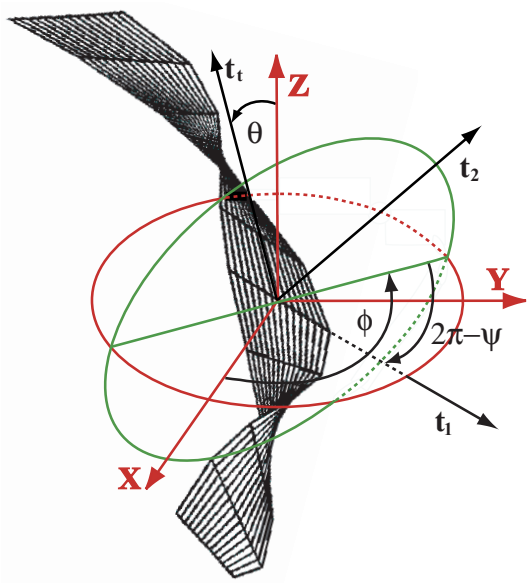

Figure 2.6: The fixed space coordinates $\{\mathbf{X}, \mathbf{Y}, \mathbf{Z}\}$, labelled red, can be brought into alignment with a single local body coordinate system $\{\mathbf{t}_1(s), \mathbf{t}_2(s), \mathbf{t}_t(s)\}$, stained black, along the trajectory of the ribbon [42] by a rotation about the Euler angles $\phi(s)$, $\theta(s)$ and $\psi(s)$. First, the space axes are rotated about their **Z**-axis by angle ϕ, such that the **X**-axis points in the direction of the line of nodes, marked in green, in the plane spanned by $\mathbf{t}_1$ and $\mathbf{t}_2$. Afterwards the new space coordinate axes are rotated about the line of nodes by angle θ, aligning **Z** with the tangent $\mathbf{t}_t$. Finally, the space axes are rotated about $\mathbf{t}_t$ by ψ such that **X** and **Y** become parallel to $\mathbf{t}_1$ and $\mathbf{t}_2$, respectively. For reasons of clarity the angle $2\pi - \psi$ instead of ψ is depicted in this drawing.

where $\mathbf{r}(s)$ is the space curve of the center line parameterized by s. A reference space coordinate system is given by $\{\mathbf{X}, \mathbf{Y}, \mathbf{Z}\}$. To compare the orientations of the space and the body system Euler angles ϕ, θ, ψ are employed. Rotating the space coordinate system about the Euler angles brings it into alignment with the body axes. This process is illustrated in Fig. 2.6, where the "x-convention" of the Euler angles is applied.
The red axes denote the space coordinate system, while the axes marked in black are the local body coordinate system of the ribbon at a position s of its center line. To bring the space axes into alignment with the body axes they are rotated in the following way. First, the space axes are rotated counterclockwise about their **Z**-axis by an angle ϕ, such that the new position of the **X**-axis, the line of nodes, painted in green, lies in the plane spanned by the body axes $\mathbf{t}_1$ and $\mathbf{t}_2$, indicated by a green ellipse. In the next stage, the new space axes are rotated about the line of nodes (green) counterclockwise by an angle θ to align the **Z** axis with the tangent of the ribbon $\mathbf{t}_t$. In the course of this rotation, the space axis **Y** becomes aligned to the plane spanned by $\mathbf{t}_1$ and $\mathbf{t}_2$, denoted by the green ellipse. In the final step, the new space coordinate axes **X** and **Y** are rotated counterclockwise about $\mathbf{t}_t$ by the Euler angle ψ to align with the principal axes of the cross-sectional plane, $\mathbf{t}_1$ and $\mathbf{t}_1$, respectively. Hence, the coordinates of the local body triad can be expressed in terms of the angles the space axes are rotated about, to transform the space to the body coordinates.

$$\mathbf{t}_1 = \begin{pmatrix} \cos\psi\cos\phi - \cos\theta\sin\phi\sin\psi \\ \cos\psi\sin\phi + \cos\theta\cos\phi\sin\psi \\ \sin\psi\sin\theta \end{pmatrix}, \tag{2.33}$$

$$\mathbf{t}_2 = \begin{pmatrix} -\sin\psi\cos\phi - \cos\theta\sin\phi\cos\psi \\ -\sin\psi\sin\phi + \cos\theta\cos\phi\cos\psi \\ \cos\psi\sin\theta \end{pmatrix}, \tag{2.34}$$

$$\mathbf{t}_t = \begin{pmatrix} \sin\theta\sin\phi \\ -\sin\theta\cos\phi \\ \cos\theta \end{pmatrix}. \tag{2.35}$$

Since the orientation of the local body axes changes along the trajectory of the rod, the Euler angles also vary with arc length position s : $\phi(s)$, $\theta(s)$, $\psi(s)$.
Two cross-sections separated by an infinitesimal distance Δs along the center line of the rod have their local axes infinitesimally rotated by an vector $\Delta\boldsymbol{\Omega}$. Therefore, the deformed state of the rod is determined by the set of infinitesimal rotations, which in the limit of $\Delta s \to 0$ is given by the "angular velocity":

$$\boldsymbol{\omega} = \lim_{\Delta s \to 0} \frac{\Delta\boldsymbol{\Omega}}{\Delta s} . \tag{2.36}$$

ω_1 and ω_2 may be interpreted as the curvatures in the principal directions, while ω_3 may be denoted the helical deformation density [3]. Using the definition of the infinitesimal rotations, the body coordinate axes can be related by the generalized Frenet equations,

$$\frac{d\mathbf{t}_1}{ds} = -\omega_2\mathbf{t}_t + \omega_3\mathbf{t}_2 , \quad \frac{d\mathbf{t}_2}{ds} = \omega_1\mathbf{t}_t - \omega_3\mathbf{t}_1 , \quad \frac{d\mathbf{t}_t}{ds} = -\omega_1\mathbf{t}_2 + \omega_2\mathbf{t}_1 . \tag{2.37}$$

The infinitesimal rotations $\boldsymbol{\omega}$ may be expressed in terms of the Euler angles. In the "x-convention" Euler's equations are [23]:

$$\omega_1 = \frac{d\phi}{ds}\sin\psi\sin\theta + \frac{d\theta}{ds}\cos\psi , \tag{2.38}$$

$$\omega_2 = \frac{d\phi}{ds}\cos\psi\sin\theta - \frac{d\theta}{ds}\sin\psi , \tag{2.39}$$

$$\omega_3 = \frac{d\phi}{ds}\cos\theta + \frac{d\psi}{ds} . \tag{2.40}$$

A derivation of the generalized Frenet equations based on the parameterization of the body coordinates in terms of Euler angles is presented in appendix A.1.

To elucidate the Euler angle representation of a deformable rod, several examples are shown. The best way to understand the Euler angles is to think of them as those angles by which the space coordinates are rotated to align to the local body coordinates, see Fig. 2.6. As the simplest example take all Euler angles equal to zero, hence, the local body coordinates do not change their direction along the rod's trajectory, as in the case of a stiff rod, see Fig. 2.7(a). Clearly, this state also minimizes the free elastic energy. If the Euler angles are changed to constant values not equal to zero, the rod is rotated within space but is not deformed. For instance, in Fig. 2.7(b) θ is chosen $\pi/2$ as well as ψ. Changing θ to $\pi/2$ provokes a rotation about the X-axis by $\pi/2$, the following change of ψ to $\pi/2$ causes a rotation about the Y-axis by $\pi/2$.

Now assume $\phi(s)$ to change linearly in s, $\phi(s) = 2\pi s/L$, then the rod from 2.7(b) is bend to form a ring lying tube-like in the xy-plane. This is the reference state for the calculations in chapter 3. Here, the local coordinate system is depicted such that the body vector $\mathbf{t}_1$ points

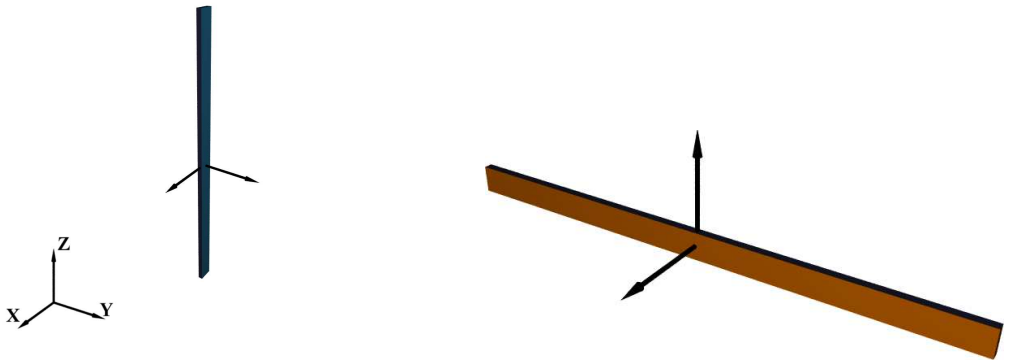

(a) Elastic rod for $\phi(s) = \theta(s) = \psi(s) = 0$.

(b) Elastic rod for $\phi(s) = 0$, $\theta(s) = \pi/2$ and $\psi(s) = \pi/2$.

Figure 2.7: Trajectories of an elastic rod for constant Euler angles. Changing the Euler angles form zero to constant angle $\pi/2$ causes a rotation about the X-axis and Y-axis for varying θ and ψ, respectively. Here and throughout this thesis the trajectories of a ribbon are painted blue and orange on the opposing long sides and dark blue and dark orange on the opposing short sides. The space axes are depicted as reference in (a).

into the direction of the major principle axis parallel to the z-axis. The Euler angle ψ indicates the angle between the xy-plane and the local axis $\mathbf{t}_1$. Hence, by choosing $\psi(s) = 0$ a disc-like ring as depicted in Fig. 2.8(b) is produced. To investigate how the ring structure changes if the Euler angles θ and ψ are altered linearly in s, we let the Euler angle $\psi(s) = \pi/2 + 2\pi s/L$ vary periodically keeping $\phi(s) = 2\pi s/L$ and $\theta(s) = \pi/2$ fixed. This produces a ring, which is twisted once around its center line, see Fig. 2.8(c). Setting θ equal to $\theta(s) = \pi/2 + 4\pi s/L$, while $\phi(s) = 2\pi s/L$ and $\psi(s) = \pi/2$ remain to generate the ring conformation, bends the ring off the xy-plane forming a saddle-like structure, see Fig. 2.8(d).

Recapitulating, the Euler angles are assigned to the deformations as

$\phi(s)$: azimuth angle depicting bending within the xy-plane
$\theta(s)$: polar angle characterizing bending out of the xy-plane
$\psi(s)$: twist angle describing the twist around the center line of the rod

2.2.3 Elastic free energy of a ribbon

Deforming a rod from its unstressed configuration requires energy. In the wormlike chain model the elastic free energy of a space curve, i.e. the polymer, was given by the squared curvature times the bending modulus, see Eq. (2.16), where the curvature of a space curve $\mathbf{r}(s)$ is given by its second derivative.
Considering an elastic rod or a ribbon with anisotropic bending stiffness and twist stiffness, the elastic free energy is supposed to be more sophisticated. The first two components of the "angular velocity" vector $\boldsymbol{\omega}$ can be interpreted as the curvatures in the principal directions

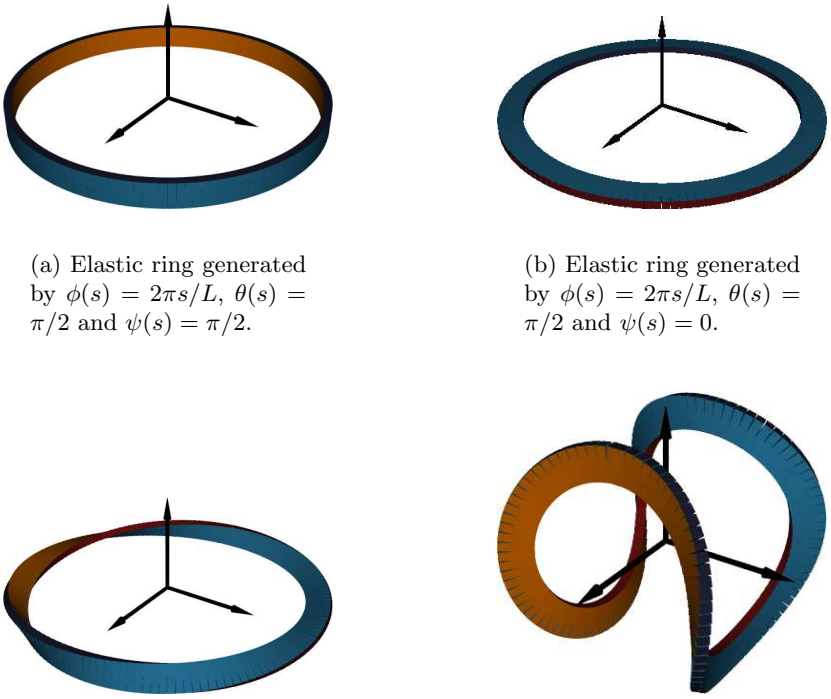

(a) Elastic ring generated by $\phi(s) = 2\pi s/L$, $\theta(s) = \pi/2$ and $\psi(s) = \pi/2$.

(b) Elastic ring generated by $\phi(s) = 2\pi s/L$, $\theta(s) = \pi/2$ and $\psi(s) = 0$.

(c) Elastic ring generated by $\phi(s) = 2\pi s/L$, $\theta(s) = \pi/2$, $\psi(s) = \pi/2 + 2\pi s/L$.

(d) Elastic ring generated by $\phi(s) = 2\pi s/L$, $\theta(s) = \pi/2 + 4\pi s/L$, $\psi(s) = \pi/2$.

Figure 2.8: Trajectories of an elastic ring for non-zero Euler angles. Letting $\phi(s)$ vary linearly with s creates a ring which is further modified, i.e. twisted or bend out of the xy-plane, by additionally altering $\psi(s)$ or $\theta(s)$ linearly with s.

of the cross-sectional plane, while the third component characterizes the helical deformation density. Hence, the elastic free energy of an anisotropic rod of length L is just the sum of all three contribution times the corresponding elastic moduli [31]:

$$F = \frac{1}{2}\int_0^L ds \left[I_1 E\omega_1^2 + I_2 E\omega_2^2 + C\omega_3^2\right], \tag{2.41}$$

where I_1 and I_2 denote the principal moments of inertia of the cross-sectional plane and E and C symbolize the elastic bending and torsional modulus, respectively. Analogous to the definition of the persistence length as the length over which the tangent-tangent correlation of a semiflexible polymer decays, three persistence lengths are now defined to characterize the fluctuations of a ribbon. a_1 and a_2 indicate the persistence lengths connected to the bending stiffness of the two principal axes of inertia, while a_t denotes the persistence length associated with the twist stiffness. Using this notation the elastic free energy of a ribbon can be written as:

$$F = \frac{k_B T}{2}\int_0^{2\pi R_c} ds \left[a_1\omega_1^2 + a_2\omega_2^2 + a_t\omega_3^2\right]. \tag{2.42}$$

For analytical calculations it is useful to express the components of the angular velocity in terms of Euler angles. Therefore, Eq. (2.42) is used in the analytic calculations of the statistical mechanics of ribbonlike rings in chapter 3. To simulate the fluctuations of a ribbon the description in terms of Euler angles is not adequate. A notation of the elastic free energy in space coordinates is preferable. Such an approach can be obtained by use of the Serret-Frenet equations and the generalized Frenet equations following the description of Panyukov and Rabin [42]. This mechanism is explained in the following paragraph.

Connecting the Serret-Frenet equation with the generalized Frenet equations to obtain an expression for the infinitesimal small rotations $\boldsymbol{\omega}(s)$ in terms of space coordinates rather than in Euler angles as before, the generalized Frenet equation are recalled. To characterize the fluctuations of a ribbon of non-circular cross section, local body coordinates $\{\mathbf{t}_i(s)\}$, $i = 1, 2, t$ are attached to each point s along the center line of the ribbon. $\mathbf{t}_t(s)$ is the tangent vector pointing along the center line and $\mathbf{t}_1(s)$ and $\mathbf{t}_2(s)$ are directed along the two principle axes of the cross-sectional plane, see Fig. 2.9.
The deformations of the ribbon may then be described by rotations $\boldsymbol{\omega}(s)$ of the unit triad, given by the generalized Frenet equations:

$$\frac{d\mathbf{t}_1}{ds} = -\omega_2\mathbf{t}_t + \omega_3\mathbf{t}_2 \,, \quad \frac{d\mathbf{t}_2}{ds} = \omega_1\mathbf{t}_t - \omega_3\mathbf{t}_1 \,, \quad \frac{d\mathbf{t}_t}{ds} = -\omega_1\mathbf{t}_2 + \omega_2\mathbf{t}_1 \,. \tag{2.43}$$

These equations, determining the configuration of a ribbon, are now compared with the equations that characterize the trajectory of a space curve.

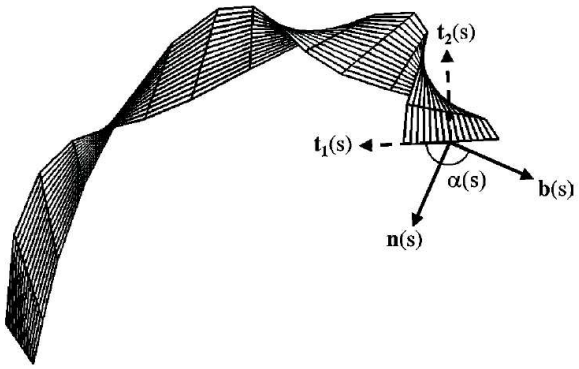

Figure 2.9: Drawing of a twisted ribbon [42]. The local body coordinate $\mathbf{t}_1(s)$ and $\mathbf{t}_2(s)$ point along the two principal axes of the cross-sectional plane while the normal $\mathbf{n}(s)$ and the binormal $\mathbf{b}(s)$ of the Frenet Trihedron of the space curve along the center line of the ribbon point in the direction of the gradient of the tangent and perpendicular to the tangent $\mathbf{t}_t(s)$ and the normal $\mathbf{n}(s)$, respectively.

To describe the conformations of a space curve parameterized by the arc length s one assigns another orthogonal triad namely the Frenet Trihedron, consisting of the tangent $\mathbf{t}$ of the curve, its normal vector $\mathbf{n}$ and its binormal vector $\mathbf{b}$, see Fig. 2.9. The tangent $\mathbf{t}$ is equal to the tangent of the local body coordinate system, $\mathbf{t}_t(s)$. The normal vector $\mathbf{n}(s)$ points into the direction of the gradient of the tangent, indicating the deviance of the curve from being a straight line. The binormal vector $\mathbf{b}(s)$ is perpendicular to both normal and tangent of the space curve completing the triad. All three vectors are interrelated by the Serret-Frenet

equations:

$$\frac{d\mathbf{b}}{ds} = -\tau\mathbf{n}\,, \quad \frac{d\mathbf{n}}{ds} = -\kappa\mathbf{t} + \tau\mathbf{b}\,, \quad \frac{d\mathbf{t}}{ds} = \kappa\mathbf{n}\,, \tag{2.44}$$

where $\kappa = \left|\frac{d\mathbf{t}}{ds}\right|$ denotes the curvature of the space curve and $\tau = \left|\frac{d\mathbf{b}}{ds}\right|$ its torsion. Identifying the center line of a ribbon with a space curve, we set $\mathbf{t} = \mathbf{t}_t$. Furthermore, one recognizes that the two frames are related by a rotation by an angle $\alpha(s)$ about the tangent of the ribbon, as depicted in Fig. 2.9. Hence, we may express $\mathbf{t}_1$ and $\mathbf{t}_2$ in terms of $\mathbf{b}$ and $\mathbf{n}$:

$$\mathbf{t}_1 = \mathbf{b}\cos(\alpha) + \mathbf{n}\sin(\alpha)\,, \quad \mathbf{t}_2 = -\mathbf{b}\sin(\alpha) + \mathbf{n}\cos(\alpha)\,. \tag{2.45}$$

Inserting these relations in Eqs. (2.43) and using Eq. (2.44) we obtain the angular velocities $\{\omega_i\}$ depending on curvature, torsion and angle α:

$$\omega_1 = -\kappa\cos(\alpha)\,, \quad \omega_2 = \kappa\sin(\alpha)\,, \quad \omega_3 = -\left(\tau - \frac{d\alpha}{ds}\right)\,. \tag{2.46}$$

Using the definition of curvature κ and torsion τ the elastic free energy of a ribbon becomes:

$$F = \frac{k_B T}{2}\int_0^L ds\left[a_1\left(\frac{d\mathbf{t}_t}{ds}\right)^2 + (a_2 - a_1)\left(\frac{d\mathbf{t}_t}{ds}\right)^2\sin^2(\alpha) + a_3\left(\left|\frac{d\mathbf{b}}{ds}\right| - \frac{d\alpha}{ds}\right)^2\right]. \tag{2.47}$$

This form of the elastic free energy of a ribbon is used in simulations, while the Euler angle description involving the infinitesimal small rotations $\boldsymbol{\omega}$ is used in the analytic calculations in the following chapter.

3 Fluctuations of a ribbonlike ring

In this chapter the effects of thermal fluctuations on a ribbonlike ring are examined analytically. Considering anisotropic bending stiffness and nonzero twist stiffness a full analysis of the modes of the ring is presented. Furthermore, an experimentally accessible parameter, the mean square diameter of the ring, is derived and investigated depending on the relative values of the bending and twisting stiffnesses. The analytic results for the mean square diameter are illustrated on physical grounds.

3.1 Elastic free energy of a tight ring

The fluctuations of a ribbonlike ring can be examined analytically when assuming small deviations from the conformation of a rigid ring. Having determined the ring conformation which minimizes the free energy of a ribbon, the elastic free energy of a tight ring is derived by approximating the latter. All terms in the elastic free energy are justified by explaining their role in detail. As a prerequisite for further investigations, the Fourier presentation of the energy is given.

3.1.1 Expanding for small fluctuations

To analyze the fluctuations of a ribbonlike ring analytically, the elastic free energy should be a polynomial of the variables, which, in the following description, are the Euler angles ϕ, θ and ψ. Otherwise the problem is intractable. Following the notation in section 2.2.3 the elastic free energy is the sum of the squared infinitesimal small rotations $\{\omega_i\}$, $i = 1, 2, 3$, which are related to sine and cosine products of the Euler angles as presented in 2.2.2. Hence, in general the elastic free energy is given by trigonometric functions of the Euler angles. To achieve an analytically tractable elastic free energy, the Euler angles are expanded around the rigid ring conformation, which minimizes the free energy.

To obtain a ring lying in the xy-plane, the Euler angle ϕ is set to $\phi_0 = s/R_c$ while $\theta_0 = \pi/2$, where R_c denotes the contour radius of the ring. The Euler angle ψ, indicating the opening angle between the xy-plane and the local $\mathbf{t}_1$ axis, seems free to choose, since the ring is closed for every opening angle. However, for the expansion the ground state ring conformation should be chosen such that the ring configuration minimizes the elastic free energy. To find the opening angle ψ_0 corresponding to the ground state, the elastic free energy of a ribbon with $\phi_0 = s/R_c$ and $\theta_0 = \pi/2$ is equated from Eq. (2.42) by use of the Euler equations Eqs. (2.40):

$$F = \frac{k_B T \pi}{R_c} \left(a_1 \sin^2 \psi_0 + a_2 \cos^2 \psi_0 \right). \tag{3.1}$$

Calculating the minimum for $\psi_0 \in [0, \pi]$, one finds that the position of the minimum depends on the ratio of the bending stiffnesses, a_1 and a_2. If $a_1 < a_2$ the minimum of the squared cosine at $\psi_0 = \pi/2$ becomes the absolute minimum. On the other hand, if $a_1 > a_2$ the minimum of the squared sine at $\psi_0 = 0$ becomes the absolute minimum, yielding, in summary, two ground state conformations. However, in both configurations the major principal axis of the cross-sectional plane is perpendicular to the xy-plane. Hence, both ground states are essentially the same, as can also be illustrated by the pictures in section 2.2.2.
The first ground state for $a_1 < a_2$ with $\psi_0 = \pi/2$ is pictured as a tube-like ring in Fig. 2.8(a). Directed parallel to the z-axis, the local body axis $\mathbf{t}_1$ is aligned to the major principal axis. This axis itself corresponds to the larger bending stiffness, which is in this case the persistence length a_2. If the opening angle ψ is changed to $\psi_0 = 0$, the local axis $\mathbf{t}_1$ is rotated to lie in the xy-plane, yielding a disk-like ring, as drawn in Fig. 2.8(b). However, this ring does not resemble the ground state for $a_1 > a_2$. The body axis $\mathbf{t}_1$ points into the direction where bending is stiffened by the persistence length a_2. However, in the disk-like ring the body axis $\mathbf{t}_1$ is pictured as the major principal axis, but is, in fact, the minor principal axis, since a_2 is now smaller than a_1. The major axis of the cross section of the ribbon is again aligned perpendicular to the xy-plane; the preferred configuration of the ribbonlike ring. Therefore, there is only one ground state, where the minor principal axis of the cross sectional plane lies in the xy-plane, while the major principal axis is perpendicular to it. In the following, the persistence length a_1 is taken to be smaller than a_2.

The unstressed state is assumed to be a straight rod in contrast to earlier work by Panyukov and Rabin [43], who took the ring geometry as unstressed. Considering small fluctuations of the Euler angles $\delta\theta$, $\delta\phi$ and $\delta\psi$ about their ground state conformation is valid for persistence lengths $\{a_k\}$, $k = 1, 2, t$ much larger than the radius R_c of the ring. Hence, we investigate a tight ribbonlike ring.
Expanding the Euler equations (2.40) around the ground state Euler angles, $\phi_0 = s/R_c, \theta = \pi/2, \psi = \pi/2$, yields:

$$\omega_1 \approx \frac{1}{R_c} + \frac{d\delta\phi}{ds} - \delta\psi\frac{d\delta\theta}{ds} - \frac{\delta\theta^2 + \delta\psi^2}{2\,R_c}\,, \tag{3.2}$$

$$\omega_2 \approx -\frac{d\delta\theta}{ds} - \frac{\delta\psi}{R_c} - \delta\psi\frac{d\delta\phi}{ds}\,, \tag{3.3}$$

$$\omega_3 \approx -\frac{\delta\theta}{R_c} + \frac{d\delta\psi}{ds} - \delta\theta\frac{d\delta\phi}{ds}\,. \tag{3.4}$$

For the elastic free energy all terms of quadratic order are taken into account, constant terms are neglected:

$$\begin{aligned} F &= \frac{k_B T}{2}\int_0^{2\pi R_c} ds\Bigg\{(a_2 - a_1)\left(\frac{\delta\psi}{R_c} + \frac{d\delta\theta}{ds}\right)^2 \\ &+ a_1\left[\left(\frac{d\delta\phi}{ds}\right)^2 - \left(\frac{\delta\theta}{R_c}\right)^2 + \left(\frac{d\delta\theta}{ds}\right)^2\right] + a_t\left(\frac{d\delta\psi}{ds} - \frac{\delta\theta}{R_c}\right)^2\Bigg\}\,. \end{aligned} \tag{3.5}$$

Looking closer at the free elastic energy, one may infer that $|a_2 - a_1|\delta\psi^2$ serves as a harmonic potential which drives the major principal axis to a direction perpendicular to the plane of the ring. To understand the precise role of each of those energy terms further, a detailed analysis is given in the following section.

In principle, it would also be possible to use another convention for the Euler angles, but the elastic free energy has proven to be invariant under changing the sequence of axes the system is rotated about in the definition of the Euler angles.

3.1.2 Analysis of the elastic free energy

To explain every single term in the expansion of the elastic free energy, the role of each Euler angle is recalled. To this purpose, the elastic free energy of the ring is separated into its three components, bending within the xy-plane, bending out of the xy-plane in z direction and twisting.

$$\begin{aligned} F &= \frac{a_1 k_B T}{2} \int_0^{2\pi R_c} ds \left[\left(\frac{d\delta\phi}{ds} \right)^2 - \left(\frac{\delta\theta}{R_c} \right)^2 + \left(\frac{d\delta\theta}{ds} \right)^2 - \left(\frac{\delta\psi}{R_c} + \frac{d\delta\theta}{ds} \right)^2 \right] \\ &+ \frac{a_2 k_B T}{2} \int_0^{2\pi R_c} ds \left(\frac{\delta\psi}{R_c} + \frac{d\delta\theta}{ds} \right)^2 + \frac{a_t k_B T}{2} \int_0^{2\pi R_c} ds \left(\frac{d\delta\psi}{ds} - \frac{\delta\theta}{R_c} \right)^2 \\ &= F_{\text{bend xy}} + F_{\text{bend z}} + F_{\text{twist}} \, . \end{aligned} \tag{3.6}$$

Three examples for deviations of the Euler angles from their ground state values are given in Fig. 3.1.

Euler angle ϕ is the azimuthal angle describing the bending of the ring within the xy-plane. Modifying ϕ is completely decoupled from twisting and bending the ring out of the xy-plane. Hence, $\delta\phi$ only contributes to $F_{\text{bend xy}}$ as in Fig. 3.1(a).
On the other hand, the angle θ characterizes the bending out-of-plane, and therefore increases the elastic free energy due to bending in z direction $F_{\text{bend z}}$. But changing θ also influences the elastic free energy due to bending within the xy-plane and due to twisting. As in Fig. 3.1(b) the contribution to the in-plane bending energy $F_{\text{bend xy}}$ is negative. This can be understood by imagining a ring which is already strongly bend within the xy-plane, adding a bending out of the ground state plane then releases the stress within the xy-plane, hence, a decrease in $F_{\text{bend xy}}$. Furthermore, bending out-of-plane induces a twist to the ring yielding non-zero F_{twist}.
Euler angle ψ depicts the twist of the ring, hence, the twisting energy F_{twist} is augmented, see Fig. 3.1(c). But again twisting induces the ring to bend in and out of the xy-plane. The bending stress in-plane is decreased by the releasing twist while the stress out-of-plane is increased.

Having gained an intuitive understanding of the influence of the Euler angles, the mathematical dependence of the elastic free energy terms on the Euler angles is analyzed next. The basic idea behind the analytical formulation is that all derivatives of the relative Euler angles $\delta\phi$, $\delta\theta$ and $\delta\psi$ incorporate the change of the Euler angles and therefore describe bending or twisting, respectively. The linear terms, all with respect to the contour radius R_c of the ring, provoke a release or increase of the corresponding elastic free energy term.
Starting with the very last term F_{twist}, these two effects can be demonstrated. Consider $\delta\theta = 0$, i.e. the ribbon is constrained to fluctuations in the xy-plane. In this case the twist is only described by the change of the twist angle, which is $d\delta\psi/ds$. Varying $\delta\theta$ induces additional twist, which is proportional to the height $\delta\theta$ gains above the xy-plane relative to

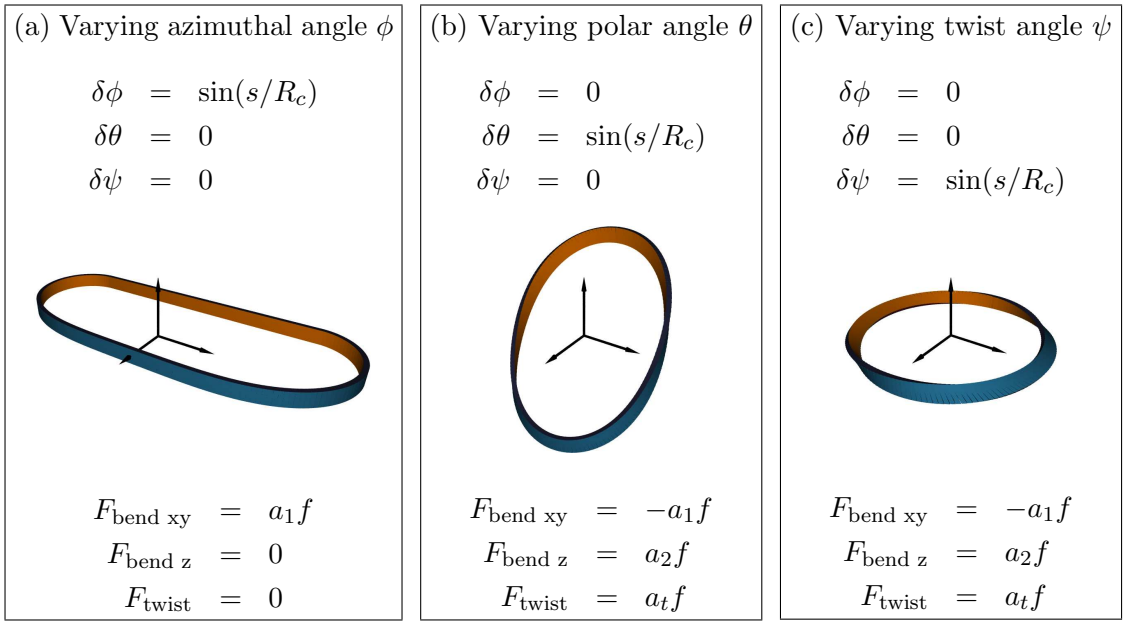

Figure 3.1: Examples for the contributions to elastic free energy from the variation of the Euler angles, where f is an abbreviation for $f = \pi k_B T/2R_c$. These examples also indicate the first non-zero sine modes of the single Euler angles as introduced later on.

the radius R_c of the ring, $\delta\theta/R_c$.
The same applies for the bending out-of-plane elastic free energy term $F_{\text{bend z}}$. Since $\delta\theta$ describes the fluctuation out of the xy-plane, $d\delta\theta/ds$ incorporates the bending out of the plane. But again, the bending out-of-plane can be increased or decreased by twist, which explains the sum of these two terms $(\delta\psi/R_c + d\delta\theta/ds)$. Both in F_{twist} and $F_{\text{bend z}}$, the two sums have been squared to account for the mirror symmetry of the ring with respect to the xy-plane.
The $F_{\text{bend xy}}$ term consists of several terms:

$$F_{\text{bend xy}} = \left(\frac{d\delta\phi}{ds}\right)^2 - 2\frac{\delta\psi}{R_c}\frac{d\delta\theta}{ds} - \left(\frac{\delta\theta}{R_c}\right)^2 - \left(\frac{\delta\psi}{R_c}\right)^2 . \tag{3.7}$$

Clearly, the derivative of the polar angle $\delta\phi$ contributes to the bending within the plane. However, this bending is reduced if the ribbon is twisted or bend out-of-plane, therefore terms proportional to the $\delta\psi$ and $\delta\theta$ relative to the radius of the ring are subtracted. In addition, a third term $2\frac{\delta\psi}{R_c}\frac{d\delta\theta}{ds}$ reduces the bending within the xy-plane, accounting for the fact that the release induced by the twist depends on the out-of-plane curvature at that point.

Previous work by Panyukov and Rabin [43] assumed the ring conformation as unstressed state. Comparing the elastic free energy derived in this thesis to their result shows that their free energy F_{PR} is lacking three terms.

$$F_{PR} = \frac{k_B T}{2}\int_0^{2\pi R_c} ds\left\{(a_2 - a_1)\left(\frac{\delta\psi}{R_c} + \frac{d\delta\theta}{ds}\right)^2 + a_1\left(\frac{d\delta\phi}{ds}\right)^2 + a_t\left(\frac{d\delta\psi}{ds} - \frac{\delta\theta}{R_c}\right)^2\right\} . \tag{3.8}$$

Hence, their free elastic energy term for bending within the xy-plane only involves the squared derivative of the angle ϕ and is therefore completely decoupled from twisting and out-of-

plane bending. However, their assumption does not apply to cytoskeletal filaments, whose conformation of zero energy is a straight rod.

In summary, all terms in the elastic free energy have a clear physical meaning. It is now of interest to investigate the statistics of a ribbonlike ring described by this elastic free energy. To this purpose the Euler angles are expanded in a Fourier series.

3.1.3 Boundary conditions and Fourier series representation

To expand the Euler angles in a Fourier series, appropriate boundary conditions due to the ring structure have to be met:

$$\delta\theta(2\pi R_c) = \delta\theta(0)\,, \quad \delta\phi(2\pi R_c) = \delta\phi(0)\,, \quad \delta\psi(2\pi R_c) = \delta\psi(0)\,, \tag{3.9}$$

for the Euler angles as well as for the three dimensional space curve of the center line: $\mathbf{r}(2\pi R_c) = \mathbf{r}(0)$. Since the position of the space curve at any point s is differing from its initial position at $s = 0$ by the sum, i.e. integral, of all tangents along its trajectory, the boundary condition can also be written in the integral form:

$$\mathbf{r}(2\pi R_c) - \mathbf{r}(0) = \int_0^{2\pi R_c} \mathbf{t}_t(s)\, ds = 0\,, \tag{3.10}$$

this is the constraint to be used in the following.
For small deviations from the equilibrium conformation the tangent vector $\mathbf{t}_t$ defined in Eq. (2.35) can be approximated to:

$$\mathbf{t}_t(s) = \begin{pmatrix} 0 \\ 0 \\ 1 \end{pmatrix} \delta\theta + \begin{pmatrix} \cos(s/R_c) \\ \sin(s/R_c) \\ 0 \end{pmatrix} \delta\phi + \begin{pmatrix} \sin(s/R_c) \\ -\cos(s/R_c) \\ 0 \end{pmatrix} \left[1 - \frac{\delta\theta^2 + \delta\phi^2}{2}\right]. \tag{3.11}$$

Taking only linear terms into account, the boundary conditions may be expressed as:

$$\int_0^{2\pi R_c} \delta\theta(s)\, ds = \int_0^{2\pi R_c} \delta\phi(s)\cos(s/R_c) ds = \int_0^{2\pi R_c} \delta\phi(s)\sin(s/R_c) ds = 0\,, \tag{3.12}$$

where the last two conditions can be summed up to:

$$\int_0^{2\pi R_c} \delta\phi(s)\, e^{-\mathrm{i}s/R_c} ds = 0\,. \tag{3.13}$$

This definition of the periodic boundary conditions can easily be transformed into a Fourier series representation.
Due to the periodicity of the Euler angles, they can be expanded in a Fourier series defined by:

$$\delta\eta(s) = \sum_n \delta\tilde{\eta}(n)\, e^{\mathrm{i}ns/R_c}, \quad \delta\tilde{\eta}(-n) = \delta\tilde{\eta}^*(n)\,, \tag{3.14}$$

for $\delta\eta = \delta\theta, \delta\phi, \delta\psi$. Since $\int_0^{2\pi R_c} e^{\mathrm{i}m\,s/R_c} ds = \delta_{m,0} 2\pi R_c$, the boundary conditions in Eqs. (3.12), (3.13) can be written as:

$$\delta\tilde{\theta}(0) = \delta\tilde{\phi}(1) = 0\,. \tag{3.15}$$

Applying the Fourier series to the elastic free energy and taking the periodic boundary conditions into account, Eq. (3.5) transforms to:

$$\begin{aligned} F &= \frac{k_B T \pi}{R_c} \Bigg\{ (a_2 - a_1) \, |\delta\tilde{\psi}(0)|^2 + (a_t + a_2 - a_1) \, |\mathrm{i}\delta\tilde{\theta}(1) + \delta\tilde{\psi}(1)|^2 \\ &+ \sum_{n=2}^{\infty} \Big[(a_2 - a_1) \, |\mathrm{i}n\delta\tilde{\theta}(n) + \delta\tilde{\psi}(n)|^2 + a_1 n^2 |\delta\tilde{\phi}(n)|^2 \\ &+ a_1 \left(n^2 - 1\right) |\delta\tilde{\theta}(n)|^2 + a_t |\mathrm{i}n\delta\tilde{\psi}(n) - \delta\tilde{\theta}(n)|^2 \Big] \Bigg\} . \end{aligned} \tag{3.16}$$

This elastic free energy of a ribbonlike ring can be used to extract the correlations and modes of the Euler angles via the equipartition theorem. For this purpose, it is reasonable to write the elastic free energy in a quadratic form. For $n \geq 2$ the quadratic form inside the sum can be represented as a matrix $A(n)$ in the space spanned by the Fourier components $\delta\tilde{\theta}(n), \delta\tilde{\phi}(n)$ and $\delta\tilde{\psi}(n)$:

$$A(n) = \begin{pmatrix} a_t + a_2 n^2 - a_1 & 0 & -\mathrm{i}n \left(a_t + a_2 - a_1\right) \\ 0 & a_1 n^2 & 0 \\ \mathrm{i}n \left(a_t + a_2 - a_1\right) & 0 & a_t n^2 + a_2 - a_1 \end{pmatrix} . \tag{3.17}$$

This results is used for the evaluation of the correlations of the Euler angles in the following section.
When introducing a new model it is compulsory to check one's approach by examining limiting cases which should reproduce known results from established models. In our case, the model of a ribbonlike ring is confirmed by recovering the wormlike chain in the limit of large rings as presented in appendix A.2.

3.2 Correlations of the Euler angles

In this section the correlations of the Euler angles are derived. From them the modes of the Euler angles can easily be read off. Furthermore, the correlations are used to derive the mean square diameter of the ring.
To extract the correlations of the Euler angles from the elastic free energy, the Fourier components $\delta\tilde{\eta}$ are expanded in terms of the eigenvectors ζ_k of matrix $A(n)$. Due to this procedure, the elastic free energy becomes diagonal and the equipartition theorem may be applied [43]. In summary, the correlations of the Euler angles can be expressed in terms of the eigenvectors ζ_k and the eigenvalues λ_k of the matrix $A(n)$:

$$\langle \delta\eta(s) \delta\eta(s') \rangle = \frac{R_c}{\pi} \sum_n e^{\mathrm{i}n(s-s')/R_c} \sum_k \frac{\zeta_k(n) \zeta_k'(-n)}{\lambda_k(n)} . \tag{3.18}$$

For the first modes $n = 0, \pm 1$ we obtain:

$$\sum_{n=0,\pm1} e^{in(s-s')/R_c} \sum_k \frac{\zeta_k(n)\zeta_k'(-n)}{\lambda_k(n)} = \frac{1}{a_2 - a_1} \begin{pmatrix} 0 & 0 & 0 \\ 0 & 0 & 0 \\ 0 & 0 & 1 \end{pmatrix} + \frac{1}{a_t + a_2 - a_1} \begin{pmatrix} \cos(s-s'/R_c) & 0 & -\sin(s-s'/R_c) \\ 0 & 0 & 0 \\ \sin(s-s'/R_c) & 0 & \cos(s-s'/R_c) \end{pmatrix} . \tag{3.19}$$

For $n \geq 2$ the following holds:

$$\sum_{n=2}^{\infty} e^{in(s-s')/R_c} \sum_k \frac{\zeta_k(n)\zeta_k'(-n)}{\lambda_k(n)} = A^{-1}_{\zeta\zeta'}(n) \, , \tag{3.20}$$

where A^{-1} is the inverse of matrix A, given by:

$$A^{-1}(n) = \begin{pmatrix} \frac{a_t n^2 + a_2 - a_1}{(n^2-1)(a_1(a_t+a_2-a_1)+a_t a_2(n^2-1))} & 0 & \frac{in(a_t+a_2-a_1)}{(n^2-1)(a_1(a_t+a_2-a_1)+a_t a_2(n^2-1))} \\ 0 & \frac{1}{a_1 n^2} & 0 \\ \frac{-in(a_t+a_2-a_1)}{(n^2-1)(a_1(a_t+a_2-a_1)+a_t a_2(n^2-1))} & 0 & \frac{a_t+a_2 n^2-a_1}{(n^2-1)(a_1(a_t+a_2-a_1)+a_t a_2(n^2-1))} \end{pmatrix} . \tag{3.21}$$

Now the correlations of the Euler angles can easily be calculated, yielding:

$$\begin{aligned} \langle \delta\phi(s_2)\delta\phi(s_1)\rangle &= \frac{R_c}{a_1\pi} \sum_{n=2}^{\infty} \frac{\cos(ns/R_c)}{n^2} \\ &= \frac{R_c}{a_1\pi} \left(\frac{(\pi - s/R_c)^2}{4} - \frac{\pi^2}{12} - \cos(s/R_c) \right) , \qquad (3.22) \\ \langle \delta\theta(s_2)\delta\theta(s_1)\rangle &= \frac{R_c}{\pi} \frac{\cos(s/R_c)}{a_t + a_2 - a_1} \\ &+ \frac{R_c}{\pi} \sum_{n=2}^{\infty} \frac{(a_t n^2 + a_2 - a_1)\cos(ns/R_c)}{(n^2-1)(a_1(a_t+a_2-a_1)+a_t a_2(n^2-1))} , \qquad (3.23) \\ \langle \delta\psi(s_2)\delta\psi(s_1)\rangle &= \frac{R_c}{\pi(a_2 - a_1)} + \frac{R_c}{\pi} \frac{\cos(s/R_c)}{a_t + a_2 - a_1} \\ &+ \frac{R_c}{\pi} \sum_{n=2}^{\infty} \frac{(a_t + a_2 n^2 - a_1)\cos(ns/R_c)}{(n^2-1)(a_1(a_t+a_2-a_1)+a_t a_2(n^2-1))} , \qquad (3.24) \\ \langle \delta\theta(s_2)\delta\psi(s_1)\rangle &= -\frac{R_c}{\pi} \frac{\sin(s/R_c)}{a_t + a_2 - a_1} \\ &+ \frac{R_c}{\pi} \sum_{n=2}^{\infty} \frac{(a_t + a_2 - a_1) n \sin(ns/R_c)}{(n^2-1)(a_1(a_t+a_2-a_1)+a_t a_2(n^2-1))} , \qquad (3.25) \end{aligned}$$

where $s = |s_2 - s_1|$. These results are now used to analyze the modes in terms of $\langle \delta\theta^2(n)\rangle$, $\langle \delta\phi^2(n)\rangle$ and $\langle \delta\psi^2(n)\rangle$.

3.3 Mode analysis

To comprehend the fluctuations of a ribbonlike ring, it is instructive to investigate its modes. As a prerequisite for the mode analysis, the Euler angles have been expanded in a Fourier

series, see Eq. (3.14). Hence, we assume the deviations of the Euler angles from their ground state values $\delta\eta$, $\eta = \phi, \theta, \psi$, to be a superposition of cosine and sine waves where the frequency is an integer multiple of s/R_c. The Fourier coefficients $\delta\tilde{\eta}(n)$ together with $\exp(\mathrm{i}ns/R_c)$ are denoted the Fourier modes or harmonics. Special interest lies in the absolute value of the Fourier coefficient since those indicate the amplitude by which every single wave is excited. As the Fourier coefficients alter with time, only predictions for the moments of the coefficients are possible. The mean of all modes is zero due to the isotropy of space, so only the mean square Fourier coefficients give an insight to the amplitude of the modes. These can easily be read off the correlations of the Euler angles in Eqs. (3.22), (3.23), (3.24) by setting $s = 0$.

For the constant mode $n = 0$ the results are:

$$\langle\delta\tilde{\phi}^2(0)\rangle = 0\,, \tag{3.26}$$

$$\langle\delta\tilde{\theta}^2(0)\rangle = 0\,, \tag{3.27}$$

$$\langle\delta\tilde{\psi}^2(0)\rangle = \frac{R_c}{a_2 - a_1}\,. \tag{3.28}$$

The ring is invariant to rotations about the z-axis, hence, a non-zero value of $\delta\phi(s)$ does not change the problem. It is therefore justified to set $\delta\phi(s)$ equal to zero. That the mean square amplitude of the $\delta\theta$ angle is zero as well follows from the periodic boundary conditions: For the closure of the ring the integral of $\delta\theta$ along the whole trajectory has to vanish, which cannot be achieved by a constant, nonzero $\delta\theta$. The Euler angle ψ_0 describes the initial angle between the major cross-sectional axis and the xy-plane. When calculating the elastic free energy it is found that the Euler angle ψ serves as a harmonic potential $(a_2 - a_1)\delta\psi^2$, driving the major axis to align perpendicular to the xy-plane. Therefore, the deviations from $\psi = \pi/2$ by $\delta\psi$ increase when the two stiffnesses become more and more equal, yielding a shallower potential. Note that $a_2 \geq a_1$, yielding a positive Fourier coefficient $\langle\delta\tilde{\psi}^2(0)\rangle$ as it should be. For $a_2 = a_1$ the cross sectional plane is a circle with no distinguished axis. Hence, $\langle\delta\tilde{\psi}^2(0)\rangle$ has no meaning anymore and diverges.
The first alternating mode $n = 1$ is defined by

$$\langle\delta\tilde{\phi}^2(1)\rangle = 0\,, \tag{3.29}$$

$$\langle\delta\tilde{\theta}^2(1)\rangle = \frac{R_c}{a_t + a_2 - a_1}\,, \tag{3.30}$$

$$\langle\delta\tilde{\psi}^2(1)\rangle = \frac{R_c}{a_t + a_2 - a_1}\,. \tag{3.31}$$

In this case, $\delta\tilde{\phi}(0) = 0$ due to the periodic boundary conditions and both $\delta\theta$ and $\delta\psi$ alternate in mean as depicted in the drawing in Fig. 3.2(b). The amplitudes are equal, becoming smaller for increasing twist stiffness and bending stiffnesses, as expected.
The amplitudes of the modes of the Euler angles for $n \geq 2$ can be written in a closed form:

$$\langle\delta\tilde{\phi}^2(n)\rangle = \frac{R_c}{a_1 n^2}\,, \tag{3.32}$$

$$\langle\delta\tilde{\theta}^2(n)\rangle = \frac{R_c(a_t n^2 + a_2 - a_1)}{(n^2-1)(a_1(a_t + a_2 - a_1) + a_t a_2(n^2-1))}\,, \tag{3.33}$$

$$\langle\delta\tilde{\psi}^2(n)\rangle = \frac{R_c(a_t + a_2 n^2 - a_1)}{(n^2-1)(a_1(a_t + a_2 - a_1) + a_t a_2(n^2-1))}\,. \tag{3.34}$$

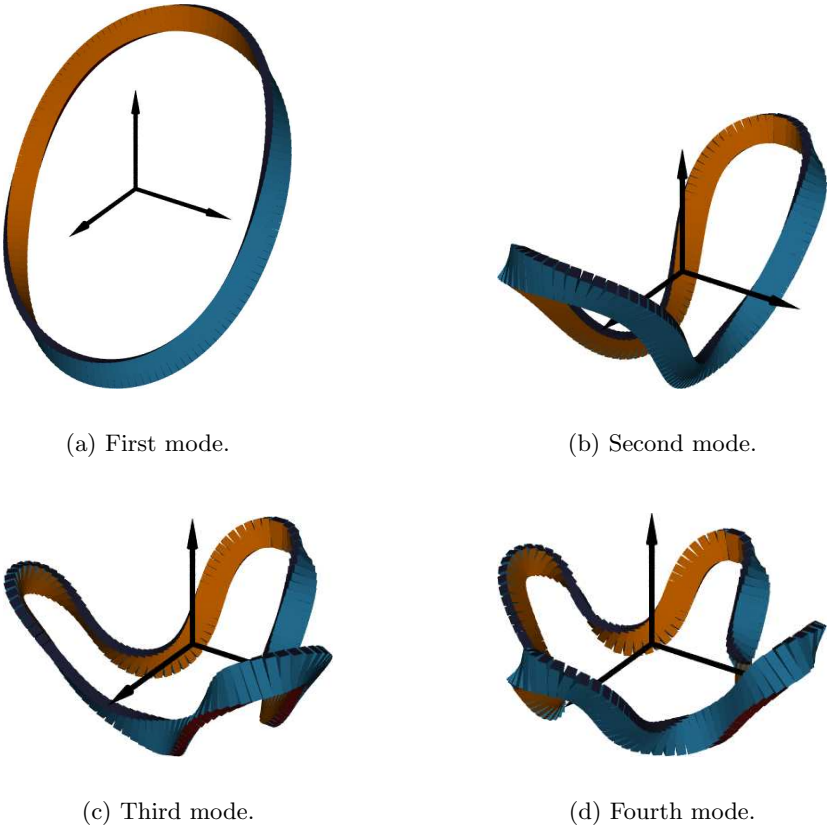

(a) First mode. (b) Second mode.

(c) Third mode. (d) Fourth mode.

Figure 3.2: The first four sine modes of the fluctuating ribbonlike ring, where the deviations from the ground state as depicted are exaggerated to give a clear impression of the modes.

The modes of the Euler angle $\delta\phi$ are simply decaying with increasing mode number n depending on the in-plane bending stiffness a_1 only, whereas the modes of the other Euler angles show a complicated behavior for small n depending on all three stiffnesses. For large n the modes of $\langle\delta\tilde{\theta}^2(n)\rangle$ are $(a_2 n^2)^{-1}$, those of $\langle\delta\tilde{\psi}^2(n)\rangle$ are $(a_t n^2)^{-1}$. The mean modes for $n = 2$ and $n = 3$ are depicted in Fig. 3.2(c)&(d). The higher the modes, the more "cloverleaves" appear and the more crumbled the whole ring becomes.
When using the modes in the following to calculate the mean square diameter, it becomes apparent that it is useful to introduce relative stiffness parameters. The latter are defined by a_1, a_2 and a_3 in the following way:

$$a_1\,, \quad \alpha = \frac{a_1}{a_2}\,, \quad \tau = \frac{a_1}{a_t}\,. \tag{3.35}$$

In these parameters the constraint $a_1 < a_2$ is given by $\alpha < 1$. Hence, the parameter space of α extends only up to one, while a_1 and τ may take values up to infinity. Using the new

variables, the amplitudes of the modes become:

$$\langle \delta\tilde{\phi}^2(n)\rangle = \frac{R_c}{a_1 n^2}\,, \tag{3.36}$$

$$\langle \delta\tilde{\theta}^2(n)\rangle = \frac{R_c}{a_1}\left[\frac{1}{n^2-1}+\frac{\alpha-1}{n^2+(1-\tau)(\alpha-1)}\right]\,, \tag{3.37}$$

$$\langle \delta\tilde{\psi}^2(n)\rangle = \frac{R_c}{a_1}\left[\frac{1}{n^2-1}+\frac{\tau-1}{n^2+(1-\tau)(\alpha-1)}\right]\,. \tag{3.38}$$

The modes are well defined in the parameter space with $\alpha \leq 1$, but divergences occur beyond it.
In the next section a new parameter is introduced that characterizes the fluctuations very well and can also serve as a measure in experiments: the mean square diameter of the ring. For its calculation the modes are employed.

3.4 Mean square diameter of the ring

Corresponding to the end-to-end distance of a wormlike chain, the mean square diameter $\langle D^2\rangle$ is the value that best characterizes the ribbonlike ring. In the first part of this section it is described how to calculate this quantity from the modes of the Euler angles.

When analyzing the modes of the ring, we found that the system can be characterized by introducing relative stiffnesses α, τ in addition to the in-plane bending stiffness a_1 as done in Eq. (3.35). To understand the mean square diameter in general, it is of importance to investigate limiting cases of those parameters. From the modes it is apparent that the in-plane bending stiffness crucially influences the fluctuations of a ribbonlike ring. For a_1 equal zero the modes diverge, and the approximation of small deviations from a rigid ring is not valid anymore. For a_1 to infinity there are no modes at all and the diameter is just twice the radius as for a rigid ring.
The impact of the relative stiffnesses and hence the out-of-plane bending stiffness a_2 and the twist stiffness a_t is more subtle. Therefore, the limiting cases of the relative stiffness are examined in detail. According to the parameter space the limiting cases are:

$$\alpha \to 1 \Leftrightarrow a_2 \to a_1\,, \qquad \alpha \to 0 \Leftrightarrow a_2 \to \infty\,,$$
$$\tau \to \infty \Leftrightarrow a_t \to 0\,, \qquad \tau \to 0 \Leftrightarrow a_t \to \infty\,,$$

where all other parameters are kept constant, respectively. Finally, the dependence of the mean square diameter on the relative stiffness is derived in general, approaching an understanding of the problem as depicted in Fig. 3.3. But before the characteristics of the mean square diameter can be discussed, an analytic formulation for the diameter of a fluctuating ribbonlike ring is derived.

3.4.1 Formula for the mean square diameter

The mean square diameter $\langle D^2\rangle$ of a fluctuating ring is the average distance in space between two points being separated by $\Delta s = \pi R_c$ along the center line of the ribbonlike ring of radius

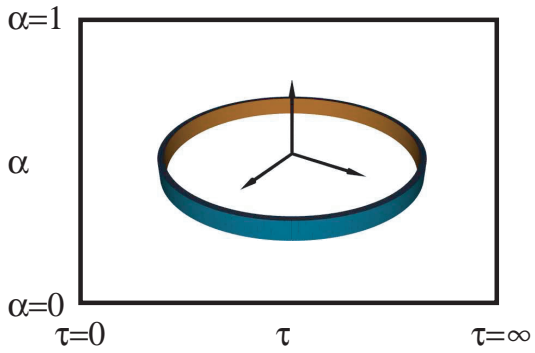

Figure 3.3: The approach to understand the mean square diameter of a ribbonlike ring starts with the examination of four limiting cases corresponding to the borders of the box above. In the end, the general mean square diameter is investigated, i.e. the inner part of the box.

R_c. The position $\mathbf{r}(s)$ of the center line at any point s is just the position of the center line at an initial point $s = 0$, $\mathbf{r}(0)$, plus the integral over all tangents along the trajectory between $s = 0$ and s, as in Eq. (3.10). Obtaining an analytic expression for the mean square diameter $\langle D^2 \rangle$ is thus related to the tangent-tangent correlation, which itself is associated to the correlations of the Euler angles derived earlier.

To derive the formula for the mean square diameter, first the tangent-tangent correlation is equated. Using the expansion of the tangent vector $\mathbf{t}_t$ in Eq. (3.11) yields:

$$\begin{aligned} \langle \mathbf{t}_t(s_1)\mathbf{t}_t(s_2)\rangle &= \langle \delta\theta(s_1)\delta\theta(s_2)\rangle + \langle \delta\phi(s_1)\delta\phi(s_2)\rangle \cos\left(\frac{|s_1 - s_2|}{R_c}\right) \\ &+ \left[1 - \langle \delta\theta^2\rangle - \langle \delta\phi^2\rangle\right] \cos\left(\frac{|s_1 - s_2|}{R_c}\right). \end{aligned} \tag{3.39}$$

Two components contribute to this tangent-tangent correlation. First the correlations of the Euler angles and second the correlation of the tangents due to the bend ground state conformation, i.e. the rigid ring. The product of two unit vectors tangent to a ring at angles s_1/R_c and s_2/R_c is just given by the cosine of the difference of the angles. Hence, the term $\cos(|s_2 - s_1|/R_c)$ in expression Eq. (3.39) arises from the rigid ring conformation.
As a further prerequisite to determine the mean square diameter of the ring, the mean square displacement of a position $\mathbf{r}(s)$ at point s along the center line of the ring versus another position along the center line, say $\mathbf{r}(0)$ at $s = 0$, is calculated. Using Eq. (2.32), $\langle (\mathbf{r}(s) - \mathbf{r}(0))^2 \rangle$ can be expressed as:

$$\langle (\mathbf{r}(s) - \mathbf{r}(0))^2 \rangle = \int_0^s dt \int_0^s dt' \langle \mathbf{t}_t(t)\mathbf{t}_t(t')\rangle \,. \tag{3.40}$$

Inserting the expression for the tangent-tangent correlation Eq. (3.39) into Eq. (3.40) and using the following integral

$$\int_0^s dt' \int_0^s dt \cos\left(n\frac{|t - t'|}{R_c}\right) = \frac{2r^2}{n^2}\left[1 - \cos\left(\frac{n\,s}{R_c}\right)\right]\Big|_{\frac{s}{R_c}=\pi} = \begin{cases} 0 & n \text{ even} \\ \frac{4r^2}{n^2} & n \text{ odd} \end{cases} . \tag{3.41}$$

yields:

$$\begin{aligned}\langle(\mathbf{r}(s)-\mathbf{r}(0))^2\rangle &= \int_0^s dt \int_0^s dt' \langle\delta\theta(t)\delta\theta(t')\rangle \\ &+ \int_0^s dt \int_0^s dt' \langle\delta\phi(t)\delta\phi(t')\rangle \cos\left(\frac{|t-t'|}{R_c}\right) \\ &+ \left[1-\left(\langle\delta\theta^2\rangle+\langle\delta\phi^2\rangle\right)\right] 2R_c^2(1-\cos(s/R_c)) \; . \end{aligned} \tag{3.42}$$

Note that again two components contribute, the fluctuations out of the ground state ring conformation and the mean square displacement of a rigid ring. For a rigid ring in the xy-plane, $\mathbf{r}(s)-\mathbf{r}(0)$ is given by:

$$\mathbf{r}(s)-\mathbf{r}(0) = \begin{pmatrix} R_c(1-\cos(s/R_c)) \\ R_c\sin(s/R_c) \\ 0 \end{pmatrix} . \tag{3.43}$$

Hence, the mean square displacement along a rigid ring yields:

$$(\mathbf{r}(s)-\mathbf{r}(0))^2_{\text{ring}} = 2R_c^2(1-\cos(s/R_c)) \; . \tag{3.44}$$

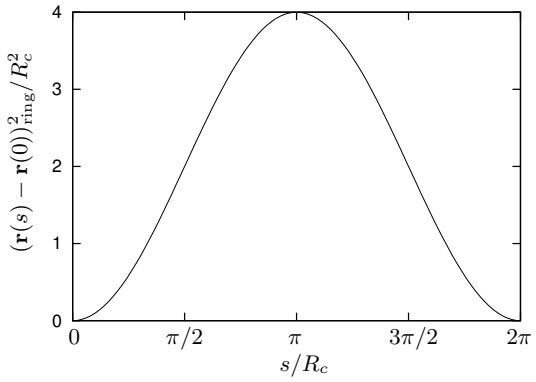

Figure 3.4: The mean square displacement of a fluctuating ribbonlike ring versus s/R_c. The displacement is maximized at $s/R_c=\pi$, hence, the mean square diameter best characterizes the fluctuations of the ring.

A plot of this function is shown in Fig. 3.4.
$(\mathbf{r}(s)-\mathbf{r}(0))^2_{\text{ring}}$ reaches a maximum at $s/R_c=\pi$ before descending to $s/R_c=2\pi$. Due to the fluctuations of the ring, the mean square displacement deviates slightly from the case of a rigid ring Eq. (3.44), but nevertheless the mean square displacement is maximized $s=\pi/R_c$. Therefore, the fluctuations of a ribbonlike ring are best characterized by the mean square displacement at $s/R_c=\pi$, i.e. the mean square diameter $\langle D^2\rangle$:

$$\begin{aligned}\langle D^2\rangle &= (2R_c)^2 + \int_0^s dt \int_0^s dt' \langle\delta\theta(t)\delta\theta(t')\rangle - 4R_c^2\langle\delta\theta^2\rangle \\ &+ \int_0^s dt \int_0^s dt' \langle\delta\phi(t)\delta\phi(t')\rangle \cos\left(\frac{|t-t'|}{R_c}\right) - 4R_c^2\langle\delta\phi^2\rangle \; . \end{aligned} \tag{3.45}$$

It is interesting to note that this formula still permits to trace the origin of the fluctuations. Since $\delta\theta$ measures the deflection from the xy-plane, the out-of-plane fluctuations are incorporated by the second and third term while the fourth and fifth term involving $\delta\phi$ originate

from the in-plane fluctuations. The first term states the diameter of a rigid ring.
Still, the formula for the mean square displacement involves integrals; solving them, an expression is deduced which only depends on the amplitudes of the $\delta\theta$ modes. The $\delta\theta$ angle correlations can be expressed in terms of the theta Fourier coefficients $\langle\delta\tilde{\theta}^2(n)\rangle$:

$$\langle\delta\theta(s_2)\delta\theta(s_1)\rangle = \frac{1}{\pi}\cos\left(\frac{|s_1-s_2|}{1}\right)\langle\delta\tilde{\theta}^2(n=1)\rangle + \frac{1}{\pi}\sum_{n=2}^{\infty}\cos\left(n\frac{|s_1-s_2|}{R_c}\right)\langle\delta\tilde{\theta}^2(n)\rangle\,. \quad (3.46)$$

Using the integral Eq. (3.41)and the double integral over the $\delta\theta$ correlations in Eq. (3.45) yields:

$$\int_0^s dt\int_0^s dt'\langle\delta\theta(t)\delta\theta(t')\rangle = \frac{4R_c^2}{\pi}\langle\delta\tilde{\theta}^2(n=1)\rangle + \frac{4R_c^2}{\pi}\sum_{n=2}^{\infty}\frac{\langle\delta\tilde{\theta}^2(2n-1)\rangle}{(2n-1)^2}\,. \quad (3.47)$$

The $\delta\phi$ correlations can be directly integrated using expression Eq. (3.22):

$$\begin{aligned}\int_0^s dt'\int_0^s dt\frac{R_c}{a_1\pi}&\left[\frac{\left(\pi-\frac{|t-t'|}{R_c}\right)^2}{4}-\frac{\pi^2}{12}-\cos\left(\frac{|t-t'|}{R_c}\right)\right]\cos\left(n\frac{|t-t'|}{R_c}\right)\\ &= \frac{R_c^3}{a_1\pi 12}\left[24\left(\frac{s}{R_c}-\pi\right)\sin\left(\frac{s}{R_c}\right)+3\left(\cos\left(\frac{2s}{R_c}\right)-1\right)+4(9-\pi^2)\left(\cos\left(\frac{s}{R_c}\right)-1\right)\right.\\ &\left.+6\frac{s}{R_c}\left(2\pi-\frac{s}{R_c}\right)\left(\cos\left(\frac{s}{R_c}\right)+1\right)\right]\Big|_{\frac{s}{R_c}=\pi} = \frac{2R_c^3}{a_1\pi 3}(\pi^2-9)\,. \end{aligned} \quad (3.48)$$

Substituting these results into Eq. (3.45) and expressing the second moment of $\delta\theta$ in terms of the amplitudes of the modes, the mean square diameter is given by:

$$\langle D^2\rangle = (2R_c)^2 - \frac{2R_c^3}{a_1\pi} + \frac{4R_c^2}{\pi}\sum_{\substack{n=3\\ n\text{ odd}}}^{\infty}\frac{\langle\delta\tilde{\theta}^2(n)\rangle}{n^2} - \frac{4R_c^2}{\pi}\sum_{n=2}^{\infty}\langle\delta\tilde{\theta}^2(n)\rangle\,. \quad (3.49)$$

The first term just denotes the diameter of a stiff ring, which is decreased due to fluctuations exhibited by the adjacent terms. The second term originates from $\delta\phi$ correlations and therefore describes the in-plane fluctuations, independent of the relative stiffnesses. The third and fourth term originate from $\delta\theta$ correlations and describe out-of-plane fluctuations. Hence, the in-plane fluctuations are completely decoupled from the out-of-plane bending stiffness and the twist stiffness and only decay to zero for infinite in-plane bending stiffness a_1. On the other hand the out-of-plane fluctuations depend on all three parameters a_1, α, τ, to be illuminated in the following sections, where limiting cases of the relative stiffnesses are considered.

3.4.2 Limiting cases for α

Here the limiting cases for the relative stiffness of in-plane bending stiffness to out-of-plane bending stiffness $a_1/a_2 = \alpha$ is examined. They are presented in the order $\alpha \to 1 \Leftrightarrow a_2 = a_1$, $\alpha \to 0 \Leftrightarrow a_2 \to \infty$, as introduced in section 3.4.

$\alpha \to 1$ - **equal bending stiffnesses**

In this section, the mean square diameter for equal bending stiffnesses is studied. This case is of both theoretical and experimental relevance since for equal bending stiffness the ribbonlike ring resembles a wormlike chain which has its ends interconnected. As becomes apparent soon, the twist stiffness is not involved any more, as expected for a wormlike chain. For further reference, this case will be denoted the *semiflexible ring*. Setting $\alpha = 1$, i.e. $a_1 = a_2 = l_p$ the modes of the Euler angle $\delta\theta$ become:

$$\langle \delta\tilde{\theta}^2(n) \rangle_{\alpha=1} = \frac{R_c}{l_p} \frac{1}{n^2 - 1} \,. \tag{3.50}$$

Substituting these modes into Eq. (3.49) yields:

$$\langle D^2 \rangle_{\alpha=1} = 4R_c^2 - \frac{2R_c^3}{l_p \pi} + \frac{4R_c^3}{l_p \pi} \sum_{\substack{n=3 \\ n \text{ odd}}}^{\infty} \frac{1}{n^2(n^2-1)} - \frac{4R_c^3}{l_p \pi} \sum_{n=2}^{\infty} \frac{1}{n^2 - 1} \,. \tag{3.51}$$

The sums are given by:

$$\sum_{\substack{n=3 \\ n \text{ odd}}}^{\infty} \frac{1}{n^2(n^2-1)} = \frac{10 - \pi^2}{8} \,, \quad \sum_{n=2}^{\infty} \frac{1}{n^2 - 1} = \frac{3}{4} \,. \tag{3.52}$$

Hence, the mean square diameter is:

$$\langle D^2 \rangle_{\alpha=1} = (2R_c)^2 \left(1 - \frac{1}{16} \frac{2\pi R_c}{l_p} \right) . \tag{3.53}$$

This result is up to one-hundredth identical to the result obtained by Shimada and Yamakawa for the mean square radius of gyration, see Eq. (2.31). Note further that the mean square diameter is independent of the twist stiffness, although no constraints where applied to the latter. This corresponds to the observation that the zeroth mode of the Euler angle $\delta\psi$ diverges for equal bending stiffness. Hence, the semiflexible ring has effectively no twist stiffness.
It is instructive to compare $\langle D^2 \rangle_{\alpha=1}$ with the end-to-end distance of a semiflexible polymer of length L and persistence length l_p, given by:

$$\langle R^2 \rangle = 2Ll_p \left[1 - \frac{l_p}{L} \left(1 - e^{-L/l_p} \right) \right] \overset{L \ll l_p}{\longrightarrow} L^2 \left[1 - \frac{1}{3} \frac{L}{l_p} + \mathcal{O}\left(\frac{L}{l_p} \right)^2 \right] . \tag{3.54}$$

Identifying the length of the polymer ring with $L = 2\pi R_c$, it is obvious that both the mean square diameter and the mean square end-to-end distance decay linearly in L/l_p in the limit of stiff chains. They just differ in the prefactor of the linear term, which is smaller for the ring, indicating that the ring is stiffer than the unconstrained semiflexible polymer, as expected, since the ring geometry induces additional stiffness.

$\alpha \to 0$ - **infinite out-of-plane bending stiffness**

To model an actin ring consisting of two coupled actin filaments, one would investigate the ribbon-like ring in the limit of $a_2 \to \infty$. In this case, the ring is completely rigid with respect

to fluctuations in the plane of the two actin filaments.
Setting $\alpha = 0$, Eq. (3.37) becomes:

$$\langle \delta\tilde{\theta}^2(n)\rangle_{\alpha=0} = \frac{R_c}{a_1}\left[\frac{1}{n^2-1} + \frac{1}{1-\tau-n^2}\right]. \tag{3.55}$$

Using this mode of the theta angle, the mean square diameter can directly be calculated with help of formula (3.49):

$$\begin{aligned}\langle D^2\rangle_{\alpha=0} &= 4R_c^2 - \frac{2R_c^3}{a_1\pi} - \frac{4R_c^3}{a_1\pi}\sum_{n=2}^{\infty}\left[\frac{1}{n^2-1} - \frac{1}{\tau-1+n^2}\right] \\ &+ \frac{4R_c^3}{a_1\pi}\sum_{\substack{n=3\\ n\text{ odd}}}^{\infty}\frac{1}{n^2}\left[\frac{1}{n^2-1} - \frac{1}{\tau-1+n^2}\right].\end{aligned} \tag{3.56}$$

As the out-of-plane bending stiffness is now set to infinity, the dependence of out-of-plane fluctuations on the parameters can be addressed again. The two terms involving the sums originate form the $\delta\theta$ correlation, and hence describe the fluctuations out-of-plane. If either a_1 or a_t approaches infinity, the out-of-plane fluctuations decay to zero, indicating that both bending in-plane and twisting together are necessary to bend this kind of ribbonlike ring out of the xy-plane.
To get further insight into the mean square diameter, Eq. (3.56) is split into a constant part, i.e. $4R_c^2$, and a linearly with R_c^3/a_1 decaying part $\partial\langle D^2\rangle_{\alpha=0}/\partial(R_c^3/a_1)$. This slope $\partial\langle D^2\rangle_{\alpha=0}/\partial(R_c^3/a_1)$ depends on τ only. This separation takes account of the dominating role of the in-plane bending stiffness a_1. If a_1 is infinite, there are no fluctuations at all, if a_1 vanishes the undulations of the ring exceed any tight ring approximation. This strong influence on the fluctuations of a ribbonlike ring is not exhibited by neither α ,i.e. the out-of-plane bending stiffness a_2, nor by τ, i.e. the twist stiffness. Calculating the sums in Eq. (3.56) by use of the formulas,

$$\begin{aligned}\sum_{\substack{n=3\\ n\text{ odd}}}^{\infty}\frac{1}{n^2(n^2+a)} &= -\frac{1}{1+a} + \frac{\pi^2}{8a} + \frac{\pi\tan(\pi\sqrt{-a}/2)}{4(-a)^{3/2}}\,, \\ \sum_{n=2}^{\infty}\frac{1}{n^2+a} &= -\frac{1+3a}{2a(1+a)} - \frac{\pi\cot(\pi\sqrt{-a})}{2\sqrt{-a}}\,,\end{aligned} \tag{3.57}$$

yields the slope $\partial\langle D^2\rangle_{\alpha=0}/\partial(R_c^3/a_1)$, see Fig. 3.5:

$$-\frac{\partial\langle D^2\rangle_{\alpha=0}}{\partial(R_c^3/a_1)} = -\frac{4+\tau\pi^2}{2\pi(1-\tau)} + \frac{2\cot(\pi\sqrt{1-\tau})}{\sqrt{1-\tau}} + \frac{\tan(\pi\sqrt{1-\tau}/2)}{(1-\tau)^{3/2}}\,. \tag{3.58}$$

The slopes magnitude is at its minimum value of $2/\pi$ at $\tau = 0$, i.e. $a_t = \infty$. For this value of τ, all fluctuations out-of-plane are suppressed, and hence the mean square diameter only depends on the in-plane bending stiffness:

$$\langle D^2\rangle_{\alpha=0,\tau=0} = (2R_c^2)\left(1 - \frac{R_c}{a_1 2\pi}\right). \tag{3.59}$$

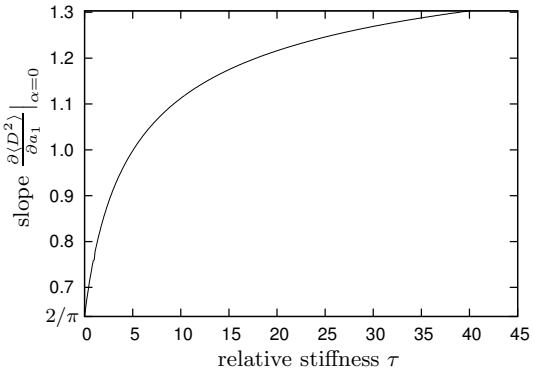

Figure 3.5: The mean square diameter decays linearly with $1/a_1$, but the slope $-\frac{\partial\langle D^2\rangle_{\alpha=0}}{\partial(R_c^3/a_1)}$ depends on τ in this limiting case of $\alpha = 0$. The slopes magnitude increases for increasing relative stiffness τ, i.e. decreasing twist stiffness.

For $\tau > 0$ the magnitude of the slope increases from its minimal value, decreasing the mean square diameter faster, since more and more out-of-plane modes are excited for decreasing twist stiffness a_t with respect to the in-plane bending stiffness a_1. For large τ, i.e. $a_3 \to 0$, the slope saturates at $\pi/2$. Hence, $\tau = \infty$ and $\alpha = 0$ yields a mean square displacement of:

$$\langle D^2\rangle_{\alpha=0,\tau=\infty} = (2R_c)^2\left(1 - \frac{1}{16}\frac{2\pi R_c}{a_1}\right). \tag{3.60}$$

This result is equal to the mean square diameter in the case of equal in-plane and out-of-plane bending stiffness, $\alpha = 1$, see Eq. (3.53). This means that the mean square diameter decays linearly with L/a_1, independent of whether both bending stiffnesses are equal or the out-of-plane bending stiffness is chosen infinity while the twist stiffness is zero. The second case can be explained by imagining a ribbonlike ring; though the out-of-plane bending stiffness is infinite, the ribbon behaves as if it would be a semiflexible ring of stiffness a_1. This is due to the zero twist stiffness. Imagine the ring twists by $\pi/2$, it will seems as if the ring has an out-of-plane bending stiffness of a_1. Hence, the ring fluctuates like a semiflexible ring.

Since only the slope of $\langle D^2\rangle_{\alpha=0}$ depends on τ, the mean square diameter depends more strongly on a_1 and varies only slightly with τ. This behavior is expected as a decrease in the twist stiffness only enables the ribbon to twist more, which does not result in large deflections out of the stiff ring conformation if $a_2 = \infty$.

Comparing the effect of the in-plane fluctuations to the out-of-plane fluctuations as before, one notes that the out-of-plane fluctuations are zero for $\tau = 0$, but increase for increasing τ, equalizing to the in-plane fluctuation for τ about thirty. When τ tends to infinity, the out-of-plane fluctuations become even about 1.5 times larger than the in-plane fluctuations. This is again an effect of the ring twisting. If a ring is twisting almost freely, out-of-plane can easily be performed. The fluctuations in-plane become smaller than the out-of-plane fluctuations since they are subject to the geometric constraint of the ring, which does not affect the deflections out-of-plane so strongly.

3.4.3 Limiting cases for τ

Having found interesting behavior in the limiting cases of α, the limiting cases of τ are investigated. First, $\tau \to 0 \Leftrightarrow a_t \to \infty$ is examined, followed by an analysis of the mean square diameter of $\tau \to \infty \Leftrightarrow a_t \to 0$.

$\tau \to 0$ - **infinite twist stiffness**

What happens, when the twist stiffness becomes infinitely large? To answer this question the mean square diameter for $\tau \to 0$ is equated.

The modes of Euler angle theta for $\tau = 0$ are:

$$\langle \delta\tilde{\theta}^2(n) \rangle_{\tau=0} = \frac{R_c}{a_1} \left[\frac{1}{n^2 - 1} + \frac{\alpha - 1}{n^2 + \alpha - 1} \right]. \tag{3.61}$$

Inserting these modes of the theta angle into the formula Eq. (3.49) the mean square diameter is calculated to:

$$\begin{aligned} \langle D^2 \rangle_{\tau=0} &= 4R_c^2 - \frac{2R_c^3}{a_1\pi} - \frac{4R_c^3}{a_1\pi} \sum_{n=2}^{\infty} \left[\frac{1}{n^2 - 1} + \frac{\alpha - 1}{n^2 + \alpha - 1} \right] \\ &+ \frac{4R_c^3}{a_1\pi} \sum_{\substack{n=3 \\ n \text{ odd}}}^{\infty} \frac{1}{n^2} \left[\frac{1}{n^2 - 1} + \frac{\alpha - 1}{n^2 + \alpha - 1} \right]. \end{aligned} \tag{3.62}$$

As beforehand, the mean square diameter mainly depends on a_1 and decreases linearly with R_c^3/a_1, while the slope now depends on α. Evaluating the sums with formulas Eqs. (3.52), (3.57) the slope is calculated to:

$$-\frac{\partial \langle D^2 \rangle_{\tau=0}}{\partial (R_c^3/a_1)} = -\frac{2}{\pi} + 2\sqrt{1-\alpha}\cot(\pi\sqrt{1-\alpha}) + \frac{\tan(\pi\sqrt{1-\alpha}/2)}{\sqrt{1-\alpha}}\,. \tag{3.63}$$

The slope for $\tau = 0$ versus α is depicted in Fig. 3.6. Starting from $2/\pi$ for infinite out-of-plane bending stiffness and infinite twist stiffness the slope increases to $\pi/2$ at in-plane bending stiffness equal out-of-plane bending stiffness. For both $\tau = 0$ and $\alpha = 0$ no fluctuations out of the xy-plane are possible and the diameter decreases only due to undulations in the xy-plane. These in-plane fluctuations correspond to a slope of $2/\pi$. When α grows, i.e. if the out-of-plane bending stiffness a_2 is decreased, more and more fluctuations perpendicular to the ground state plane of the ring are enabled, decreasing the diameter faster and faster, as the slope increases. Remarkably, the proportion of the out-of-plane fluctuations exceeds the proportion of the in-plane undulations for $a_2 < a_1$. The out-of-plane fluctuations are as high as the in-plane modes for $a_2 = 1.5a_1$ roughly. Although the out-of-plane bending stiffness is still one a half times larger than the in-plane bending stiffness and although twisting is impossible the out plane fluctuations are as large as the in-plane ones, this is due to the stiffness induced by the geometry of the ring, which dominantly affects the amplitude of the in-plane fluctuations.

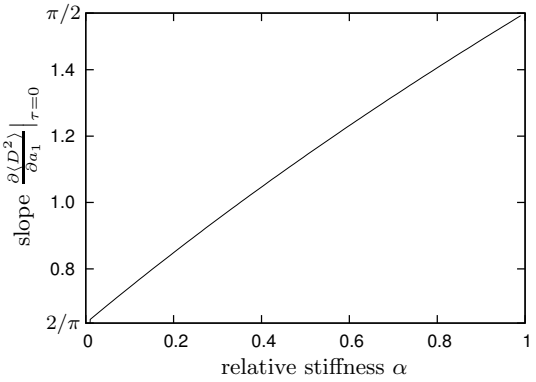

Figure 3.6: The slope of the mean square diameter $-\frac{\partial\langle D^2\rangle}{\partial(R_c^3/a_1)}$ in the limiting case of $\tau = 1$ according to Eq. (3.63). Increasing α, i.e. decreasing the out-of-plane bending stiffness, more and more out-of-plane modes are excited and the slope by which the diameter declines grows.

$\tau \to \infty$- zero twist stiffness

Setting the twist stiffness to zero enables the ribbonlike ring to unhindered twisting, such that any difference between the out-of-plane bending stiffness a_2 and the in-plane bending stiffness a_1 concerning the out-of-plane fluctuations is washed out, resulting in a mean square diameter which only depends on the smallest stiffness, the in-plane bending stiffness, as derived in section 3.4.2.

3.4.4 The general mean square diameter

After the analysis of all limiting cases, the general mean square displacement is investigated. Inserting the amplitudes of the theta modes Eq. (3.33) into Eq. (3.49) the general mean square diameter yields:

$$\begin{aligned}\langle D^2\rangle &= 4R_c^2 - \frac{2R_c^3}{a_1\pi} - \frac{4R_c^3}{a_1\pi}\sum_{n=2}^{\infty}\left[\frac{1}{n^2-1} + \frac{\alpha-1}{n^2+(1-\tau)(\alpha-1)}\right] \\ &+ \frac{4R_c^3}{a_1\pi}\sum_{\substack{n=3\\ n\text{ odd}}}^{\infty}\frac{1}{n^2}\left[\frac{1}{n^2-1} + \frac{\alpha-1}{n^2+(1-\tau)(\alpha-1)}\right].\end{aligned} \tag{3.64}$$

In this general case, the mean square diameter decreases linearly with R_c^3/a_1, where now the slope $-\partial\langle D^2\rangle/\partial(R_c^3/a_1)$ depends on both α and τ. Using the formulas for the sums given in Eqs. (3.52), (3.57), the slope is calculated to:

$$\begin{aligned}-\frac{\partial\langle D^2\rangle}{\partial(R_c^3/a_1)} &= \frac{4+\pi^2\tau}{2\pi(\tau-1)} - 2\sqrt{\frac{1-\alpha}{1-\tau}}\cot(\pi\sqrt{(1-\alpha)(1-\tau)}) \\ &\quad -\frac{\tan(\pi\sqrt{(1-\alpha)(1-\tau)}/2)}{\sqrt{(1-\alpha)(1-\tau)^3}}\,.\end{aligned} \tag{3.65}$$

Now the limiting cases determined beforehand have the important role to check this result. A contour plot of the slope versus both relative stiffnesses α and τ is shown in Fig. 3.7. The

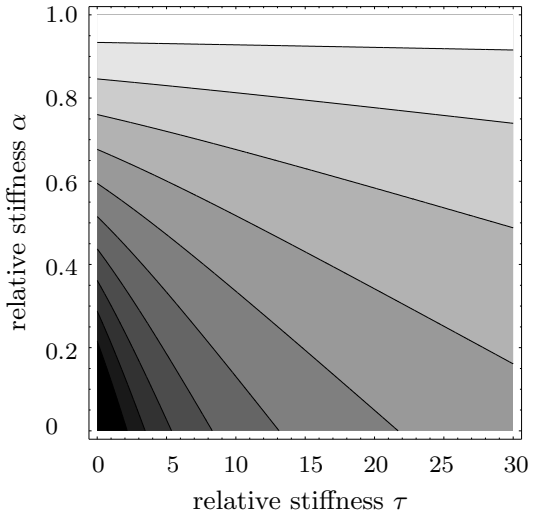

Figure 3.7: Contour plot of the slope of the mean square diameter $-\frac{\partial\langle D^2\rangle}{\partial(R_c^3/a_1)}$ versus α and τ, where the contour lines decrease from $\pi/2$ to $2/\pi$ in ten equal steps. Four limiting cases are recovered. For $\alpha = 0$ the slope increases at first fast and saturates at a constant value for infinite τ, verified by the growth of the distance of the contour lines. In the case of $\alpha = 0$ an almost linear decay is forecasted, confirmed by the equal distances of the contour lines. For $\alpha = 1$ $\langle D^2\rangle$ is independent of τ, hence, the contour is parallel to the τ-axis.

slope increases from its minimal value of $2/\pi$ for $\tau = 0, \alpha = 0$ to its maximal value of $\pi/2$ at $\tau = \infty, \alpha = 1$. The limiting cases are recovered at the boundaries of the parameter intervals. For $\alpha = 0$ the slope is forecast to increase slower and slower with τ, saturating at $2/\pi$. This is recovered, since the distance of the contour lines in Fig. 3.7 grows with τ. For $\tau = 0$ the slope increases almost linearly with α as indicated by the equal distance of the contour lines. For both $\tau = \infty$ and $\alpha = 1$ the slope is at its maximum value of $\pi/2$ as predicted. The almost horizontal contour lines in Fig. 3.7 decline with τ, such that the slope is equal $\pi/2$ at $\tau = \infty$. All these limits are also obtained analytically from Eq. (3.65).

The dominating role in decreasing the mean square diameter by fluctuations is played by the in-plane bending stiffness a_1. If it is infinite no undulations occur, if it vanishes the fluctuations exceed the tight ring approximation. The second prominent role is taken by the out-of-plane bending stiffness a_2. Together with the twist stiffness a_t it regulates the amount of out-of-plane fluctuation. The undulations perpendicular to the xy-plane are important for a considerable decline of the diameter, since they are not so much affected by the additional stiffness induced by the geometry of the ring, which stiffens the in-plane fluctuations. The deviations out of the xy-plane exceed those in-plane, when $\tau = 0, \alpha \approx 0.65$ or $\tau \approx 28, \alpha = 0$ or both of them on the contour line connecting those two points on the axes in Fig. 3.7. This also indicates why the role of the out-of-plane bending stiffness is more important than the one of the twist stiffness, although they are coupled. The twist stiffness has to be decreased to much smaller values to obtain the same small diameter, as can be achieved with a relatively high out-of-plane bending stiffness a_2, respectively. Furthermore, the slope is not as sensitive to small changes of the relative value of the twist stiffness τ as it is to small changes of the relative bending stiffness α.
Closing the analytic calculations with the above discussion of the mean square diameter and

its slope, we proposed a complete model for tight fluctuating ribbonlike rings, considering the function of in-plane and out-of-plane bending stiffness as well as twist stiffness in detail.

3.5 Rings with intrinsic twist

When connecting the ends of a ribbon to form a ring, one can match the ends such that no intrinsic twist is involved as has been assumed up to now. Alternatively, one end can bind to the other end forming a Möbius strip or when allowing for nicked rings all kinds of mismatched interconnections are possible. The number of times the ribbon is twisted before its ends are connected is called the linking number Lk. For a closed ring the linking number can be defined as:

$$\mathrm{Lk} = \int_0^{2\pi R_c} \frac{d\psi(s)}{ds} = \psi(2\pi R_c) - \psi(0) = \frac{\alpha_{Lk}}{2\pi} \,, \tag{3.66}$$

which is just the imposed twist angle at $s = 2\pi R_c$ relative to the twist angle at $s = 0$, denoted α_{Lk}. Including nonzero linking numbers serves to couple in and out-of-plane fluctuations [52], so new properties of the ring arise. The idea of nicked rings has been studied for DNA strands with intrinsic helical structures [35, 24, 3]. It could also be illuminating to study the linking number dependence of the fluctuations of ribbonlike rings with no helical structure but anisotropic bending stiffness as in the model presented in this chapter.
The concept of a mismatched closed ring can easily be incorporated in the model by requiring the ground state twist angle to be:

$$\psi_0(s) = \frac{\alpha_{Lk}}{2\pi}\frac{s}{R_c} + \psi_{00} \,, \tag{3.67}$$

where ψ_{00} is the former ground state twist angle, i.e. $\psi_{00} = \pi/2$. Proceeding analogous to section 3.1, expanding around the new equilibrium conformation the elastic free energy yields:

$$\begin{aligned} F = \frac{k_B T}{2} \int_0^{2\pi R_c} ds \Bigg\{ & (a_2 - a_1) \cos\left(\frac{\alpha_{Lk}}{\pi}\frac{s}{R_c}\right) \left(\frac{\delta\psi}{R_c} + \frac{d\delta\theta}{ds}\right)^2 \\ & + \left(a_1 \cos^2\left(\frac{\alpha_{Lk}}{2\pi}\frac{s}{R_c}\right) + a_2 \sin^2\left(\frac{\alpha_{Lk}}{2\pi}\frac{s}{R_c}\right)\right) \left[\left(\frac{d\delta\phi}{ds}\right)^2 - \left(\frac{\delta\theta}{R_c}\right)^2 + \left(\frac{d\delta\theta}{ds}\right)^2\right] \\ & + (a_2 - a_1) \sin\left(\frac{\alpha_{Lk}}{\pi}\frac{s}{R_c}\right) \left[2\frac{\delta\psi}{R_c} + \frac{d\delta\theta}{ds}\right] \frac{d\delta\phi}{ds} + a_t \left[\left(\frac{d\delta\psi}{ds} - \frac{\delta\theta}{R_c}\right)^2 - \frac{\alpha_{Lk}}{\pi R_c}\delta\theta\frac{d\delta\phi}{ds}\right] \Bigg\} \,. \end{aligned}$$

Obviously the elastic free energy has become more evolved but is still accessible to further analysis to be done in future work. Previous to an investigation of the statistical mechanics of fluctuating nicked rings a thorough calculation of the configurations that minimize the elastic free energy should be pursued.

In the following chapter, simulation techniques are introduced, which are applied to investigate the quality of the analytic predictions. So far, only the limiting case of equal in-plane and out-of-plane bending stiffness, $\alpha = 1$, has been simulated. However, the semiflexible ring yields additional interesting features, to be discussed in chapter 5.

4 Simulation techniques

Analytic calculations are often limited, allowing only asymptotically fulfilled scaling laws. In those cases simulations provide the opportunity to go beyond the analytic predictions.
In the model for fluctuating ribbonlike rings in chapter 3, the fluctuations were approximated to be small with respect to the rigid ring conformation. Applying simulations also flexible configurations of the ring become examinable. Furthermore, the simulations are employed to assess the quality of the approximation.
To investigate the equilibrium statistical mechanics of fluctuating rings, the method of choice is Monte Carlo simulations. By drawing random numbers a Monte Carlo simulation generates sample configurations, from which estimates of some properties of the system can be obtained by averaging.
In this chapter, at first, the Metropolis Monte Carlo method is introduced, giving an account of conditions that have to be met when designing a Metropolis Monte Carlo simulation. Furthermore, the correlations and errors arising from the simulation data are discussed. Finally, the implementation of a fluctuating semiflexible ring is explained.

4.1 The Monte Carlo method

Monte Carlo simulations are a class of computational algorithms, whose implementations use random number generators to obtain stochasticity; for a good overview see reference [18]. Among those, the Metropolis algorithm [38] has proven to be very effective in simulating, amongst others, thermodynamic properties of biological systems on large time scales. In this section, the Metropolis algorithm is explained along with conditions such as detailed balance and ergodicity that have to be met by an implementation. An account of the error estimates for the averages of the simulation data is also presented.

4.1.1 From simple sampling to Metropolis algorithm

In statistical physics, a system can be well characterized by averages of representative parameters. Working in a canonical ensemble with constant temperature T, the expectation value of any observable A is given by:

$$\langle A \rangle = \frac{\int_\Omega d\mathbf{x}\, A(\mathbf{x})\, e^{-\beta H(\mathbf{x})}}{\int_\Omega d\mathbf{x}\, e^{-\beta H(\mathbf{x})}} \,, \tag{4.1}$$

where Ω denotes the configuration space. Note that for our purposes the Hamiltonian $H(\mathbf{x})$ is only known for equilibrated states.

Using simple sampling Monte Carlo, one can solve an integral by choosing random configurations $\{\mathbf{x}\}$, evaluating the integrand of those random configurations and averaging the integrand over all trials. If the integrand is almost constant, the accuracy with which this method estimates the true value of the integral increases with the inverse square root of the total number of trials.
However, in the case of a nonzero Hamiltonian, the integrand may vary strongly within the configuration space, since the probability for the occurrence of a certain state in the configuration space is given by the Boltzmann distribution. Assuming the Boltzmann distribution to be highly peaked, the simple sampling Monte Carlo method will most of the time generate configurations with very small contributions to the integral. To sample the major contributions one has to choose the configurations according to the Boltzmann distribution, using so-called importance sampling.
Metropolis et al. [38] invented an algorithm where conformations $\{\mathbf{x}\}$ are drawn with a probability of $\exp(-\beta H(\mathbf{x}))$. The Metropolis method can be understood as a random walk in configuration space, where the probability to visit a point $\mathbf{x}$ is proportional to the Boltzmann weight. Starting off a configuration $\mathbf{x}_{old}$ the algorithm randomly generates a new conformation $\mathbf{x}_{new}$ with attempt probability $\alpha(\mathbf{x}_{old} \rightarrow \mathbf{x}_{new})$. If the energy of the new state is smaller than the old one's, the new configuration is accepted. If the energy of $\mathbf{x}_{new}$ is larger than the old conformation's, the new state is accepted with an probability of $\exp(-\beta[H(\mathbf{x}_{new}) - H(\mathbf{x}_{old})])$, i.e. a random number $r \in [0, 1)$ is drawn, if $r < \exp(-\beta[H(\mathbf{x}_{new}) - H(\mathbf{x}_{old})])$ the new conformation is accepted, otherwise it is rejected. Even if the new conformation $\mathbf{x}_{new}$ is not admitted, the state the system resides in after the procedure is taken as a new conformation for the purpose of taking averages. Calculating the average of a parameter only gives an estimate of the true expectation value and approaches the expectation value in the limit of infinite samples. Therefore considerations concerning the error of the average have to be made.
Summarizing, the Metropolis algorithm is given by:

1. choose an initial conformation,
2. perform a move to produce a new configuration $\mathbf{x}_{new}$ out of $\mathbf{x}_{old}$,
3. calculate the difference in energy between the new conformation and the old one,
4. accept the new conformation with probability
   $P_{acc}(\mathbf{x}_{old} \rightarrow \mathbf{x}_{new}) = \min\{1, \exp(-\beta[H(\mathbf{x}_{new}) - H(\mathbf{x}_{old})])\}$, and return to step 2,
5. take samples for averaging after a specific number of steps.

4.1.2 Detailed balance and ergodicity

In order to have a sequence of states generated by the Metropolis algorithm satisfying the distribution of a canonical ensemble in thermal equilibrium, some conditions have to be imposed.
Producing the sequence of states in a Markovian stochastic process, the probability to be at

point $\mathbf{x}$ in configuration space after k steps, $\rho_k(\mathbf{x})$, is described by a master equation:

$$\begin{aligned}\rho_k(\mathbf{x}) - \rho_{k-1}(\mathbf{x}) &= \sum_{\mathbf{x}'} \rho_{k-1}(\mathbf{x}') P_{acc}(\mathbf{x}' \to \mathbf{x}) \alpha(\mathbf{x}' \to \mathbf{x}) \\ &- \sum_{\mathbf{x}'} \rho_{k-1}(\mathbf{x}) P_{acc}(\mathbf{x} \to \mathbf{x}') \alpha(\mathbf{x} \to \mathbf{x}') \,, \end{aligned} \tag{4.2}$$

where the transition probabilities consist of the product of attempt probability α and acceptance probability P_{acc}. To obtain an equilibrium distribution, the master equation should not depend on time, i.e. k, and hence, the left hand side of the master equation has to vanish. One possibility to satisfy this constraint is to require each pair of summands of the state $\mathbf{x}'$ to be zero. This is just the detailed balance or micro-reversibility condition:

$$\rho(\mathbf{x}') P_{acc}(\mathbf{x}' \to \mathbf{x}) \alpha(\mathbf{x}' \to \mathbf{x}) = \rho(\mathbf{x}) P_{acc}(\mathbf{x} \to \mathbf{x}') \alpha(\mathbf{x} \to \mathbf{x}') \,. \tag{4.3}$$

Note that this condition is sufficient but not necessary, i.e. other choices of the probabilities might satisfy the equilibrium condition as well.
In the Metropolis algorithm, the probability to be at point $\mathbf{x}$ in configuration space, $\rho(\mathbf{x})$, is given by the Boltzmann weight. Detailed balance can be fulfilled by designing the attempt probability to be symmetric: $\alpha(\mathbf{x}' \to \mathbf{x}) = \alpha(\mathbf{x} \to \mathbf{x}')$ while the acceptance probability is taken to be

$$P_{acc}(\mathbf{x} \to \mathbf{x}') = \min(1, \rho(\mathbf{x}')/\rho(\mathbf{x})) \,. \tag{4.4}$$

But sometimes it may be more efficient to sample the configuration space with an asymmetric attempt probability $\alpha(\mathbf{x}' \to \mathbf{x}) \neq \alpha(\mathbf{x} \to \mathbf{x}')$, then detailed balance is satisfied with an acceptance probability given by [27]:

$$P_{acc}(\mathbf{x} \to \mathbf{x}') = \min\left(1, \frac{\alpha(\mathbf{x}' \to \mathbf{x})\rho(\mathbf{x}')}{\alpha(\mathbf{x} \to \mathbf{x}')\rho(\mathbf{x})}\right) . \tag{4.5}$$

In addition, it may be advantageous to conduct the generation of new states not in the coordinate system, where the energy of a configuration $H(\mathbf{x})$ is known, but in a generalized coordinate system $\tilde{\mathbf{x}}$. In this case, the acceptance criterion is:

$$P_{acc}(\mathbf{x} \to \mathbf{x}') = \min\left(1, \frac{\alpha(\tilde{\mathbf{x}}' \to \tilde{\mathbf{x}})\rho(\mathbf{x}')J(\tilde{\mathbf{x}}' \to \mathbf{x}')}{\alpha(\mathbf{x} \to \mathbf{x}')\rho(\mathbf{x})J(\tilde{\mathbf{x}} \to \mathbf{x})}\right) , \tag{4.6}$$

where $J(\tilde{\mathbf{x}} \to \mathbf{x})$ is the Jacobian of the coordinate transformation.
When designing moves which generate new configurations out of old ones, one of the three acceptance probabilities stated above has to be chosen according to the attempt probability to fulfill the detailed balance condition. Furthermore, moves have to be ergodic, which means that every possible position in configuration space should be accessible within a finite number of steps. Attention has to be paid to systems that are quasi-ergodic, this means that, although all position could be reached in principle, the system gets trapped in a local energy minimum being unable to move out of it within a finite number of steps. If this happens to be the case, new moves have to be designed to remove the quasi-ergodicness.

4.1.3 Correlations and error estimates

Performing a simulation we learn about the investigated physical system by taking averages of parameters that characterize it. Those data is only an estimate for the true values, since

only a finite number of samples is analyzed and since all data is subject to statistical errors. When applying Metropolis Monte Carlo, the correlation of successive samples has to be taken into account for the error estimate.

Starting from an arbitrary conformation the system has to equilibrate before taking samples. During this first phase of equilibration, the parameter of the system decreases to a constant plateau, where it is only subject to thermal fluctuations. Hence, plotting the order parameter versus the number of completed moves gives a guess about how many moves have to be performed until equilibrium is reached.
Assuming the system is equilibrated, samples A_i are taken yielding an estimate of the average of A, which gives the expectation value $\langle A \rangle$ in the limit of N to infinity:

$$\overline{A} = \frac{1}{N} \sum_{i=1}^{N} A_i \overset{N \to \infty}{\longrightarrow} \langle A \rangle \, . \tag{4.7}$$

Introducing a time interval δt in units of Monte Carlo steps between two successive observations A_i, A_{i+1}, the time at which sample i is taken is given by $t = i\delta t$. Using this notation, the characteristic decay time τ_A of the correlations is the integral over the correlation function $\phi(t)$:

$$\tau_A = \int_0^\infty dt \, \phi(t) = \int_0^\infty dt \, \frac{\overline{A(0)A(t)} - \overline{A}^2}{\overline{A^2} - \overline{A}^2} \, . \tag{4.8}$$

Taking the correlations into account, the square of the statistical error is given by [30, 18]:

$$\overline{(\delta A)^2} = \frac{1}{N} \left[\overline{A^2} - \overline{A}^2 \right] \left(1 + 2 \frac{\tau_A}{\delta t} \right) \, . \tag{4.9}$$

In comparison to the statistical error of uncorrelated data Metropolis Monte Carlo has an additional factor of $(1+2\tau_A/\delta t)$ to take into account. Clearly, an estimate of the characteristic decay time τ_A can be obtained by measuring $\overline{(\delta A)^2}$, $\overline{A^2}$ and $\overline{A}$.
Another approach to obtain the characteristic decay time of the correlations is direct measurement of a correlation function $\phi(t)$ over time. The correlation function in general decays as an exponential function with characteristic time τ_A:

$$\phi(t) = e^{-t/\tau_A}. \tag{4.10}$$

If the characteristic decay time $\tau_A \gg \delta t$, Eq. (4.9) can be simplified, yielding:

$$\overline{(\delta A)^2} = \left[\overline{A^2} - \overline{A}^2 \right] \left(2 \frac{\tau_A}{t} \right) , \tag{4.11}$$

where $N\delta t = t$. Hence, the statistical error is inversely proportional to the number of uncorrelated samples, τ_A/t. If on the other hand the time interval between subsequent samples is taken large enough to gain uncorrelated measurements, the statistical error results in

$$\overline{(\delta A)^2} = \frac{[\overline{A^2} - \overline{A}^2]}{N} \, . \tag{4.12}$$

In addition, simulations should be tested against quasi-ergodicity by repeating a given run with different initial conformations and different sequences of random numbers.

4.2 Simulation of a semiflexible ring

To implement a Metropolis Monte Carlo simulation, there are two questions to answer: What is the Hamiltonian of the system? And how can new configuration be generated?
To model a semiflexible polymer ring, the contour length of a polymer has to be discretized. Imagining a polymer ring of infinite stiffness, the ground state conformation of a discretized polymer would be a regular polygon of N segments, where N denotes the order of discretization. To model a polymer, the inextensibility constraint given in Eq. (2.17) should be satisfied, hence, all segment should remain their length. Therefore, the simulation is pursued in free space.
The first ingredient to know for a Monte Carlo simulation is the Hamiltonian of the system. For a discretized polymer the Hamiltonian is equivalent to the discretized free energy of the wormlike chain model, see Eq (2.12):

$$\frac{H}{k_B T} = N \frac{l_p}{L} \sum_{i=1}^{N} \left(1 - \mathbf{t}_t^i \mathbf{t}_t^{i+1}\right), \tag{4.13}$$

where N denotes the number of segments and the parameter L/l_p characterizes the stiffness of the polymer. For L/l_p small the polymer is in the stiff regime and becomes more and more flexible for increasing L/l_p.

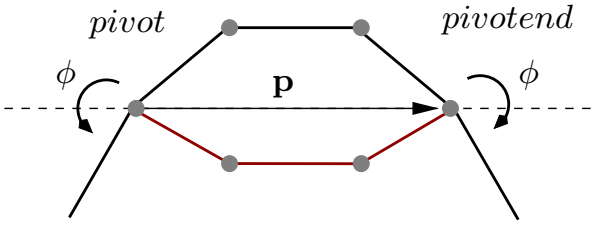

Figure 4.1: In the crankshaft move two vertices of the polygon, *pivot* and *pivotend*, are drawn randomly and the segments enclosed by them are rotated by an random angle $\phi \in [-\phi_{max}, \phi_{max}]$.

The remaining question is how to produce new configurations of a polymer ring keeping the segment length fixed. We choose to generate new conformations of the polymer with symmetric attempt probabilities by employing the crankshaft move [26]. For this move two vertices, *pivot* and *pivotend*, of the polygon are drawn randomly and the adjacent sub-chain between *pivot* and *pivotend* is rotated around the pivot $\mathbf{p}$, interconnecting the random vertices, by a random angle ϕ, see Fig. 4.1. The random angle is uniformly distributed over the interval $\phi \in [-\phi_{max}, \phi_{max}]$, where the maximum angle ϕ_{max} is adjusted such that the acceptance probability of the move lies between 25% and 50%. The new positions of the polygon vertices are obtained by subtracting the position vector of the pivot's origin $\mathbf{r}_{pivot}$ from all vertex vectors to be changed and rotating the difference vector by laws of finite rotation [23]. After rotating the difference vector, the pivot's origin which is identical to the position of the first random vertex is added again yielding the new position of the vertex:

$$\begin{aligned} \mathbf{r}_i' &= \mathbf{r}_{pivot} + (\mathbf{p} \cdot (\mathbf{r}_i - \mathbf{r}_{pivot})) \cdot \mathbf{p} + [(\mathbf{r}_i - \mathbf{r}_{pivot}) - (\mathbf{p} \cdot (\mathbf{r}_i - \mathbf{r}_{pivot})) \cdot \mathbf{p}] \cos\phi \\ &+ ((\mathbf{r}_i - \mathbf{r}_{pivot}) \times \mathbf{p}) \sin\phi \,. \end{aligned} \tag{4.14}$$

Changing the position of vertices the direction of the enclosed tangents also alters. The new tangents are calculated by $\mathbf{t}_t^i = (\mathbf{r}_{i+1} - \mathbf{r}_i)/|\mathbf{r}_{i+1} - \mathbf{r}_i|$. After each move, the energy difference

due to the change of the enclosed tangents is calculated and the move is rejected and accepted according to the Metropolis Monte Carlo acceptance probability given in Eq. (4.4).
The number of steps for equilibration are found to be roughly $600N$, taken to scale linearly with N. The quantity of steps, that have to be performed to obtain uncorrelated samples were analogously estimated to be $300N$.

Knowing all ingredients, the simulation of a semiflexible polymer ring is implemented with the following algorithm:

- initialize the polymer ring as a regular polygon of N segments with circumradius $R_c = 1$,
- adjust the maximum angle by increasing or decreasing ϕ_{max} in steps of 0.01 if the acceptance rate of the moves is a above 50% or below 25%, respectively,
- perform crankshaft moves until the system is equilibrated after about $600N$ moves,
- take uncorrelated samples every $300N$ steps and calculate averages of characteristic parameters.

5 The semiflexible ring

Consider a semiflexible polymer, well described by the wormlike chain model. If the ends of this polymer are interconnected without twisting it, one obtains a semiflexible ring. The semiflexible ring is a limiting case of a fluctuating ribbon, where the cross-section is symmetric, i.e. both bending stiffnesses are equal, and no twist stiffness is imposed. Analytic calculations for the semiflexible ring are presented in section 3.4.2.
In this chapter, the properties of a fluctuating semiflexible ring are discussed in detail. At first, the Monte Carlo data for the mean square diameter is compared to the analytic prediction of the model presented in chapter 3, yielding very good agreement up to high ratios of perimeter to persistence length. Proceeding, the cross-over behavior of the radius distribution function from semiflexible to flexible polymers is investigated and found to be dominated by a finite size effect. The chapter concludes with a broad examination of the shape of semiflexible rings.

5.1 Mean square diameter

The fluctuations of a semiflexible ring are best described by the mean square diameter $\langle D^2 \rangle$ analogous to the characterization of a free polymer by the mean square end-to-end distance. Therefore, $\langle D^2 \rangle$ should also be a parameter relevant for experimental investigations. In section 3.4.2, predictions for the decrease of the mean square diameter with increasing flexibility were made, which shall now serve to gain an understanding of the quality of the approximations made when describing tight rings. Furthermore, the Monte Carlo data permits an insight into the cross-over from semiflexible to flexible rings.

Numerical calculations of Shimada and Yamakawa led to a first order approximation of the mean square radius of gyration of a nearly rigid ring [48] as introduced in section 2.2.1:

$$\langle R_g^2 \rangle = R_c^2 \left(1 - 0.057 \frac{2\pi R_c}{l_p} \right). \tag{5.1}$$

For a tight ring, the center of mass is almost equal to the center of the ring, hence, radius and radius of gyration should decrease in the same way. The analytical calculations presented in chapter 3 led to the following formula for the mean square diameter:

$$\langle D^2 \rangle = (2R_c)^2 \left(1 - \frac{1}{16} \frac{2\pi R_c}{l_p} \right). \tag{5.2}$$

Hence, the analytic approximation of a tight ring yields an exact result of the first correction from a rigid ring.
In order to asses the quality of the tight ring approximation, Monte Carlo simulations were performed for different values of L/l_p. Using an algorithm as presented in section 4.2 with

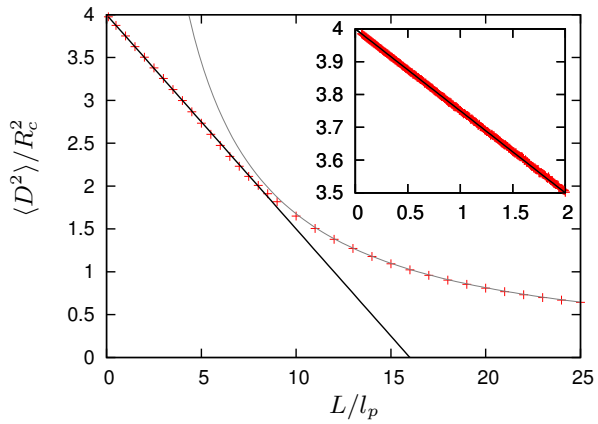

Figure 5.1: Comparison of the simulation data (crosses) for the mean square diameter $\langle D^2\rangle/R_c^2$ versus L/l_p to Eq. (5.2) (black line). For $L/l_p \gg 1$ the mean square diameter decays in a power law given by Eq. (5.4) (grey line). Error bars for the Monte Carlo data are approximately of the size of the symbols.

$N = 50$ segments discretizing a polymer ring, the data depicted in Fig. 5.1 was collected. For L/l_p equal zero the diameter of a rigid ring $(2R_c)^2$ is expected, while the diameter should decrease for increasing flexibility $L/l_p > 0$ due to the thermal fluctuations. Comparing the Monte Carlo data to the analytic result of Eq. (5.2), one recognizes that the data fits the theory excellently and diverges slightly for L/l_p larger than one and a half, but is a good approximation for degrees of flexibility up to $L/l_p = 8$. Note that there is no free parameter to adjust the Monte Carlo simulation data to the analytic predictions. Hence, the analytic calculations derived in chapter 3 describe the fluctuations of a semiflexible ring very well up to large ratios of perimeter to persistence length.
For increasing flexibility, the mean square diameter decreases less and less fast. The mean of the diameter $\langle D\rangle$ certainly decays to zero for a freely jointed ring polymer. But the variance of the diameter and so the second moment remains finite to allow for various coiled up conformations. For very flexible semiflexible rings the mean square diameter declines to its limiting value of $Ll_p/2$ as, according to Yamakawa [57]:

$$\langle D^2\rangle_{L/l_p\gg 1} = \frac{Ll_p}{2}\left(1 - \frac{1}{6}\frac{l_p}{L}\right). \tag{5.3}$$

The Monte Carlo data suggest the following power law decay:

$$\langle D^2\rangle \propto \left(\frac{l_p}{L}\right)^{1.040\pm 0.002}. \tag{5.4}$$

in accordance with the result by Yamakawa.

The knowledge of the dependence of the mean square diameter on the persistence length is also of interest for experiments. If the microscopes are sufficient to focus a fluctuating polymer ring in total or at least at two opposing segments of the ring, the diameter can be observed over time and averaged. Using the analytic relationship in Eq. (5.2) between diameter and persistence length, the stiffness of a polymer can be detected. However, since the fluctuations of an unconstraint polymer ring are three dimensional, confocal microscopy

would be required to observe the diameter as presented above. Using normal fluorescence microscopy, the error in the measurement of the persistence length depends on the height of the undetected out-of-plane fluctuations. A way out would be to compare the measured diameter to the projection of $\langle D^2 \rangle$, which can in principle be obtained from Monte Carlo simulations. However, the technique invented by Sackmann and collaborators [33, 9] to study actin rings constrains the rings to fluctuations in a two-dimensional plane. Hence, the mean square diameter becomes observable by normal fluorescence microscopy and the error-prone out-of-plane fluctuations are avoided. The mean square diameter of a truly two dimensional semiflexible ring is extracted from the calculations in chapter 3 by neglecting the contributions due to the modes of the theta angle, yielding:

$$\langle D^2 \rangle_{2D} = (2R_c)^2 \left(1 - \frac{1}{2\pi^2} \frac{2\pi R_c}{l_p} \right). \tag{5.5}$$

Note that the decay is slower, indicating that a two dimensional ring is stiffer than a three dimensional, as expected.

In the following section, a further parameter is introduced providing a tool to measure the persistence length of semiflexible rings as well: the mean radius of the semiflexible ring $\langle R \rangle$.

5.2 Radius distribution

A central quantity for characterizing the conformation of single polymer chains is the distribution $G(\mathbf{R})$ of the end-to-end distance $\mathbf{R}$. For a freely jointed chain, $G(\mathbf{R})$ is known exactly and can for most purposes be approximated by a Gaussian distribution [56]. For semiflexible polymers, the end-to-end distance distribution has been calculated in the limits of almost flexible polymers [12, 21] and nearly rigid polymers [54]. $G(\mathbf{R})$ is highly peaked close to full extension for very stiff polymers and flattens out to form a Gaussian distribution around small $|\mathbf{R}|$ in the flexible regime.
Considering rings, the quantity corresponding to the distribution of the end-to-end vector is the distribution of the diameter or equivalently the distribution of the radius of the ring $G(R)$. In the following, Monte Carlo simulation data for the radius distribution is analyzed using the moments of the distribution. An interesting cross-over between semiflexible and flexible rings is observed. Furthermore, the mean radius $\langle R \rangle$ is found to decay linearly with L/l_p over a wide range of flexibility, recommending the mean radius as the parameter to measure the stiffness of rings in experiments.

The radius distribution of a ring can be determined from Monte Carlo simulations by measuring for many configurations the distance of each segment of the discretized ring to the center of mass, respectively. In analogy to the end-to-end distance distribution of a semiflexible polymer chain, the radius distribution is expected to be highly peaked around the contour radius R_c for stiff rings, i.e. $L/l_p < 2$, and broadening into a Gaussian distribution centered around $R < R_c$ for flexible rings, $L/l_p \gg 2$.

Radius distribution histograms obtained from Monte Carlo simulations are presented in Fig. 5.2 for different levels of flexibility. In the stiff limit, $L/l_p = 1$, $G(R)$ is nearly Gaussian distributed around a mean slightly smaller than $R/R_c = 1$ as in Fig. 5.2(a). This behavior is in contrast to the highly antisymmetric distribution of a free semiflexible polymer. In

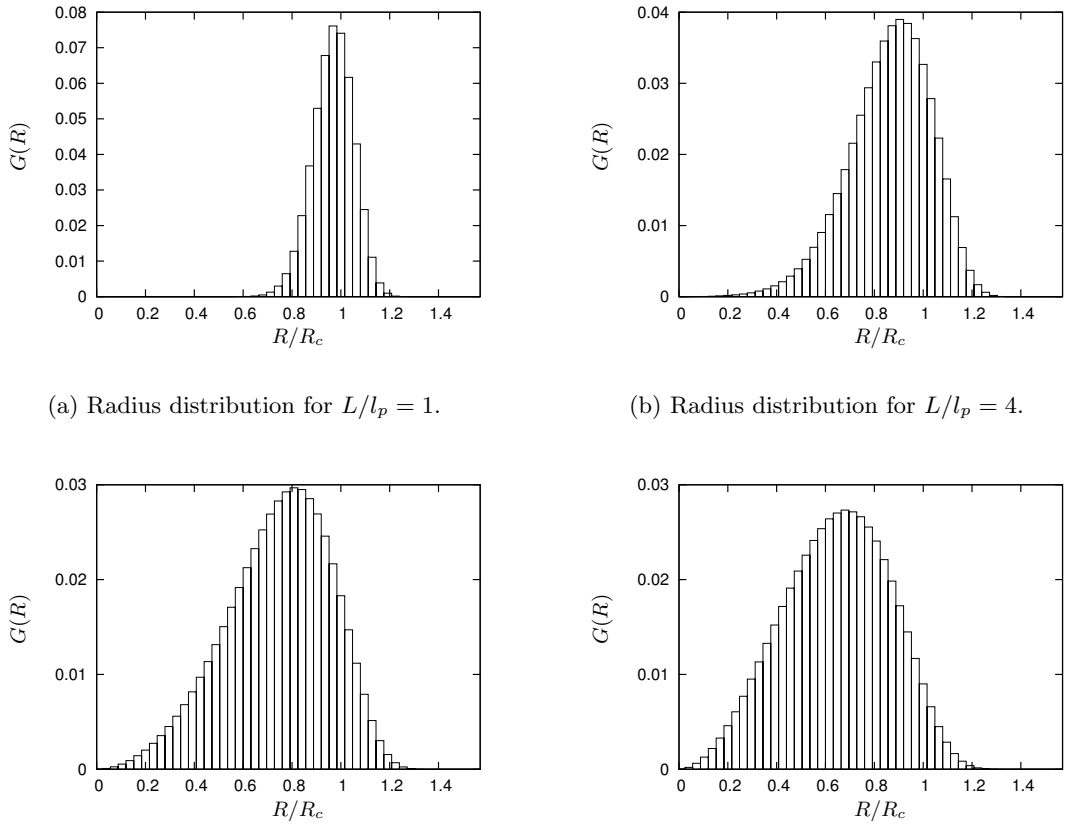

(a) Radius distribution for $L/l_p = 1$.

(b) Radius distribution for $L/l_p = 4$.

(c) Radius distribution for $L/l_p = 7$.

(d) Radius distribution for $L/l_p = 10$.

Figure 5.2: Radius distribution histograms at different levels of flexibility. For very stiff rings the distribution is almost Gaussian, broadening into a left-skewed distribution, when the flexibility is increased. Finally, the distribution becomes Gaussian again in the limit of $L/l_p \to \infty$ due to the central limit theorem.

the limit of tight polymer rings, the persistence length is so high, that a barely fluctuating segment of the ring is almost not influenced by the fluctuations of other segments and therefore yields a Gaussian radius distribution. Proceeding to more flexible rings the distribution spreads out, centered around smaller and smaller values of R, and becomes asymmetric, in this case denoted left-skewed, which means that the lower tail is longer than the higher, see Fig. 5.2(b)&(c). For even higher flexibility the radius distribution is again Gaussian-like, centered at $0 < R < R_c$, as expected from the central limit theorem, see Fig. 5.2(d).

The change in the shape of the distribution can be measured by its skewness. The skewness g_1 is the third standardized moment in probability theory and is defined as the ratio of the third moment about the mean to the third power of the standard deviation. For a sample of N measurements the skewness is calculated by:

$$g_1 = \frac{\sqrt{N}\sum_{i=1}^{N}(x_i - \bar{x})}{\left(\sum_{i=1}^{N}(x_i - \bar{x})^2\right)^{3/2}} \,. \tag{5.6}$$

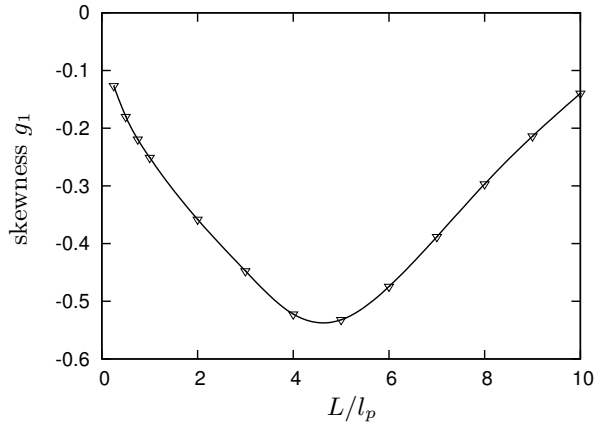

Figure 5.3: Monte Carlo data of the skewness g_1 of the radius distribution versus ratio of length to persistence length. The magnitude of the skewness increases due to the finite size of the radius and decreases again due to the central limit theorem. The error in the simulation data is of the order of the size of the symbols.

A Gaussian distribution has zero skewness while left-skewed distributions, as observed for the semiflexible ring, have negative skewness. Positive values of g_1 correspond to right-skewed distributions. Plotting the skewness of $G(R)$ versus L/l_p, as done in Fig. 5.3, reveals the change in the shape of the distribution from "Gaussian" for a rigid ring ($L/l_p = 0$) to highly skewed distributions for $L/l_p \approx 5$ back to Gaussian in the limit of L/l_p to infinity.
This change of aspect is the result of a finite size effect. If a ring of perimeter $2\pi R_c$ is folded to a line, the maximal radius possible is $\pi R_c/2$. Hence, no radius of the ring can be larger than $\pi R_c/2$ without violating the inextensibility constraint. Therefore, $R/R_c = \pi/2$ has been chosen the maximum value of the abscissa in the histograms in Fig. 5.2. If a fluctuating semiflexible ring becomes more and more flexible, the radii exhibited are spread about a larger and larger interval. But for the ring a maximum radius exists, hence, the distribution spreads asymmetrically to smaller radii and features a left-skewed distribution. If the ring becomes even more flexible, the segments are less and less correlated and the geometry of the ring turns unimportant, yielding a Gaussian radius distribution as for a flexible chain. This limiting behavior follows from the central limit theorem.
The minimum of the skewness indicates a cross-over from semiflexible to flexible behavior of the ring. Other cross-overs between the two levels of flexibility of a polymer have been observed for L/l_p of the order of one [53]. For the ring, the cross-over occurs comparatively late, due to the additional stiffness induced by the geometry of the ring.

Based on the radius distribution, a contribution can be made to the discussion on a possible interaction of the membrane with the actin ring in giant vesicles experiments performed by Sackmann and collaborators as well as Bausch and collaborators [33, 9]. The radii exhibited are always smaller than $R/R_c = 1.3$, as can be read off the histograms in Fig. 5.2. Therefore, one can state that a membrane of radius 1.3 times larger than the radius of the actin ring will not effect the fluctuations of the ring due to sterical hindrance. If the radius of the membrane is smaller, a ring confined to a sphere is studied, requiring different interpretation.

Having analyzed the third moment of the radius distribution in form of the skewness, the first moment $\langle R \rangle$ is investigated. Simple scaling arguments in section 2.2.1 led to the prediction

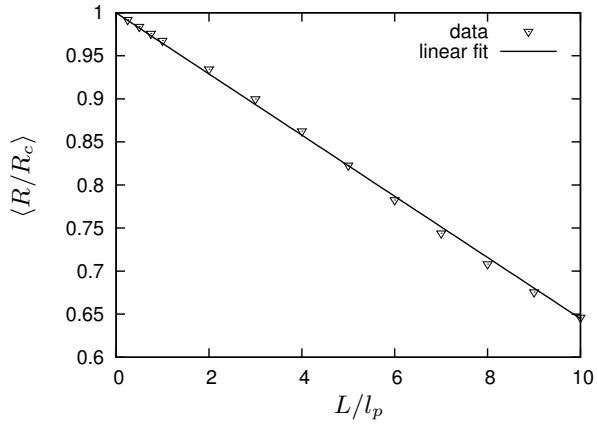

Figure 5.4: Monte Carlo data (triangles) for the mean radius. The latter decreases linearly for increasing flexibility over a wide range of flexibility and may therefore serve as a parameter to determine the stiffness of a ring in experiments. The linear fit obeys Eq. (5.8).

of a linear decay of the mean radius of a tight ring with the ratio of perimeter to persistence length:

$$\langle R \rangle = R_c \left(1 - \frac{4\pi^2}{720}\frac{L}{l_p}\right) \approx R_c \left(1 - 0.055\frac{L}{l_p}\right). \tag{5.7}$$

This scaling argument is expected to hold in the limit of tight rings, i.e. $L/l_p < 2$. Performing Monte Carlo simulations, indications arise that the linear dependence of the mean radius on L/l_p holds up to values of $L/l_p = 10$, well in the flexible regime. The Monte Carlo data is presented in Fig. 5.4. The mean radius decays linearly with

$$\langle R \rangle = R_c \left(1 - (0.0355 \pm 3 \cdot 10^{-4})\frac{L}{l_p}\right). \tag{5.8}$$

Since the mean radius decays linearly over such a large range of flexibility, the mean radius of a semiflexible ring could be the parameter of choice to determine the persistence length of a polymer ring in experiments.

5.3 Shape of the semiflexible ring

The shape of polymers have been under discussion since it was found that the average shape of a single trajectory of a random walk, i.e. a freely jointed chain, is asymmetric. To obtain a spherically symmetric random walk, the number of steps in each of the six space directions has to be equal. But the number of those symmetric conformations is smaller than the number of asymmetric trajectories. Hence, the average random walk is asymmetric. Being able to classify the asymmetry of polymers, different polymers become comparable. While flexible polymers with and without self-avoidance have been analyzed both analytically and by simulations, no investigations into the shape of semiflexible polymers, not to mention semiflexible polymer rings, have been undertaken.
Considering the shape of semiflexible rings, its change on increasing the flexibility of the rings shall be investigated. As a preliminary, parameters that characterize a polymer's shape are

introduced, followed by a scaling argument, which explains the change in shape of tight rings. Finally, the alteration of shape for semiflexible rings for increasing levels of flexibility are presented and interpreted.

5.3.1 Characterizing the shape of a polymer

What is the shape of a single polymer and how can it be characterized? Clearly, averaging an isotropic ensemble of trajectories yields a spherically symmetric distribution. But this does not imply that the typical trajectory of a polymer is itself symmetric. In fact, random walks for example have been found to be on average rather prolate (cigar-like) than spherically symmetric. For clarification of the terms prolate and oblate see Fig. 5.5 and Fig. 5.6, respectively.

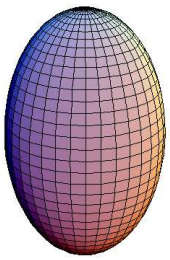

Figure 5.5: Drawing of a prolate spheroid, the eigenvalues λ_i, $i = 1, 2, 3$ of the radius of gyration tensor are ordered as $(\lambda_1 \gg \lambda_2 \approx \lambda_3)$.

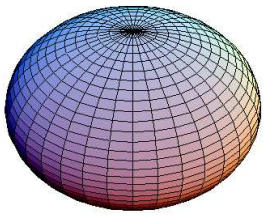

Figure 5.6: Drawing of an oblate spheroid, where the eigenvalues of the radius of gyration tensor obey the ordering $(\lambda_1 \approx \lambda_2 \gg \lambda_3)$.

The characterization of a polymer's shape is based on the definition of its size. The latter can be either defined by its end-to-end distance or by its radius of gyration. The radius of gyration is given by the average distance of each segment $\mathbf{r}(s)$ of the polymer from the center of mass $\mathbf{r}_{com}$. Therefore, every segment of the polymer is equally weighted and the spatial extend of the polymer is also reflected by the radius of gyration. Using the center of mass $\mathbf{r}_{com}$ of a polymer defined by:

$$\mathbf{r}_{com} = \frac{1}{L}\int_0^L ds\, \mathbf{r}(s)\,, \tag{5.9}$$

the mean square radius of gyration R_g^2 is computed:

$$\langle R_g^2 \rangle = \frac{1}{L}\int_0^L ds\, \langle (\mathbf{r}(s) - \mathbf{r}_{com})^2 \rangle = \left\langle \frac{1}{L}\int_0^L ds\, r^2(s) - \frac{1}{L^2}\left(\int_0^L ds \mathbf{r}(s)\right)^2 \right\rangle . \tag{5.10}$$

To measure the spatial extend of a polymer in three dimensions the radius of gyration is generalized to a shape tensor Q, whose components are [49]:

$$Q_{ij} = \frac{1}{L}\int_0^L r_i(s) r_j(s)\, ds - \frac{1}{L^2}\int_0^L r_i(s)\, ds \int_0^L r_j(s)\, ds\,. \tag{5.11}$$

Note that the trace of this tensor retrieves the radius of gyration. The shape of the polymer itself is hidden in the proportion of the eigenvalues $\lambda_1 \geq \lambda_2 \geq \lambda_3$ of the radius of gyration

tensor Q. Early investigations of the shape of polymers classified the asymmetry by the ratio of the eigenvalues $\lambda_1 : \lambda_2 : \lambda_3$ [50, 49, 37, 45, 44, 28]. The random walk was found to be characterized by prolateness, which is increased when imposing self-avoidance.
Since Q has to be diagonalized for each configuration to yield the eigenvectors λ_i, $i = 1, 2, 3$, the ratio of the eigenvalues is not suitable for analytic calculations. Progress was made when Aronovitz and Nelson [2] as well as Rudnick and Gaspari [46] realized that the asymmetry of a polymer can be described by the deviation of the eigenvalues from their mean eigenvalue $\bar{\lambda} = \mathrm{Tr}\, Q/3$. Clearly the eigenvectors of a shifted tensor $\widehat{Q}$ defined by :

$$\widehat{Q}_{ij} = Q_{ij} - \frac{1}{3}\delta_{ij}\mathrm{Tr}\, Q\,, \tag{5.12}$$

incorporate just this deviation and therefore the asymmetry of a configuration. Taking the trace of the square of the shifted tensor:

$$\mathrm{Tr}\, \widehat{Q}^2 = \sum_{i=1}^{3} \left(\lambda_i - \bar{\lambda}\right)^2, \tag{5.13}$$

yields a rotationally invariant polynomial. Describing the asymmetry of a polymer by this polynomial, the tensor Q does not have to be diagonalized and the shape of a polymer becomes analytically tractable. While $\mathrm{Tr}\, \widehat{Q}^2$ is the variance of the eigenvectors determining the deviation from spherical symmetry, the nature of this asphericity is measured by the determinant of $\widehat{Q}$:

$$\mathrm{Det}\, \widehat{Q} = \left(\lambda_1 - \bar{\lambda}\right)\left(\lambda_2 - \bar{\lambda}\right)\left(\lambda_3 - \bar{\lambda}\right). \tag{5.14}$$

For a prolate polymer ($\lambda_1 \gg \lambda_2 \approx \lambda_3$), the first term remains positive while the other two terms in the product become negative resulting in a overall positive determinant. On the other hand, for an oblate polymer ($\lambda_1 \approx \lambda_2 \gg \lambda_3$) only the last term turns negative, yielding an overall negative $\mathrm{Det}\, \widehat{Q}$. Hence, the sign of $\mathrm{Det}\, \widehat{Q}$ denotes oblateness or prolateness, while its magnitude indicates the degree of prolateness or oblateness. To compare values of the asymmetry $\mathrm{Tr}\, \widehat{Q}^2$ and the nature of asymmetry $\mathrm{Deet}\, \widehat{Q}$ independent of the length of the polymer, both are normalized. Then, the asphericity of the shape of a polymer is defined by [2]:

$$\Delta = \frac{3}{2}\frac{\mathrm{Tr}\, \widehat{Q}^2}{(\mathrm{Tr}\, Q)^2}\,, \tag{5.15}$$

and the nature of asphericity by [8]:

$$\Sigma = \frac{4\mathrm{Det}\, \widehat{Q}}{\left(\frac{2}{3}\mathrm{Tr}\, \widehat{Q}^2\right)^{3/2}}\,. \tag{5.16}$$

The asphericity takes values between $0 \geq \Delta \geq 1$, where $\Delta = 0$ corresponds to a spherically symmetric object, where all eigenvectors of the radius of gyration tensor are equal. For $\Delta = 1$, the polymer is fully extended, forming a rigid rod. The nature of asphericity is bounded between $-1 \geq \Sigma \geq 1$. $\Sigma = -1$ is obtained for a fully oblate object such as a disc, while $\Sigma = 1$ is the result for a rigid rod. Note that the nature of asphericity parameter Σ presented in here is different from the parameter introduced by Aronovitz and Nelson [2], since their parameter has proven to be size-dependent and has been replaced by the size-independent parameter Σ [8].

Monte Carlo and Brownian dynamics simulations have been applied to measure the asphericity and nature of asphericity for freely jointed chains [8], freely jointed chains with self avoidance [4, 8], freely jointed chains in porous media [25] and star macromolecules [5]. The analytic calculations differ in the way the ensemble average of the quotients in Eqs. (5.15), (5.16) is taken. Aronovitz and Nelson [2] as well as Rudnick and Gaspari [46] approached the simpler task of evaluating the quotient of the averages instead of calculating the averages of quotients, when calculating the asphericity of self-avoiding and non-self-avoiding freely jointed chains, respectively. This way of evaluating the average yields a measurement of the asphericity which is size-dependent. To obtain a pure measurement of the shape independent of the overall size of the object the averages of quotients have to be considered. Performing the averages of quotients the mean asphericity of freely jointed chains in d dimensions has been derived analytically by Rudnick, Beldjenna and Gaspari [46] and Diehl and Eisenriegler [13]. In three dimensions the mean asphericity of a freely jointed chain is 0.394. Interestingly Diehl and Eisenriegler also investigated Δ for a freely jointed polymer ring (fjr). Their analytical result of

$$\Delta_{\mathrm{fjr}} = 0.2464... \tag{5.17}$$

indicates that the closure of a flexible polymer induces a remarkable change in shape yielding a more spherically symmetric aspect than for a free polymer.

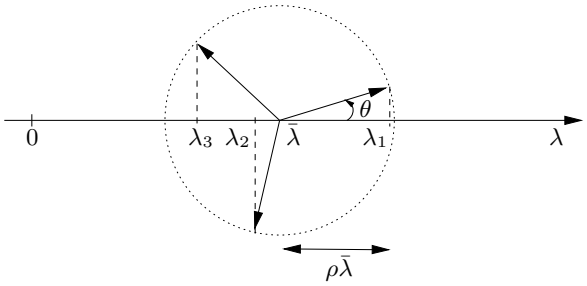

Figure 5.7: Geometric representation of the eigenvalues of the radius of gyration tensor Q. The three eigenvalues can be transformed into one size-dependent parameter $\bar{\lambda}$ and two size independent parameters ρ and θ by Eqs. (5.19). ρ characterizes the asphericity of a polymer; θ indicates the nature of asphericity. $0 \leq \theta \leq \pi/6$ corresponds to prolate shape, $\pi/6 \leq \theta \leq \pi/3$ to oblate shape.

To obtain a more detailed characterization of a polymer's shape, it is instructive to consider a distribution function P as introduced by Cannon, Aronovitz and Goldbart [8]. P is the distribution function of the shifted and rescaled radius of gyration tensor $(\mathrm{Tr}\, Q)^{-1}\widehat{Q}$. Since $\widehat{Q}$ is traceless, the three eigenvectors of the shifted tensor can be represented by two parameters denoted θ and ρ. Consider a one-dimensional axis where all eigenvalues λ_i, $i = 1, 2, 3$, of the radius of gyration tensor Q and their mean value $\bar{\lambda}$ are indicated, as in Fig. 5.7. Then a circle of radius $\rho\bar{\lambda}$ is drawn centered at $\bar{\lambda}$, such that the three eigenvalues can be interpreted as the projections of three two-dimensional vectors starting at $\bar{\lambda}$ and terminating on the circle with relative angles $2\pi/3$.

$$\begin{aligned} \lambda_1 &= \bar{\lambda}\,(1 + \rho\cos(\theta))\,, \\ \lambda_2 &= \bar{\lambda}\,(1 + \rho\cos(\theta + 2\pi/3))\,, \\ \lambda_3 &= \bar{\lambda}\,(1 + \rho\cos(\theta - 2\pi/3))\,. \end{aligned} \tag{5.18}$$

In this definition ρ indicates the degree of asphericity, since $\rho = 0$ is obtained for equal

eigenvalues, $\lambda_1 = \lambda_2 = \lambda_3$, and increases when the eigenvalues spread out. θ, on the other hand, denotes the nature of asphericity. For a prolate polymer ($\lambda_1 \gg \lambda_2 \approx \lambda_3$) θ is close to zero; for an oblate polymer ($\lambda_1 \approx \lambda_2 \gg \lambda_3$) θ is greater or equal $\pi/3$. The cross-over between prolateness and oblateness occurs when $\lambda_3 = 2\lambda_2 - \lambda_1$, then $\lambda_2 = \bar{\lambda}$ yields a zero determinant $\mathrm{Det}\,\widehat{Q}$. This cross-over corresponds to $\theta = \pi/6$. The parameters ρ and θ can themselves be used to compute the asphericity and nature of asphericity:

$$\Delta = \rho^2/4\,, \tag{5.19}$$

$$\Sigma = 4\cos(\theta)\sin(\pi/6-\theta)\sin(\pi/6+\theta)\,. \tag{5.20}$$

The formalism presented in this section is now employed to analyze the shapes of semiflexible rings. But before Monte Carlo simulations are analyzed a scaling argument for tight rings is introduced.

5.3.2 A scaling argument

To explain the change of aspect of a tight ring when increasing the ratio of length to persistence length, a calculation of the asphericity and nature of asphericity for a simple model is presented in this section.

To give a scaling argument for the asphericity and the nature of the asphericity, the mean shape of a stiff ring is approximated to be an ellipse. For an infinite bending stiffness, the ellipse coincides with a rigid ring and for stiff rings the semiaxes of the ellipse decrease and increase from equality depending on the ratio of the perimeter to the stiffness of the ring L/l_p. In fact, both first non-zero modes of the Euler angles $\delta\tilde{\phi}(2)$ and $\delta\tilde{\theta}(1)$ have oval shapes, see Fig. 3.1. The modes of the Euler angle ψ are not considered, since the semiflexible ring has no twist stiffness and is therefore absolute free to twist.
The modes of the ring rotate in space, and if one would draw all trajectories of a fluctuating ring on top of each other, the thickest line would be that of a rigid ring, but if one measures the shape of every single trajectory and averages those, the mean shape will be an ellipse, since the dominant first mode is oval.

But how do the semimajor axis $a(L/l_p)$ and the semiminor axis $b(L/l_p)$ increase and decrease with the flexibility of the polymer ring? In section 2.2.1 a scaling argument for the fuzzy diameter of a tight ring was equated by calculating the fluctuations of a weakly bend rod with periodic boundary conditions, yielding:

$$\tilde{D} \propto 2\sqrt{\langle r^2_{\perp,1}\rangle} = 2\cdot\frac{2\pi}{\sqrt{720}}\frac{R_c^{3/2}}{l_p^{1/2}}\,. \tag{5.21}$$

Fitting an ellipse into this fuzzy diameter requires the semiminor axis to be decreased from the radius of a rigid ring R_c by the square root of the undulations $\langle r^2_{\perp,1}\rangle$, while the semimajor axis is extended by the same amount. Hence, the equation of the ellipse becomes:

$$\mathbf{r}(s) = \begin{pmatrix} a(L/l_p)\cos(s/R_c) \\ b(L/l_p)\sin(s/R_c) \\ 0 \end{pmatrix} = \begin{pmatrix} R_c\left(1+\sqrt{c\frac{L}{l_p}}\right)\cos(s/R_c) \\ R_c\left(1-\sqrt{c\frac{L}{l_p}}\right)\sin(s/R_c) \\ 0 \end{pmatrix}, \tag{5.22}$$

where for the prefactor a shorthand is used, $\sqrt{c} = 2\pi/\sqrt{720}$. Note that deviations from an elliptical shape in the third component of $\mathbf{r}(s)$ are not considered, as they are of second order for the shape of polymer ring. This does not imply that fluctuations out of the xy-plane are neglected, since their first mode also creates an elliptical shape and is therefore incorporated in the shape, see Fig. 3.2(a). The shape of an ellipse is usually expressed in a term called eccentricity e, defined by:

$$e = \sqrt{1 - \frac{b^2}{a^2}} \,. \tag{5.23}$$

Hence, the eccentricity is zero for a circle and unity for a rod. Similar to the asphericity of three dimensional objects, the eccentricity describes two dimensional shapes. For the ellipse defined above the eccentricity is increasing with growing flexibility.
To determine the asphericity and the nature of asphericity as defined in Eqs. (5.15) and (5.16), respectively, the radius of gyration tensor and the shifted radius of gyration tensor as introduced in Eqs. (5.11) and (5.12) are derived for an ellipse as stated above.
Integrating any coordinate $r_i(s)$ of the ring over the whole length gives zero due to the periodic boundary conditions. Hence, only the correlation integrals have to be solved to compute the radius of gyration tensor. Those can be further simplified by taking the principal axes of the ellipse to be aligned to the space coordinates. This way no correlations occur, and the radius of gyration tensor consists of integrals over the squared coordinates $r_i(s)$ on the diagonal and is zero otherwise:

$$Q_{\text{ellipse}} = \begin{pmatrix} \frac{R_c^2}{2}\left(1+\sqrt{c\frac{L}{l_p}}\right)^2 & 0 & 0 \\ 0 & \frac{R_c^2}{2}\left(1-\sqrt{c\frac{L}{l_p}}\right)^2 & 0 \\ 0 & 0 & 0 \end{pmatrix} . \tag{5.24}$$

Equating the mean eigenvalue of the radius of gyration tensor, the shifted radius of gyration tensor is calculated by subtracting the mean eigenvalue from the diagonal entries of Q, yielding:

$$\widehat{Q}_{\text{ellipse}} = \begin{pmatrix} R_c^2\left[\frac{1}{6}\left(1+c\frac{L}{l_p}\right)+\sqrt{c\frac{L}{l_p}}\right] & 0 & 0 \\ 0 & R_c^2\left[\frac{1}{6}\left(1+c\frac{L}{l_p}\right)-\sqrt{c\frac{L}{l_p}}\right] & 0 \\ 0 & 0 & -\frac{R_c^2}{3}\left(1+c\frac{L}{l_p}\right) \end{pmatrix} . \tag{5.25}$$

With those results the asphericity of an ellipse, whose eccentricity is increasing with the flexibility of the polymer, is determined by:

$$\Delta_{\text{ellipse}} = \frac{1}{4} + \frac{3c\frac{L}{l_p}}{\left(1+c\frac{L}{l_p}\right)^2} = \frac{1}{4} + \frac{\pi^2}{60}\frac{L}{l_p} + \mathcal{O}((L/l_p)^2) \,. \tag{5.26}$$

A plot of this result is presented in Fig. 5.8(a). From the ground state value of 0.25 for a rigid ring the asphericity of stiff rings increases linearly with the ratio of perimeter to persistence length. For $L/l_p = 1/c$, the semiminor axis is zero, while the semimajor axis is twice the radius of the rigid ring. Hence, the ellipse has become a rod whose shape is most aspherical and $\Delta = 1$. But those values of cL/l_p are well beyond the approximation of tight rings where

it was assumed that $cL/l_p, \ll 1$.
The nature of asphericity of the ellipse is computed to be:

$$\Sigma_{\text{ellipse}} = \frac{-1 + 33c\frac{L}{l_p} + 33\left(c\frac{L}{l_p}\right)^2 - \left(c\frac{L}{l_p}\right)^3}{\left[1 + 14c\frac{L}{l_p} + \left(c\frac{L}{l_p}\right)^2\right]^{3/2}} = -1 + \frac{3\pi^2}{10}\frac{L}{l_p} + \mathcal{O}((L/l_p)^2)\,. \tag{5.27}$$

This function is drawn in Fig. 5.8(b). A linear growth of the nature of asphericity for small values of L/l_p is observed starting from an oblate shape of a rigid ring with $\Sigma = -1$. For higher flexibility the ellipse becomes rod-like which corresponds to $\Sigma = 1$. In between, the nature of asphericity crosses zero, if the squared semiaxes have a ratio of 2:1.

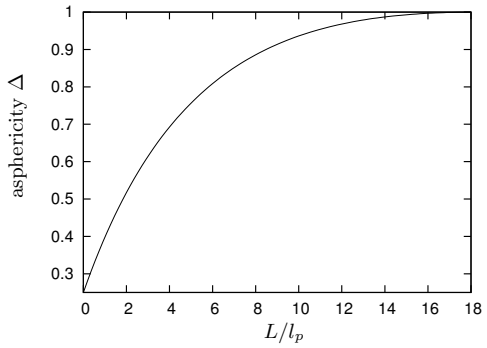

(a) Asphericity of an ellipse versus flexibility from Eq. (5.26).

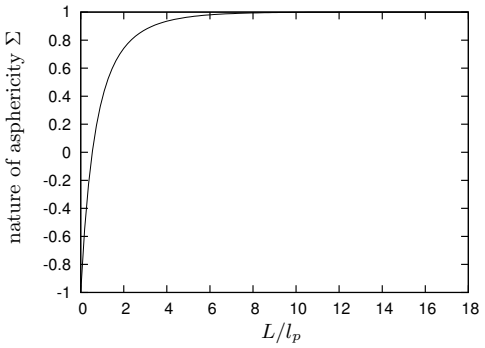

(b) Nature of asphericity of an ellipse versus increasing flexibility from Eq. (5.27).

Figure 5.8: The asphericity and the nature of asphericity of an ellipse. The semimajor axis is assumed to be growing from the radius of a rigid ring with the square root of the ratio of perimeter to persistence length, while the semiminor axis decreases from R_c by the same amount.

Meant to model the mean asphericity and mean nature of asphericity, the scaling argument only considers the main effect, the elliptical shape, that changes the aspect of a tight ring. However, the mean constitutes from several different configurations which are not pictured individually. Therefore, it is illuminating to study a distribution of states. The distribution function P as introduced in section 5.3.1 is used for this purpose. The latter cannot be predicted by the scaling argument, but the analytic calculations forecast a line on which all ellipses with different eccentricities depending on L/l_p can be found, see Fig. 5.9. The rigid ring is represented by the coordinates $(\rho = 1, \theta = \pi/3)$, the point farthest to the right. From there on ρ increases, while θ decreases with a growing eccentricity of the ellipse. At first, both change very fast, then, they alter slower and slower.

Having deduced all relevant shape parameters for an ellipse whose semiaxes are increasing and decreasing with the square root of the ratio of perimeter to persistence length, real semiflexible polymer are investigated.

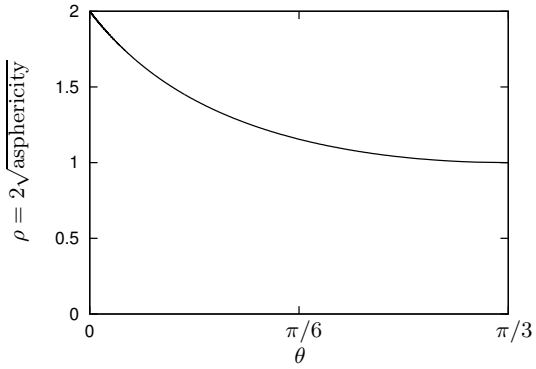

Figure 5.9: Asphericity and nature of asphericity of all elliptical conformations based on Eq. (5.22) with $c\,L/l_p < 1$ in one plot. ρ is proportional to the square root of Δ, while θ is related to the nature of asphericity. The asphericity and the prolateness increase from right to left starting from the rigid ring conformation at $\rho = 1$ and $\theta = \pi/3$.

5.3.3 The change of shape

When increasing the flexibility of a polymer ring by raising the ratio of perimeter to persistence length, the mean shape of the ring is expected to change. The scaling argument forecasts a linear grow of asphericity and nature of asphericity for tight semiflexible rings, starting from $\Delta = 0.25$ and $\Sigma = -1$, respectively. In addition, analytic calculations predict an asphericity of $\Delta \approx 0.2464$ for freely jointed rings [13]. Hence, a cross-over between tight and flexible rings is expected to occur.

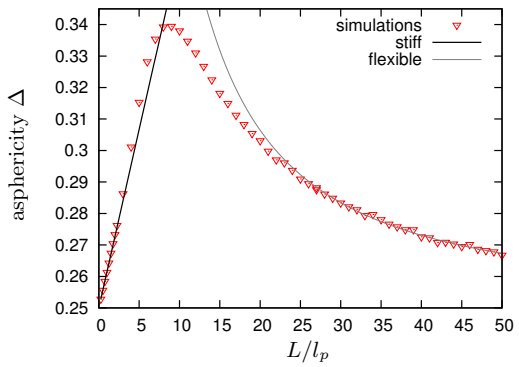

(a) Asphericity of a semiflexible ring versus ratio of perimeter to persistence length.

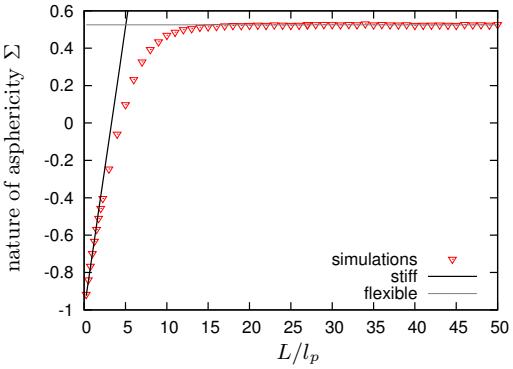

(b) Nature of asphericity of a semiflexible ring versus increasing flexibility L/l_p.

Figure 5.10: Monte Carlo simulation data for the mean asphericity Δ and the mean nature of asphericity Σ versus increasing flexibility. Both increase linearly with growing flexibility for tight rings according to Eqs. (5.28) and (5.29) (black line), respectively. Then, Σ saturates at at a prolate shape of $\Sigma = (0.5252 \pm 4 \cdot 10^{-4})$, while the asphericity decreases in a power law corresponding to Eq. (5.30) (grey line). The error bars are about of the size of the symbols.

Performing Metropolis Monte Carlo simulations as described in section 4.2, the shape pa-

rameters Δ and Σ are calculated according to their definition, see Eqs. (5.15) and (5.16), respectively. Clearly, diagonalizing the matrices did not provoke a problem in the simulations. The results of the Monte Carlo simulations are presented in Fig. 5.10. For tight rings both asphericity and nature of asphericity do grow linearly with the ratio of perimeter to persistence length. Up to $L/l_p = 3$ a straight line obtained from least square fitting gives a good approximation. For the asphericity the best fit is found as:

$$\Delta = 0.25 + (0.01133 \pm 7 \cdot 10^{-5})\frac{L}{l_p} , \tag{5.28}$$

while the nature of asphericity obeys in this regime a straight line given by:

$$\Sigma = -1 + (0.302 \pm 7 \cdot 10^{-3})\frac{L}{l_p} . \tag{5.29}$$

Compared to the predictions of the scaling analysis given in Eqs. (5.26) and (5.27) the values obtained from the simulations are roughly one order of magnitude too large. Hence, the eccentricity of the ellipse grows slower with increasing flexibility as forecasted by the calculations. This is expected since the scaling argument is based on the calculation of the undulations of a weakly bend rod with periodic boundary conditions. These computations do not account for the overall curvature of the ring, which induces additional stiffness, leading to less flexible configurations than predicted by the scaling argument.
Proceeding beyond the tight ring limit, the asphericity progresses still almost linearly before it exhibits a maximum at about $L/l_p = 8$. Afterwards the asphericity decreases constantly towards $\Delta \approx 0.2464$ at L/l_p to infinity, obeying the following power law:

$$\Delta \propto \left(\frac{L}{l_p}\right)^{-(1.29\pm0.02)} . \tag{5.30}$$

The nature of asphericity on the other hand saturates to a constant value of $\Sigma = (0.5252 \pm 4 \cdot 10^{-4})$ at L/l_p of the order of 15.

To get an intuitive understanding of what kind of shape changes occur during the cross-over from semiflexible to flexible rings, a number of snapshots have been taken, see Fig. 5.11. To sample all characteristic features of the cross-over, the pictures were taken at $L/l_p = 1, 4, 8, 16, 32, 64$, such that their individual asphericity and nature of asphericity are close to the mean values of the ensemble, determined beforehand. The colors of the ring segments are chosen as in the pictures in chapter 2 and 3. Due to vanishing twist stiffness all segments can freely rotate about its center line producing a rough structure of the ring.

The linear increase of the asphericity is due to the growing eccentricity of the ellipse. This is supported by the first three snapshots at $L/l_p = 1, 4, 8$, which show an elliptical trajectory though rotated in space. In addition, one observes that the undulations out of the ellipse increase with raising flexibility.
Beyond the maximum, the asphericity decreases, finally integrating into a power law decay. From the snapshots one can deduce that the overall prolate shape remains, while the trajectory of the former ellipse is more and more crumbled up. Since there is no self-avoidance included the segments can intersect each other yielding very compact structures. The more condensed the ring configuration the smaller the variance of the eigenvalues λ_i, $i = 1, 2, 3$, and hence,

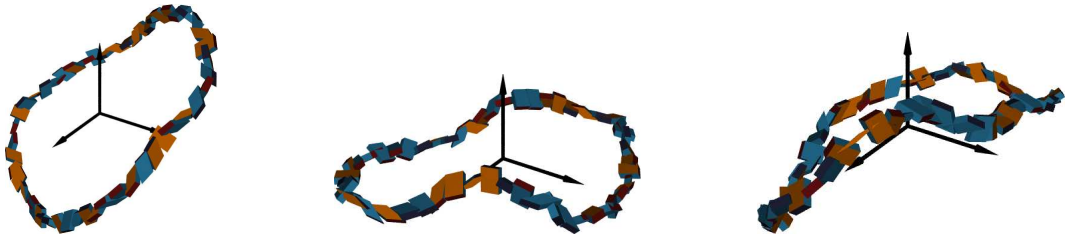

(a) $L/l_p = 1$,
$\Delta = 0.2613$,
$\Sigma = -0.673$.

(b) $L/l_p = 4$,
$\Delta = 0.3024$,
$\Sigma = -0.057$.

(c) $L/l_p = 8$,
$\Delta = 0.3389$,
$\Sigma = 0.395$.

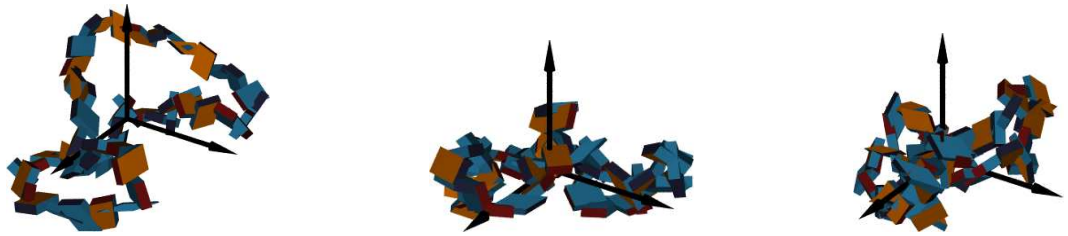

(d) $L/l_p = 16$,
$\Delta = 0.3143$,
$\Sigma = 0.525$.

(e) $L/l_p = 32$,
$\Delta = 0.2758$,
$\Sigma = 0.530$.

(f) $L/l_p = 64$,
$\Delta = 0.2608$,
$\Sigma = 0.533$.

Figure 5.11: Typical conformations of a semiflexible ring at different levels of flexibility. The conformations were chosen such that their individual shape parameters are about equal to the mean values of the asphericity and nature of asphericity of the respective ensemble. For small values of L/l_p the dominating overall shape is an ellipse, with increasing eccentricity. For more flexible rings the ellipse is more and more crumbled up, retaining an overall prolate shape.

the smaller the asphericity.
The nature of asphericity also grows due to the progressing eccentricity of the elliptical center line, transversing from an absolutely oblate shape to an prolate shape. The abscissa is crossed, when the semimajor axis is about twice the size of the semiminor axis. Further raise of the L/l_p does eventually not result in a further augmentation of the nature of asphericity due to energetic as well as entropic reasons. The number of rod-like conformations is smaller than those with moderate prolateness. On the other hand, there is no argument why the polymer ring should become oblate again. Hence, the nature of asphericity saturates at a constant value.
Former Monte Carlo simulations have estimated the nature of asphericity of random walks to be $\Sigma_{RW} = 0.481 \pm 0.009$ [8]. The shape of a closed random walk, i.e. a flexible polymer ring, is with $\Sigma = (0.5252 \pm 4 \cdot 10^{-4})$ slightly more prolate. It seems astonishing that the overall nature of asphericity does not change for $L/l_p > 15$. On the other hand, a prolate shape might be less symmetric than an oblate shape and asymmetry might be favorable due to entropic reasons.

However, understanding the change of the mean asphericity and the mean nature of aspheric-

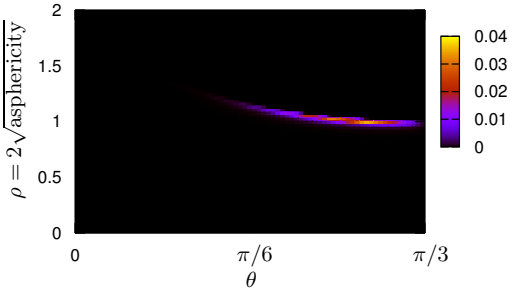

(a) Distribution of shapes for $L/l_p = 1$.

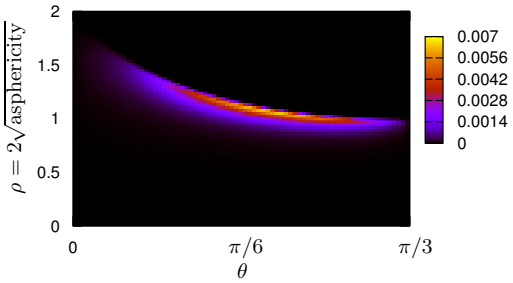

(b) Distribution of shapes for $L/l_p = 4$.

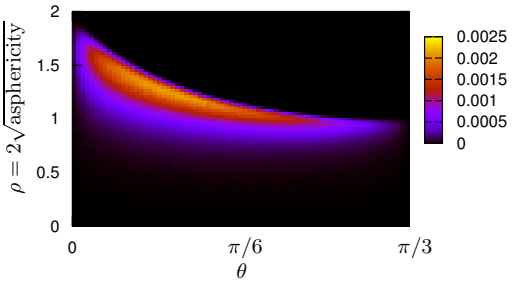

(c) Distribution of shapes for $L/l_p = 8$.

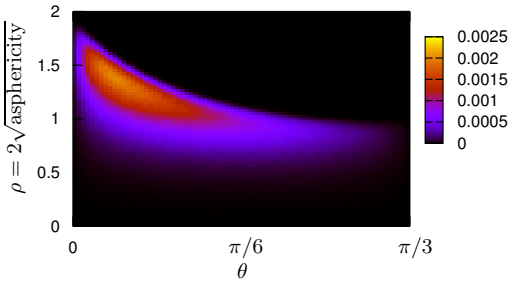

(d) Distribution of shapes for $L/l_p = 16$.

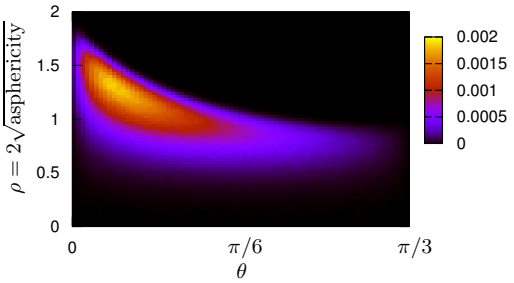

(e) Distribution of shapes for $L/l_p = 32$.

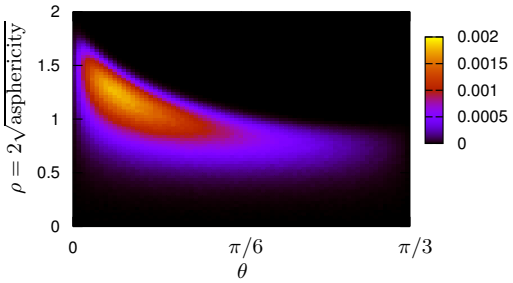

(f) Distribution of shapes for $L/l_p = 64$.

Figure 5.12: The distribution of asphericity and nature of asphericity at different levels of flexibility. $\rho = 2\sqrt{\Delta}$ measures the asphericity, while θ indicates the nature of asphericity, where $0 \leq \theta \leq \pi/6$ corresponds to an prolate and $\pi/6 \leq \theta \leq \pi/3$ to an oblate shape.

ity of an ensemble of polymer rings is only half of the story. To obtain a full picture, one should also investigate the distribution of the shape parameters. For this purpose, the distribution function P as introduced in section 5.3.1 is examined for $L/l_p = 1, 4, 8, 16, 32, 64$, see Fig. 5.12. In this distribution the abscissa θ indicates the nature of asphericity, ranging from $0 \leq \theta \leq \pi/6$ for prolate shapes and from $\pi/6 \leq \theta \leq \pi/3$ for oblate shapes. The ordinate ρ measures the asphericity reaching from zero for spherically symmetric objects to $\rho = 2$ for a rod.
For the stiffest polymer ring pictured in Fig. 5.12, $L/l_p = 1$, the configurations are all quite concentrated, all lying on a curve equivalently to the curve of ellipses calculated in the scaling argument, Fig. 5.9. Hence, all ring conformations have an almost elliptical shape, where the conformations with higher eccentricity are less frequent, than those with smaller eccentricity. Note that the rigid ring conformation corresponding to $(\rho = 1, \theta = \pi/3)$ is almost not existent any more.
When the ratio of perimeter to persistence length is increased to $L/l_p = 4$, the frequent configurations move further up the curve of elliptical shapes. However, there is a new tendency to conformations with both smaller ρ and θ than forecasted by an ellipse. These are observed due to the development of fluctuations perpendicular to the plane of the ellipse, which both increase the prolateness and decrease the asphericity. Since the amplitudes of the out-of-plane fluctuations decay with $1/(n^2 - 1)$, while the in-plane undulations decay slightly faster with $1/n^2$, as calculated in section 3.3, one may infer that the deviations from the elliptical shape at $L/l_p = 4$ are caused predominantly by higher out-of-plane modes, resulting in undulations of the ellipse perpendicular to its plane.
On the other hand, there is no effect which drives the configurations beyond the line of ellipses to a region of both large ρ and θ. Hence, this region is always blocked for the shapes of a semiflexible ring, regardless of how flexible it becomes.
Increasing the flexibility to $L/l_p = 8$ the frequent conformations are even more prolate and less spherical than before due to the higher eccentricity of the ellipse. However, the region of highly excited configurations is slightly below the line of elliptical shapes indicating that the undulations out of the oval shape increased, both perpendicular and within the plane of the ellipse, resulting in more spherical shapes. Furthermore, there is a tendency to more spherical but highly prolate shapes, though barely accounted for at this stage of flexibility. The reason for these conformations may be, that more and more higher modes are excited which provoke the undulation of the ellipse with "cloverleaf" structures. These modes lead to configurations, where the ring folds on itself, and hence seems more spherical. These kind of crumpled shapes become abundant, when the flexibility is further amplified.
For $L/l_p = 16$ pure elliptical trajectories occur rarely. Numerous configurations are rather prolate and aspherical, since now almost all rings exhibit higher modes and so the amount of crumpled structures grows.
The distribution of prolateness seems not to change on increasing the flexibility further, as reflected by the constant mean nature of asphericity, found previously. However, the asphericity of the frequent configurations decreases constantly as the whole distribution wanders to smaller and smaller values of ρ. This can be explained by recalling, that the more flexible the rings are the more crumbled are their shapes, leading to a smaller variance of the eigenvalues and hence, a smaller asphericity. Note that the distributions of flexible rings is broadly spread out, such that still very much rod-like or disc-like configurations occur, though rarely.

The study of the shape of a polymer ring is an elegant tool to understand its fluctuations in

terms of modes. Analyzing the first modes we are able to give a scaling argument for tight rings, which are dominated by an elliptical shape. The change of shape on increasing the flexibility beyond the limit of tight rings illuminates when higher modes are excited and how they change the trajectory of the fluctuating ring.

6 Summary and Outlook

This thesis is concerned with the statistical mechanics of polymer rings and polymer bundle rings in equilibrium. The conformations of the rings result from the interplay of thermal excitations and the internal elastic stress of the polymer. Since polymer bundles may have an anisotropic cross section, they are modeled as ribbons, assigning two bending stiffnesses related to bending about the two principal axes of the cross-sectional plane in addition to a twist stiffness. Pursuing a theoretical description of fluctuating ribbonlike rings a two-fold approach is taken. On the one hand an analytic model is introduced, on the other hand Metropolis Monte Carlo simulations are employed.

The analytic model introduced for tight rings in chapter 3 accounts for an asymmetric cross-sectional plane and takes, in contrast to previous work, the unconfined ground state of the polymer to be an extended rod, as in the case of cytoskeletal filaments. The model is based on a parameterization of the trajectories of ribbons in terms of Euler angles. Approximating the fluctuations of a ring to be small with respect to the conformation of a rigid ring, the elastic free energy of ribbonlike rings is expanded around the ground state ring conformation. The latter is chosen such that it minimizes the elastic free energy.
To reflect the overall properties of polymer rings, the mean square diameter is introduced as the characteristic parameter. A detailed analysis of the mean square diameter depending on the relative bending and twist stiffness is presented.

The Metropolis Monte Carlo simulations are focussed on the study of rings consisting of a single semiflexible filament, see chapter 5. Those polymer rings have a symmetric cross-sectional plane and no twist stiffness, and are comprised in the analytic model as a limiting case. Comparison of the simulation data with the analytic predictions for the mean square diameter yields an excellent agreement up to tremendous orders of flexibility. Hence, the mean square diameter is proposed as the new parameter of choice to determine the persistence length of semiflexible rings in experiments.
Furthermore, the Monte Carlo simulations are employed to study the cross-over between the semiflexible and the flexible regime of a polymer ring. Investigating the radius distribution of semiflexible rings, the cross-over is found to be dominated by a finite-size effect arising from the upper boundary for the radius of the ring.
Finally, the mean shape of semiflexible rings is addressed. Former investigations only considered the aspect of flexible polymers with self-avoidance and without self-avoidance. In this thesis an analysis of the shape of semiflexible polymer rings in the entire range of flexibility is provided. For tight semiflexible rings a scaling argument explains the change of shape. The latter is based on the assumption that the mean configuration of a tight ring is elliptical. For higher degrees of flexibility a power law is identified.

As the simulation of semiflexible rings lead to a more complete picture of their properties, one could in a similar manner investigate ribbons with asymmetric cross section and non-

zero twist stiffness using Metropolis Monte Carlo simulations. For this purpose, new moves have to be implemented, since the crankshaft move, utilized up to now, is quasi-ergodic when the cross-section turns asymmetric. A good candidate for the implementation of rings with anisotropic bending stiffness is the end-bridging Monte Carlo introduced by Mavrantzas et al. [36]. Some preliminary simulations have been run, but the laborious programs still need refinement.

Future work may extend to so-called nicked rings, where the interconnection of the ends of the polymer includes a non-zero angle between the principal axes in the cross-sectional plane. Those nicked rings are the reason for supercoiling of helical rings and could also provoke fascinating behavior for initially straight ribbons. For this project, a good starting point would be a detailed analysis of the minima of the free energy landscape of nicked rings in dependence of the magnitude of the angle enclosed by the respective principal axes at the link. Afterwards, the elastic free energy of fluctuating nicked rings could be expanded around those minima and an analysis of their statistical mechanics analogous to this thesis could be pursued.

A Appendix

A.1 Derivation of the generalized Frenet equations

As supplement to section 2.2 the generalized Frenet equations are derived in this appendix.

The kinematics of a ribbon can be described in terms of Euler angles analogous to the formalism developed for the analysis of elastic rods, see section 2.2.2. To each position along the center line of a ribbon a local body coordinate system is assigned $\mathbf{t}_i$, $i = 1, 2, t$. A rotation of the fixed space coordinates by the Euler angles leads to alignment of the two triads. Hence, all body coordinate can be expressed in terms of the Euler angles, as:

$$\mathbf{t}_1 = \begin{pmatrix} \cos\psi\cos\phi - \cos\theta\sin\phi\sin\psi \\ \cos\psi\sin\phi + \cos\theta\cos\phi\sin\psi \\ \sin\psi\sin\theta \end{pmatrix}, \tag{A.1}$$

$$\mathbf{t}_2 = \begin{pmatrix} -\sin\psi\cos\phi - \cos\theta\sin\phi\cos\psi \\ -\sin\psi\sin\phi + \cos\theta\cos\phi\cos\psi \\ \cos\psi\sin\theta \end{pmatrix}, \tag{A.2}$$

$$\mathbf{t}_t = \begin{pmatrix} \sin\theta\sin\phi \\ -\sin\theta\cos\phi \\ \cos\theta \end{pmatrix}. \tag{A.3}$$

The change of the body axes as they proceed along the center line is equal to rotations of the body coordinates, provoked by the "angular velocity" vector $\boldsymbol{\omega}$, where the infinitesimal rotations $\boldsymbol{\omega}$ are themselves related to the change of the Euler angles.

$$\omega_1 = \frac{d\phi}{ds}\sin\psi\sin\theta + \frac{d\theta}{ds}\cos\psi\,, \tag{A.4}$$

$$\omega_2 = \frac{d\phi}{ds}\cos\psi\sin\theta - \frac{d\theta}{ds}\sin\psi\,, \tag{A.5}$$

$$\omega_3 = \frac{d\phi}{ds}\cos\theta + \frac{d\psi}{ds}\,. \tag{A.6}$$

Using the parameterization of the local body coordinates in terms of Euler angles the generalized Frenet equations can be derived. The latter predict the change of the local body axes along the arc length s of the center line of the ribbon. Hence, deriving the first body

coordinate by s yields:

$$\frac{d\mathbf{t}_1}{ds} = \begin{pmatrix} -\dot{\phi}(\cos\psi\sin\phi + \cos\theta\cos\phi\sin\psi) + \dot{\theta}\sin\theta\sin\phi\sin\psi \\ \dot{\phi}(\cos\psi\cos\phi - \cos\theta\sin\phi\sin\psi) - \dot{\theta}\sin\theta\cos\phi\sin\psi \\ \dot{\theta}\sin\psi\cos\theta \end{pmatrix} \tag{A.7}$$

$$+ \begin{pmatrix} -\dot{\psi}(\sin\psi\cos\phi + \cos\theta\sin\phi\cos\psi) \\ -\dot{\psi}(\sin\psi\sin\phi - \cos\theta\cos\phi\cos\psi) \\ \dot{\psi}\cos\psi\sin\theta \end{pmatrix}, \tag{A.8}$$

where $\dot{\eta}$, $\eta = \phi, \theta, \psi$ denotes the derivative by s of the respective Euler angle. Inserting a one of the form $1 = \sin^2\theta + \cos^2\theta$ in the terms $(\dot{\phi}\cos\psi\sin\phi)$ and $(\dot{\phi}\cos\psi\cos\phi)$, the vector above can be simplified to:

$$\frac{d\mathbf{t}_1}{ds} = -\left[\dot{\phi}\cos\psi\cos\theta - \dot{\theta}\sin\psi\right] \begin{pmatrix} \sin\theta\sin\phi \\ -\sin\theta\cos\phi \\ \cos\theta \end{pmatrix} \tag{A.9}$$

$$+ \left[\dot{\phi}\cos\theta + \dot{\psi}\right] \begin{pmatrix} -\sin\psi\cos\phi - \cos\theta\sin\phi\cos\psi \\ -\sin\psi\sin\phi + \cos\theta\cos\phi\cos\psi \\ \cos\psi\sin\theta \end{pmatrix}. \tag{A.10}$$

The vectors are identified as $\mathbf{t}_t$ and $\mathbf{t}_2$, respectively, while the corresponding prefactors denote the second and third component of the infinitesimal rotation vector $\boldsymbol{\omega}$, ω_2 and ω_3. Hence, the first generalized Frenet equation is derived:

$$\frac{d\mathbf{t}_1}{ds} = -\omega_2\mathbf{t}_t + \omega_3\mathbf{t}_2\ . \tag{A.11}$$

In an analog manner the other derivatives of the local body vectors can be simplified. For the derivative of $\mathbf{t}_2$ one obtains:

$$\frac{d\mathbf{t}_2}{ds} = \begin{pmatrix} \dot{\phi}(\sin\psi\sin\phi - \cos\theta\cos\phi\cos\psi) + \dot{\theta}\sin\theta\sin\phi\cos\psi \\ -\dot{\phi}(\sin\psi\cos\phi + \cos\theta\sin\phi\cos\psi) - \dot{\theta}\sin\theta\cos\phi\cos\psi \\ \dot{\theta}\cos\psi\cos\theta \end{pmatrix} \tag{A.12}$$

$$+ \begin{pmatrix} -\dot{\psi}(\cos\psi\cos\phi - \cos\theta\sin\phi\sin\psi) \\ -\dot{\psi}(\cos\psi\sin\phi + \cos\theta\cos\phi\sin\psi) \\ -\dot{\psi}\sin\psi\sin\theta \end{pmatrix}. \tag{A.13}$$

Again a one of the form $1 = \sin^2\theta + \cos^2\theta$ is included, now in the terms $(\dot{\phi}\sin\psi\sin\phi)$ and $(\dot{\phi}\sin\psi\cos\phi)$, yielding:

$$\frac{d\mathbf{t}_2}{ds} = \left[\dot{\phi}\sin\psi\sin\theta + \dot{\theta}\cos\psi\right] \begin{pmatrix} \sin\theta\sin\phi \\ -\sin\theta\cos\phi \\ \cos\theta \end{pmatrix} \tag{A.14}$$

$$- \left[\dot{\phi}\cos\theta + \dot{\psi}\right] \begin{pmatrix} \cos\psi\cos\phi - \cos\theta\sin\phi\sin\psi \\ \cos\psi\sin\phi + \cos\theta\cos\phi\sin\psi \\ \sin\psi\sin\theta \end{pmatrix}. \tag{A.15}$$

This is equivalent to the second Frenet equation, on identifying the vectors with $\mathbf{t}_t$ and $\mathbf{t}_1$ and the prefactors with ω_1 and ω_3, respectively.

$$\frac{d\mathbf{t}_2}{ds} = \omega_1\mathbf{t}_t - \omega_3\mathbf{t}_1\ . \tag{A.16}$$

The derivative of the tangent of the ribbon is rather short:

$$\frac{d\mathbf{t}_t}{ds} = \begin{pmatrix} \dot{\phi}\sin\theta\cos\phi + \dot{\theta}\cos\theta\sin\phi \\ \dot{\phi}\sin\theta\sin\phi - \dot{\theta}\cos\theta\cos\phi \\ -\dot{\theta}\sin\theta \end{pmatrix}. \tag{A.17}$$

To bring this derivative to the form of the Frenet equations a factor of $1 = \sin^2\psi + \cos^2\psi$ has to be multiplied with every single term. In addition, various terms are added and subtracted simultaneously to obtain:

$$\frac{d\mathbf{t}_t}{ds} = -\Big[\dot{\phi}\sin\psi\sin\theta + \dot{\theta}\cos\psi\Big] \begin{pmatrix} -\sin\psi\cos\phi - \cos\theta\sin\phi\cos\psi \\ -\sin\psi\sin\phi + \cos\theta\cos\phi\cos\psi \\ \cos\psi\sin\theta \end{pmatrix} \tag{A.18}$$

$$+ \Big[\dot{\phi}\cos\psi\sin\theta - \dot{\theta}\sin\psi\Big] \begin{pmatrix} \cos\psi\cos\phi - \cos\theta\sin\phi\sin\psi \\ \cos\psi\sin\phi + \cos\theta\cos\phi\sin\psi \\ \sin\psi\sin\theta \end{pmatrix}. \tag{A.19}$$

This equation is equivalent to the third and last generalized Frenet equation:

$$\frac{d\mathbf{t}_t}{ds} = -\omega_1\mathbf{t}_2 + \omega_2\mathbf{t}_1\ . \tag{A.20}$$

Hence, the generalized Frenet equations can be derived from the parameterization of the local body coordinates in terms of Euler angles on identifying Euler's equations for the "angular velocity" $\boldsymbol{\omega}$.

A.2 Checking the wormlike chain limit

When introducing a new model, it is always recommendable to approve it by recovering well-known results. In the case of the fluctuating ribbonlike ring, one expects the influence of the geometry to fade when the contour radius R_c of the ring is increased. The local behavior should then resemble the behavior of a wormlike chain. Hence, the tangent-tangent correlation of a wormlike chain should be recovered when taking R_c large with respect to the distance of the tangents s. Furthermore, the model is approved by showing that the in- and out-of-plane fluctuations locally equalize for a large fluctuating ring.

To compute the tangent-tangent correlation, the formula derived in section 3.4.1 is used. This formula relates the tangent-tangent correlation to the correlations of the Euler angles, which in turn are evaluated from the limiting case of the free elastic energy for large contour radius R_c.
Assuming R_c to be large compared with s, we omit terms of order $1/R_c$ in the elastic free energy in Eq. (3.5). Thus, the elastic free energy becomes diagonal in the Euler angles:

$$F = \frac{k_BT}{2}\int_0^{2\pi R_c} ds\Big\{a_1\left(\frac{d\delta\phi}{ds}\right)^2 + a_2\left(\frac{d\delta\theta}{ds}\right)^2 + a_3\left(\frac{d\delta\psi}{ds}\right)^2\Big\}\ . \tag{A.21}$$

Proceeding analogous to section 3.1.3, the Fourier transformed elastic free energy is found to be:

$$\begin{aligned} F &= \frac{k_B T \pi}{R_c}\Big\{ a_2 |\delta\tilde{\psi}(1)|^2 + a_3 |\delta\tilde{\psi}(1)|^2 \\ &+ \sum_{n=2}^{\infty}\left[a_1 n^2 |\delta\tilde{\phi}(n)|^2 + a_2 n^2 |\delta\tilde{\theta}(n)|^2 + a_3 n^2 |\delta\tilde{\psi}(n)|^2 \right]\Big\}. \end{aligned} \tag{A.22}$$

Note that the Euler angles are now decoupled, yielding modes which decay with $1/n^2$ for every single Euler angle.
The correlations of the Euler angles for R_c large compared to s are calculated to:

$$\langle \delta\theta(s_2)\delta\theta(s_1)\rangle_{s/R_c\ll 1} = \frac{R_c}{a_2\pi}\left(\frac{(\pi - s/R_c)^2}{4} - \frac{\pi^2}{12}\right), \tag{A.23}$$

$$\langle \delta\phi(s_2)\delta\phi(s_1)\rangle_{s/R_c\ll 1} = \frac{R_c}{a_1\pi}\left(\frac{(\pi - s/R_c)^2}{4} - \frac{\pi^2}{12} - \cos(s/R_c)\right), \tag{A.24}$$

$$\langle \delta\psi(s_2)\delta\psi(s_1)\rangle_{s/R_c\ll 1} = \frac{R_c}{a_3\pi}\left(\frac{(\pi - s/R_c)^2}{4} - \frac{\pi^2}{12}\right), \tag{A.25}$$

where s denotes $s = |s_1 - s_2|$ and the following formula was used to calculate the sums:

$$\sum_{n=2}^{\infty}\frac{\cos(n\, s/R_c)}{n^2} = \frac{\left(\pi - \frac{s}{R_c}\right)^2}{4} - \frac{\pi^2}{12} - \cos\left(s\frac{s}{R_c}\right). \tag{A.26}$$

Inserting the correlations of the Euler angles Eqs. (A.23), (A.24) into the expression for the tangent-tangent correlation Eq. (3.39) yields:

$$\begin{aligned} \langle \mathbf{t}_t(s_1)\mathbf{t}_t(s_2)\rangle_{s/R_c\ll 1} &= \cos(s/R_c) + \frac{R_c}{a_2\pi}\left(-\frac{s\pi}{2R_c} + \frac{s^2}{4R_c^2} + \frac{\pi^2}{6}(1-\cos(s/R_c))\right) \\ &+ \frac{R_c}{a_1\pi}\left(-\frac{s\pi}{2R_c} + \frac{s^2}{4R_c^2} + 1 - \cos(s/R_c)\right)\cos(s/R_c), \end{aligned} \tag{A.27}$$

where s denotes the distance of the tangents along the center line of the ring $s = |s_2 - s_1|$. To pursue the wormlike chain limit, this tangent-tangent correlation is expanded for R_c large compared with the distance of the tangents along the trajectory, i.e. $s/R_c \to 0$, resulting in:

$$\begin{aligned} \langle \mathbf{t}_t(s_1)\mathbf{t}_t(s_2)\rangle_{s/R_c\ll 1} &= 1 - \frac{1}{2}\left(\frac{1}{a_1} + \frac{1}{a_2}\right)s \\ &+ \frac{1}{a_2 R_c \pi}\frac{3+\pi^2}{12}s^2 + \frac{1}{a_1 R_c \pi}\frac{3}{4}s^2 + O\left(\frac{s}{R_c}\right)^2. \end{aligned} \tag{A.28}$$

Up to first order, the expansion of an exponential function with argument $-\frac{1}{2}\left(\frac{1}{a_1} + \frac{1}{a_2}\right)s$ is obtained, higher order terms turn out to be antisymmetric in a_1 and a_2, which is imposed by the geometry of the problem. Comparison with the series of the tangent-tangent correlation of the wormlike chain in the limit of tight chains:

$$\langle \mathbf{t}(s_1)\mathbf{t}(s_2)\rangle = e^{-\frac{|s_1 - s_2|}{l_p}} = 1 - \frac{1}{l_p}|s_1 - s_2| + \ldots, \tag{A.29}$$

yields an agreement for the first two terms for equal bending stiffness in-plane and out-of-plane $a_1 = a_2 = l_p$. Therefore, the model for tight ribbonlike ring includes the limiting case of local wormlike chain behavior for large radii R_c.

Furthermore, the local fluctuations of large rings are assumed to be symmetric in- and out-of-plane, since the overall geometry of the ring does not influence the local fluctuations anymore. To approve this statement, the mean square displacement is calculated and expanded for $s/R_c \ll 1$.

The mean square displacement can be calculated by directly integrating the tangent-tangent correlation according to expression (3.40), yielding:

$$\begin{aligned}\langle(\mathbf{r}(s)-\mathbf{r}(0))^2\rangle_{s/R_c\ll 1} &= 2R_c^2(1-\cos(s/R_c)) - \frac{R_c^3}{24a_1\pi}\big[24(1-\cos(s/R_c)) \\ &+12s/R_c(s/R_c-2\pi)(1+\cos(s/R_c)) + 6(1-\cos(2s/R_c)) + 48(\pi - s/R_c)\sin(s/R_c)\big] \\ &-\frac{R_c^3}{24a_2\pi}\big[8\pi^2(1-\cos(s/R_c)) - (s/R_c)^2(s/R_c-2\pi)^2\big]\,. \end{aligned} \tag{A.30}$$

Expanding this equation for the mean square displacement around $s/R_c = 0$ up to third order in s/R_c, yields equal contributions from in- and and out-of-plane fluctuations indicated by the equal proportion of $1/a_1$ and $1/a_2$ terms:

$$\langle(\mathbf{r}(s)-\mathbf{r}(0))^2\rangle_{s/R_c\ll 1} = s^2 - \frac{1}{6}\left(\frac{R_c}{a_1}+\frac{R_c}{a_2}\right)s^3 + \cdots\,. \tag{A.31}$$

Notice that the fluctuations are independent of R_c, as one would expect for local fluctuations on an infinitely long wormlike chain. Hence, the fluctuating ring model obeys locally the behavior of a wormlike chain for large contour radii.

Glossary

l_p	persistence length
a_1, a_2	persistence lengths corresponding to the bending stiffnesses about the two principal axes of the cross-sectional plane
a_t	persistence length corresponding to the twist stiffness
$\alpha = a_1/a_2$	relative bending stiffness
$\tau = a_1/a_t$	relative twist stiffness
L	polymer length
R_c	contour radius of a polymer ring $2\pi R_c = L$
s	arc length
$\mathbf{r}(s)$	trajectory
$\mathbf{r}_\perp(s)$	undulations
$r_\parallel(s)$	stored length
$\mathbf{X}$, $\mathbf{Y}$, $\mathbf{Z}$	fixed space axes
$\mathbf{t}_1$, $\mathbf{t}_2$	local body axes aligned to the two principal axes of the cross-sectional plane
$\mathbf{t}, \mathbf{t}_t$	tangent
$\mathbf{n}$	normal vector of a space curve
$\mathbf{b}$	binormal vector of a space curve
N	number of segments
k_BT	thermal energy
F	elastic free energy
ω_1, ω_2	curvatures in the two principal directions
ω_3	helical deformation density
$\phi(s)$, $\theta(s)$, $\psi(s)$	Euler angles
$\delta\phi(s)$, $\delta\theta(s)$, $\delta\psi(s)$	relative Euler angles
R	radius
D	diameter
R_g	radius of gyration
$G(R)$	radius distribution
g_1	skewness
Q	shape tensor
$\widehat{Q}$	shifted shape tensor
λ_1, λ_2, λ_3	eigenvalues of the shape tensor
Δ	asphericity
Σ	nature of asphericity
$P(\rho, \theta)$	shape distribution function
$\rho = 2\sqrt{\Delta}$	parameter corresponding to the asphericity
θ	parameter corresponding to the nature of asphericity

Bibliography

[1] S. R. Aragon und R. Pecora.
Dynamics of wormlike chains.
Macromolecules **18**, 1868 (1985).

[2] J. A. Aronovitz und D. R. Nelson.
Universal features of polymer shapes.
J. Physique **47**, 1445 (1986).

[3] C. J. Benham und S. P. Mielke.
DNA mechanics.
Annu. Rev. Biomed. Eng. **7**, 21 (2005).

[4] M. Bishop und J. H. R. Clarke.
Brownian dynamics study of the shape of star and linear polymers in different regimes.
J. Chem. Phys. **90**, 6647 (1989).

[5] R. L. Bishop.
There is more than one way to frame a curve.
Am. Math. Monthly **82**, 246 (1975).

[6] D. Bray.
Cell Movements.
Garland, New York (2001).

[7] C. J. Camacho und M. E. Fisher.
Semiflexible planar polymeric loops.
J. Chem. Phys. **94**, 5693 (1991).

[8] J. W. Cannon, J. A. Aronovitz und P. Goldbart.
Equilibrium distribution of shapes for linear and star macromolecules.
J. Phys. I **1**, 629 (1991).

[9] M. M. A. E. Claessens, M. Bathe, E. Frey und A. R. Bausch.
Actin-binding proteins sensitively mediate F-actin bundle stiffness.
Submitted.

[10] M. M. A. E. Claessens, R. Tharmann, K. Kroy und A. R. Bausch.
Microstructure and viscoelasticity of confined semiflexible polymer networks.
Nature Physics **2**, 186 (2006).

[11] G. M. Cooper und R. E. Hausmann.
The Cell: A Molecular Approach.
Sinauer Associates (2003).

[12] H. E. Daniels.
The statistical theory of stiff chains.
Proceedings of the Royal Society in Edinburgh **63A**, 290 (1952).

[13] H. W. Diehl und E. Eisenriegler.
Universal shape ratios for open and closed random walks: exact results for all d.
J.Phys. A: Math. Gen. **22**, L87 (1989).

[14] M. Doi.
Introduction to Polymer Physics.
Clarendon Press, Oxford (2001).

[15] M. Elbaum, D. Kuchnir Fygenson und A. Libchaber.
Buckling microtubules in vesicles.
Phys. Rev. Lett. **76**, 4078 (1996).

[16] M. E. Fisher.
Magnetism in one-dimensional systems –the Heisenberg model for infinite spin.
Am. J. of Phys. **32**, 343 (1963).

[17] R. A. Freitas.
Nanomedicine, Volume I: Basic Capabilities.
Landes Bioscience, Georgetown (1999).

[18] D. Frenkel und B. Smit.
Understanding Molecular Simulation.
Academic Press, San Diego (2002).

[19] M. Fujii und H. Yamakawa.
Moments and transport coefficients of wormlike rings.
Macromolecules **8**, 792 (1975).

[20] F. Gittes, B. Mickey, J. Nettleton und J. Howard.
Flexural rigidity of microtubules and actin filaments measured from thermal fluctuations in shape.
J. Cell Biol. **120**, 923 (1993).

[21] W. Gobush, H. Yamakawa, W. H. Stockmayer und W. S. Magee.
Statistical mechanics of wormlike chains. I. Asymptotic behavior.
J. Chem. Phys. **57**, 2839 (1972).

[22] L. Le Goff, O. Hallatschek, E. Frey und F. Amblard.
Tracer studies on F-Actin fluctuations.
Phys. Rev. Lett. **89**, 258101 (2002).

[23] H. Goldstein, C. Poole und J. Safko.
Classical Mechanics.
Addison Wesley, San Francisco, 3rd Auflage (2002).

[24] K. A. Hoffman, R. S. Manning und J. H. Maddocks.
Link, twist, energy and the stability of DNA minicircles.
Biopolymers **70**, 145 (2003).

[25] J. D. Honeycutt und D. Thirumalai.
Static properties of polymer chains in porous media.
J. Chem. Phys. **90**, 4542 (1989).

[26] K. V. Klenin, A. V. Vologodskii, V. V. Anshelevich, A. M. Dykhne und M. D. Frank-Kamenetskii.
Computer simulation of DNA supercoiling.
J. Mol. Biol. **217**, 413 (1991).

[27] M. Kotelyanskii und D. N. Theodorou.
Simulation Methods for Polymers.
Marcel Dekker (2004).

[28] D. E. Kranbuehl und P. H. Verdier.
Relaxation of the aspherical shapes of random-coil polymer chains.
J. Chem. Phys. **67**, 361 (1977).

[29] O. Kratky und G. Porod.
Röntgenuntersuchung gelöster Fadenmoleküle.
Rec. Trav. Chim. **68**, 1106 (1949).

[30] D. P. Landau und K. Binder.
A Guide to Monte Carlo Simulations in Statistical Physics.
Cambridge University Press, Cambridge (2000).

[31] L. D. Landau und E. M. Lifschitz.
Theory of Elasticity.
Pergamon Press, Oxford (1970).

[32] L. D. Landau und E. M. Lifschitz.
Statistical Physics.
Butterworth-Heinemann, Oxford (1999).

[33] L. Limozin und E. Sackmann.
Polymorphism of cross-linked actin networks in giant vesicles.
Phys. Rev. Lett. **89**, 168103 (2002).

[34] I. Linhartová, B. Novotná, V. Sulimenko, E. Dráberova und P. Dráber.
Gamma-tubulin in chicken erythrocytes: Changes in localization during cell differentiation and characterization of cytoplasmatic complexes.
Developmental Dynamics **223**, 229 (2002).

[35] J. F. Marko und E. D. Siggia.
Statistical mechanics of supercoiled DNA.
Phys. Rev. E **52**, 2912 (1995).

[36] V. G. Mavrantzas, T. D. Boone, E. Zervopoulou und D. N. Theodorou.
End-bridging Monte Carlo: A fast algorithm for atomistic simulation of condensed phases of long polymer chains.
Macromolecules **32**, 5072 (1999).

[37] J. Mazur, C. M. Guttman und F. L. McCrackin.
Monte carlo studies of self-interacting polymer chains with excluded volume. II. Shape of a chain.
Macromolecules **6**, 872 (1973).

[38] N. Metropolis, A. W. Rosenbluth, M. N. Rosenbluth, A. H. Teller und E. Teller.
Equation of state calculations by fast computing machines.
J. Chem. Phys. **21**, 1087 (1953).

[39] B. Mickey und J. Howard.
Rigidity of microtubules is increased by stabilizing agents.
J. Cell Biol. **130**, 909 (1995).

[40] T. Odijk.
DNA in liquid-crystalline environment: Tight bends, rings, supercoils.
J. Chem. Phys. **105**, 1270 (1996).

[41] F. Pampaloni, G. Lattanzi, A. Jonáš, T. Surrey, E. Frey und E.-L. Florin.
Elastic properties of grafted microtubules.
Proc. Natl. Acad. Sci. USA in press.

[42] S. Panyukov und Y. Rabin.
Fluctuating filaments: Statistical mechanics of helices.
Phys. Rev. E **62**, 7135 (2000).

[43] S. Panyukov und Y. Rabin.
Fluctuating elastic rings: Statics and dynamics.
Phys. Rev. E **64**, 011909 (2001).

[44] R Rubin und J. Mazur.
Ordered spans of unrestricted and self-avoiding random-walk models of polymer chains. I. Space-fixed axes.
J. Chem. Phys. **63**, 5362 (1975).

[45] R. Rubin und J. Mazur.
Spans of polymer chains measured with respect to chain-fixed axes.
Macromolecules **10**, 139 (1977).

[46] J. Rudnick und G. Gaspari.
The asphericity of random walks.
J. Phys. A:Math. Gen. **19**, L191 (1986).

[47] N. Saitô, K. Takahashi und Y. Yunoki.
The statistical mechanical theory of stiff chains.
J. Phys. Soc. Jap. **22**, 219 (1967).

[48] J. Shimada und H. Yamakawa.
Moments for DNA topoisomers: The helical wormlike chain.
Biopolymers **27**, 657 (1988).

[49] K. Šolc.
Shape of a random-flight chain.
J. Chem. Phys. **55**, 335 (1971).

[50] K. Šolc und W. H. Stockmayer.
Shapes of a random-flight chains.
J. Chem. Phys. **54**, 2756 (1971).

[51] J. X. Tang, J. A. Käs, J. V. Shah und P. A. Janmey.
Counterion-induced actin ring formation.
Eur. Biophys. J. **30**, 477 (2001).

[52] I. Tobias.
A theory of thermal fluctuations in DNA miniplasmids.
Biophysical Journal **74**, 2545 (1998).

[53] F. Wagner, G. Lattanzi und E. Frey.
Polymers in axially symmetric confining geometries.
Submitted.

[54] J. Wilhelm und E. Frey.
Radial distribution function of semiflexible polymers.
Phys. Rev. Lett. **77**, 2581 (1996).

[55] B. Winckler und F. Solomon.
A role for microtubule bundles in the morphogenesis of chicken erythrocytes.
Proc. Natl. Acad. Sci. USA **88**, 6033 (1991).

[56] H. Yamakawa.
Modern Theory of Polymer Solutions.
Harper & Row, New York (1971).

[57] H. Yamakawa.
Helical Wormlike Chains in Polymer Solutions.
Springer-Verlag, Berlin (1997).

Acknowledgements

First of all, I would like to thank Prof. Dr. Erwin Frey for the interesting topic of my diploma thesis and for his guidance during this year. His enthusiasm and energy were always a source of motivation for myself. I very much appreciated his deep insights into physics which lead to fruitful and stimulating ideas.
I am thankful to Prof. Dr. Thomas Franosch and Claus Heusinger, who always answered all my questions concerning polymer physics.
Furthermore, I would like to thank Dr. Mark Bathe, who offered me all his knowledge about Monte Carlo simulations and the experimental background.
Special thanks goes to my office mates, Wolfram Möbius, Nico Geisel and Thomas Schötz, for all those small questions within this year, all chats during long working days, for just having a very nice time together.
I am grateful to Tobias Reichenbach, who had the patience to proofread this thesis and gave a lot of ideas for enhancement.
Last but not least, I am indebted to Murad Alim, for his love and his encouragement, and my family, who always supported me throughout my life.

Ich versichere, die Arbeit selbstständig angefertigt und dazu nur die im Literaturverzeichnis angegebenen Quellen benutzt zu haben.

München, den 26. Mai 2006